



**HAL**  
open science

# Modeling interfacial effects on transport properties: mechanical properties of polymers, thermal properties of nanofluids

Mihail Vladkov

► **To cite this version:**

Mihail Vladkov. Modeling interfacial effects on transport properties: mechanical properties of polymers, thermal properties of nanofluids. Data Analysis, Statistics and Probability [physics.data-an]. Université Claude Bernard - Lyon I, 2007. English. NNT: . tel-00176186

**HAL Id: tel-00176186**

**<https://theses.hal.science/tel-00176186>**

Submitted on 2 Oct 2007

**HAL** is a multi-disciplinary open access archive for the deposit and dissemination of scientific research documents, whether they are published or not. The documents may come from teaching and research institutions in France or abroad, or from public or private research centers.

L'archive ouverte pluridisciplinaire **HAL**, est destinée au dépôt et à la diffusion de documents scientifiques de niveau recherche, publiés ou non, émanant des établissements d'enseignement et de recherche français ou étrangers, des laboratoires publics ou privés.

N d'ordre 91 - 2007

Année 2007

**THESE**

présentée

devant l'**UNIVERSITE CLAUDE BERNARD - LYON 1**

pour l'obtention

du **DIPLOME DE DOCTORAT**

(arrêté du 7 août 2006)

présentée et soutenue publiquement le 2 Juillet 2007

par

**Mihail VLADKOV**

---

**Modélisation des effets  
d'interface sur les coefficients de  
transport: propriétés  
mécaniques des polymères,  
propriétés thermiques des  
nanofluides**

---

Directeur de thèse: Pr. Jean-Louis BARRAT

JURY: M. Didier LONG (rapporteur, DR CNRS)  
M. Ralf EVERAERS (rapporteur, Pr, ENSL)  
M. Jorg BASCHNAGEL (Pr, ULP Strasbourg)  
M. Jean-Louis BARRAT (directeur de these, Pr, UCBL)  
M. Marc COUTY (Ingénieur de recherche, Michelin)



THESIS

UNIVERSITY CLAUDE BERNARD - LYON 1

presented and defended the 2 of July 2007  
by

Mihail VLADKOV

---

Modeling interfacial effects on  
transport properties:  
mechanical properties of  
polymers, thermal properties of  
nanofluids

---

Supervisor: Pr. Jean-Louis BARRAT

JURY: M. Didier LONG (DR CNRS)  
M. Ralf EVERAERS (Pr ENSL)  
M. Jorg BASCHNAGEL (Pr ULP Strasbourg)  
M. Jean-Louis BARRAT (Pr UCBL)  
M. Marc COUTY (researcher Michelin)



# Acknowledgments

This work has been done in the “Théorie et Modélisation” group of the Laboratoire de Physique de la Matière Condensée et Nanostructures (LPMCN), University Lyon 1, to a large extent in collaboration with the Michelin Research Center in Clermont Ferrand. I would like to express here my gratitude to the people I had the pleasure to work with during my stay at the LPMCN from April 2004 to September 2007.

- First of all, I thank my supervisor, Pr. Jean-Louis Barrat, for his endless support, guidance and advice throughout the three years of my thesis.
- I also thank Kurt Smith, his presence in the laboratory at the beginning of this study was very fruitful and helped me learn a lot.
- The continuous collaboration with Marc Couty and Laurent Petitjean from Michelin, as well as their support is greatly appreciated.
- I thank Yioryos Papakonstantopoulos from the University of Wisconsin in Madison, who provided much of the data for the polymer nanocomposites. His stay at the laboratory was both very productive and pleasant.
- I would also like to acknowledge the discussions with Pr. Ralf Everaers, his expertise on polymer physics and primitive paths was very helpful.
- I would like to thank the members of the jury for their interest in my work and for their in-depth reading of the manuscript.
- Last but not least, I thank the LPMCN staff and my colleagues from the theory group for their warm welcome and assistance.



# Contents

<b>1</b>	<b>Introduction</b>	<b>1</b>
1.1	Context	1
1.1.1	Polymer Nanocomposites and Thin Films	2
1.1.2	Nanofluids	5
1.2	Methods	7
1.3	Overview	9
<b>2</b>	<b>Theoretical background</b>	<b>11</b>
2.1	Coarse grained models	11
2.2	Static properties of a polymer	13
2.3	The Rouse model	14
2.4	The reptation concept	18
2.5	Polymer based composites - reinforcement and Payne effect	22
<b>3</b>	<b>Viscoelasticity of Pure Polymer Melts</b>	<b>27</b>
3.1	Introduction	27
3.2	System description and methods	28
3.3	Viscosity determination by NEMD	32
3.3.1	Green-Kubo approach	35
3.3.2	Rouse modes	38
3.4	Elastic Moduli	43
3.4.1	Method	43
3.4.2	Results	45
3.5	Discussion and Conclusions	52
<b>4</b>	<b>Static properties and adsorption desorption at interfaces</b>	<b>55</b>
4.1	Introduction	55
4.2	Systems description and preparation	56
4.3	Static properties of chains at the interface	61
4.4	Adsorption and desorption dynamics	69
4.5	Conclusion	84

---

<b>5</b>	<b>Dynamics and entanglements at the interface</b>	<b>87</b>
5.1	Introduction . . . . .	87
5.2	Local dynamics near a bare and grafting wall . . . . .	88
5.2.1	Desorption and Mean Square Displacement . . . . .	88
5.2.2	Local Dynamics from Rouse Modes . . . . .	89
5.2.3	Local stress relaxation function . . . . .	94
5.3	Primitive Path Analysis of the Wall Melt Interface . . . . .	96
5.4	Entanglements in polymer nanocomposites . . . . .	101
5.4.1	Effect of fillers on chain conformations . . . . .	104
5.4.2	Influence of fillers on primitive paths . . . . .	105
5.4.3	Predicting the entanglement length . . . . .	109
5.4.4	Conclusion . . . . .	111
5.5	Dynamics in nanocomposites . . . . .	114
5.6	Discussion and conclusions . . . . .	117
<b>6</b>	<b>Heat transfer and conductivity in nanofluids</b>	<b>119</b>
6.1	Introduction . . . . .	119
6.2	Simulation method . . . . .	120
6.3	Modeling pump-probe experiments and determination of the interfacial resistance . . . . .	124
6.4	Conductivity of nanofluids . . . . .	129
6.4.1	The Maxwell Garnett calculation . . . . .	129
6.4.2	Single particle in a heat flow . . . . .	132
6.4.3	Study of Collective Effects . . . . .	134
6.5	Conclusion . . . . .	138
<b>7</b>	<b>Conclusion and Perspectives</b>	<b>141</b>
7.1	Summary of the main results . . . . .	141
7.2	Perspectives . . . . .	143

# Chapter 1

## Introduction

### Contents

---

<b>1.1</b>	<b>Context</b>	<b>1</b>
1.1.1	Polymer Nanocomposites and Thin Films	2
1.1.2	Nanofluids	5
<b>1.2</b>	<b>Methods</b>	<b>7</b>
<b>1.3</b>	<b>Overview</b>	<b>9</b>

---

### 1.1 Context

This work is situated in the global context of computational composite materials research.

Nanocomposites are materials that are created by introducing nanoparticles into a macroscopic sample material. This is part of the growing field of nano technology. Particulate composites reinforced with micron-sized particles of various materials are perhaps the most widely used composites in everyday materials. By scaling the particle size down to the nanometer scale, it has been shown that novel material properties can be obtained.

In general, the nano substances used are nanoscopic filler particles of different nature (metallic, silica, carbon black) or nanotubes and they are dispersed into the other composite materials during processing. The nanomaterials tend to drastically add to the electrical and thermal conductivity as well as to the mechanical strength properties of the original material.

In this section we will give a brief overview of the basic properties of interest of nanocomposite polymer based materials and nanoparticle suspensions (nanofluids).

### 1.1.1 Polymer Nanocomposites and Thin Films

Polymer composites are important commercial materials with applications that include filled elastomers for damping, electrical insulators, thermal conductors, and high-performance composites for use in aircraft. Materials with synergistic properties are chosen to create composites with tailored properties; for example, high-modulus but brittle carbon fibers are added to low-modulus polymers to create a stiff, lightweight composite with some degree of toughness. In recent years, however, we have reached the limits of optimizing composite properties of traditional micrometer-scale composite fillers, because the properties achieved usually involve compromises. Stiffness is traded for toughness, or toughness is obtained at the cost of optical clarity. In addition, macroscopic defects due to regions of high or low volume fraction of filler often lead to breakdown or failure. In the last decade a large window of opportunity has opened to overcome the limitations of traditional micrometer-scale polymer composites - nanoscale filled polymer composites - in which the filler is smaller than 100 nm in at least one dimension. Some nanofilled composites (carbon black [1] and fumed silica [2] filled polymers) have been used for more than a century, but research and development of nanofilled polymers has greatly increased in recent years, for several reasons. First, unprecedented combinations of properties have been observed in some polymer nanocomposites [3]. For example, the inclusion of roughly spherical nanoparticles in thermoplastics, and particularly in semi crystalline thermoplastics, increases the yield stress, the tensile strength, and Young's modulus compared to pure polymer. A volume fraction of only 0.04 mica-type silicates in epoxy increases the modulus below the glass transition temperature by 58% and the modulus in the rubbery region by 450 % [4]. A second reason for the large increase in research and development efforts was the "discovery" of carbon nanotubes in the early 1990s and their subsequent usage in composite materials [5]. The properties of these carbon nanotubes, strength and electrical properties in particular, offer exciting possibilities for new composite materials. Third, significant development in the chemical processing of nanoparticles and in the in situ processing of nanocomposites has led to unprecedented control over the morphology of such composites, it has also created an almost unlimited ability to control in principle the interface between the matrix and the filler.

Thus, this is an exciting time to study nanocomposites, because of the unique combinations of properties that are achievable and also because of the high potential for successful commercial development. Scientists now have the ability to change the size, shape, volume fraction, interface, and degree of dispersion or aggregation of fillers. Thus, the opportunities may well become limitless when theory and experiment have assembled enough information to guide further development.

A relevant question to ask is: What is unique to nano-fillers compared to

micrometer-scale traditional fillers, and how do the nanocomposites compare to their macroscopic counterparts? The most obvious difference is the small size of the fillers. For example, very small nanoparticles do not scatter light significantly, and thus it is possible to make composites with altered electrical or mechanical properties that retain their optical clarity. In addition, the small size means that the particles do not create large stress concentrations and thus do not compromise the ductility of the polymer. A similar concept applies for electrical breakdown strength.

A substantial difference compared to bigger particles and a main motivation for the present work is the fact that the small size of the fillers leads to an exceptionally large interfacial area in the composites.

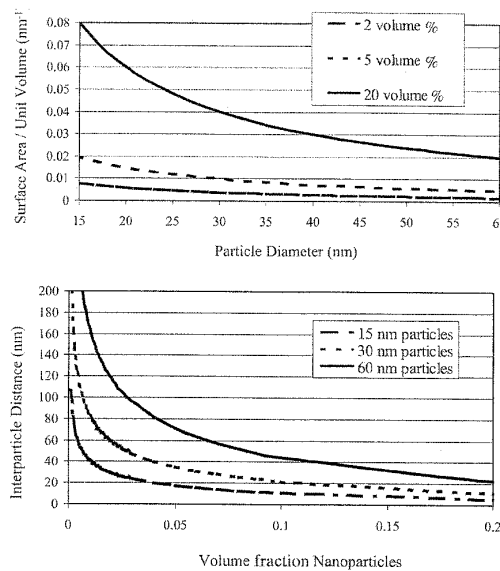


Figure 1.1: Surface area per unit volume and particle particle distance as a function of particle size and volume fraction for spherical particles that are ideally dispersed

Figure 1.1, top shows the surface area per unit volume as a function of particle size for spherical particles that are ideally dispersed. The increase in surface area below 100 nm is dramatic. The interface controls the degree of interaction between the filler and the polymer and thus controls the properties. Therefore the greatest challenge in developing polymer nanocomposites may be learning to control the interlace. Thus, it seems relevant to define the interfacial region and discuss its properties. As defined in traditional composites, the interfacial region is the region beginning at the point in the filler at which the properties differ from those of the bulk filler and ending at the point in the matrix at which the properties become equal to those of the bulk matrix. It can be a region of altered chemistry, altered polymer chain

mobility, altered degree of cure, and altered crystallinity. Interface size has been reported to be as small as 2 nm and as large as about 50 nm. Figure 1.1, bottom shows inter particle spacing as a function of particle size for an ideally dispersed nanoparticle composite: at low volume fractions the entire matrix is essentially part of the interfacial region. For example, for 15 nm particles at a filler loading of 10 vol %, the inter particle spacing is only 10 nm. Even if the interfacial region is only a few nanometers, very quickly the entire polymer matrix has a different behavior than the bulk. If the interfacial region is more extended, then the polymer matrix behavior can be altered at much smaller loadings. Therefore, by controlling the degree of interaction between the polymer and the nanofiller, the properties of the entire matrix can be controlled.

In order to understand the properties of confined polymers, much experimental and computational effort has been devoted to the study of thin polymer films. This interest originates in part from the many technological applications of these systems, and in part from some fundamental questions associated with the influence of confinement on physical processes. Some of the numerous applications of polymer films are protective coatings, scaffold structure in microelectronic devices and membranes in vesicles used for drug delivery. Moreover, as in polymer based nanocomposite materials, most of the “polymer” component is actually confined in the form of thin layers squeezed between the fillers, the study of thin films provides clues for explaining the complex physics in these heterogeneous materials. On the fundamental side, much of the interest has focused on the influence of confinement on the glass transition temperature. In spite of many difficulties in the interpretation of early results, a clear consensus seems now to have emerged, that the glass transition temperature is reduced, and the dynamics accelerated, in the vicinity of a free interface. This observation has been confirmed by several different experimental techniques and molecular simulations. In the case of supported films, strong interaction with the substrate may counterbalance the effect of the free surface.

Many unique properties of the polymer matrix are related to the chain-like nature of polymer molecules and the fact that they form entanglements. Entanglements of polymer chains are topological constraints to motion that have a profound effect on the mobility of the molecules [6]. Qualitatively, they can be viewed as crossings of polymer chains that remain intact when the material is subject to strain and so are mechanically active. They therefore strongly influence dynamic properties of polymer melts such as viscosity and diffusion. The main glassy state properties that are influenced by entanglements are the high strain properties, such as natural draw ratio, craze extension ratio, and toughness. In molten polymeric systems, above the glass transition, dynamics is dominated by chain connectivity and entanglement effects. The density of entanglements, often described by the molecular weight of a chain between entanglements  $M_e$ , can be obtained

from the plateau modulus of a high molecular weight melt. The mean distance between entanglements serves as the tube diameter within the dominant reptation model of polymer dynamics. Entanglement in the polymer bulk is reasonably well understood in broad terms [7], but the situation at an interface, surface or in a thin film is much less clear. Some theoretical assumptions have been put forward [8] suggesting that the entanglement density should vary near an interface, but experimental results exist only for a limited number of cases [9]. Experimental verification of such effects is difficult, as entanglements are not directly observable. Conflicting conclusions have been reached from several different mechanical determinations [9, 10, 11] and spectroscopic methods [12]. While the spectroscopic methods probe mostly the overlap between different chains, the mechanical approach is more directly linked to the entanglement concept used in rheology. Some of these studies imply that the rubber modulus is decreased, or the entanglement distance (as measured from the extension before rupture) decreased, in confined films [9]. Using a bubble inflation method for the determination of viscoelastic properties, O'Connell and McKenna [10] conclude that the compliance is drastically reduced in thin films, which would rather correspond to an increase in entanglement density. Finally, experiments on the spreading of thin films on a liquid substrate [11] conclude that this modulus is not affected, while the terminal relaxation time is. Some distinctions between interchain and intra-chain entanglements have been proposed in order to reconcile these different results. The behavior of the entanglement network in a filled polymer melt is unclear. Some experimental results suggest that it can remain to a large extent unaffected for a certain filler type [13], or be subject to variation in the case of strong filler polymer interaction [14].

In summary, the interfacial region is complex, and when the interfacial area is very large, the whole polymer matrix may essentially be interfacial region. This presents one of the essential challenges in polymer nanocomposites: to develop technology to control the interface, to describe the interface mathematically, and to be able to predict properties taking into account the interfacial region. Traditional composite theory, although very far advanced in describing properties that are relatively independent of the interface, is still in its infancy in taking into account the role of the interfacial region. A number of open questions remain concerning the understanding of the interaction of polymers with flat surfaces. The interaction of polymers with highly curved surfaces and at scales similar to that of the radius of gyration is also not well understood.

### 1.1.2 Nanofluids

Nanofluids are solid-liquid composite materials consisting of solid nanoparticles or nano fibers with sizes typically of 1-100 nm suspended in liquid. Nanofluids have been proposed as a route for surpassing the performance

of heat transfer liquids currently available. Cooling is one of the most important technical challenges facing many diverse industries. Technological developments such as microelectronic devices with smaller (sub-100 nm) features and faster (multi-gigahertz) operating speeds, higher-power engines, and brighter optical devices are driving increased thermal loads, requiring advances in cooling. The conventional method for increasing heat dissipation is to increase the area available for exchanging heat with a heat transfer fluid. However, this approach requires an undesirable increase in the thermal management system's size. There is therefore an urgent need for new and innovative coolants with improved performance. The novel concept of nanofluids has been proposed as a means of meeting these challenges. Recent experiments on nanofluids have indicated significant increases in thermal conductivity compared to liquids without nanoparticles or larger particles. Some of the experimental results are controversial, the extent of thermal conductivity enhancement sometimes greatly exceeds the predictions of well-established theories (fig. 1.2).

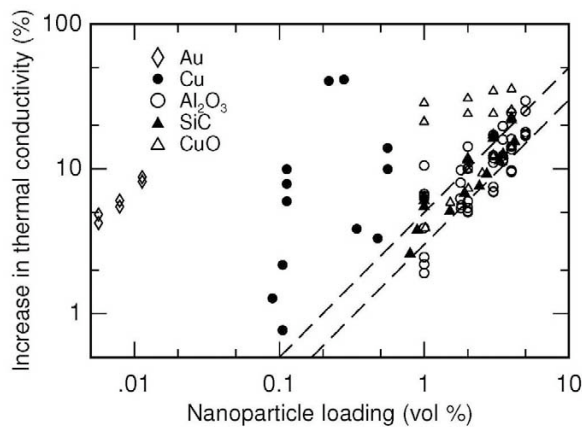


Figure 1.2: Relative increase in the thermal conductivity as a function of the volume fraction of nanoparticles. The lower dashed line is the prediction from effective medium theory for well-dispersed suspensions of highly thermally conductive nanoparticles; the upper dashed line is the prediction for random-close-packed aggregates of nanoparticles. Most of the data is reasonably well described by effective medium theory. The most anomalous results (furthest left and above the dashed lines) for Cu and Au nanoparticle suspensions are [15] and [16].

For example, a small amount (about 1% volume fraction) of Cu nanoparticles or carbon nanotubes dispersed in ethylene glycol or oil is reported to increase the inherently poor thermal conductivity of the liquid by 40% and 150%, respectively [15, 17]. Conventional particle-liquid suspensions require high concentrations (higher than 10%) of particles to achieve such enhance-

ment. There are problems of rheology and stability at high concentrations, making the possibility to use nanofluids even more attractive. In contrast with the highly optimistic results many researchers report “normal” thermal behavior of nanoparticle suspensions [18] (fig. 1.2). If these exciting results on nanofluids can be confirmed in future systematic experiments, new theoretical descriptions may be needed to account properly for the unique features of these materials. These enhanced thermal properties are not merely of academic interest. If confirmed and found consistent, they would make nanofluids promising for applications in thermal management.

The rather controversial findings have stimulated computational and theoretical studies trying to explain the microscopic mechanisms behind the increase in thermal properties. Among the possibilities that were suggested, the Brownian motion [19] of a single sphere in a liquid leads to an increase in thermal conductivity on the order of 4–5%, and appears to be an attractive and generic explanation. The essential idea is that the Brownian velocity of the suspended particle induces a fluctuating hydrodynamic flow [20, 21], which on average influences (increases) thermal transport. This mechanism is different from transport of heat through center of mass diffusion, which was previously shown to be negligible [22]. However, some experimental high precision studies question the validity of this assumption [18]. Recent simulations also showed that normal conductivity is expected for low volume fractions (around 3.3%) and the physical parameter determining thermal properties should be the particle interfacial thermal resistance [23]. However a method providing quantitative data on the particles interfacial resistance and its dependence on physical properties is still missing. Such data should allow direct quantitative prediction of the thermal properties. Also, studying the fluid conductivity when precisely controlling the diffusion of particles can further elucidate the heat transfer mechanisms in nanofluids and clarify the role of Brownian motion. Another possible explanation of the peculiar thermal behavior of nanofluids lies in collective effects. This field is generally rather complex but some insights in the possible mechanisms involved can be achieved in a study of systems with a small number of particles.

## 1.2 Methods

The characterization and study of nanocomposites involves many different fields of materials science. Among them computer simulations have a noticeable place with growing importance. Computation is now an integral part of contemporary science, and is having a profound effect on the way we do physics, on the nature of the important questions, and on the physical systems we choose to study. Developments in computer technology are leading to new ways of thinking about physical systems.

We carry out computer simulations in the hope of understanding the

properties of assemblies of molecules in terms of their structure and the microscopic interactions between them. This serves as a complement to conventional experiments, enabling us to learn something new, something that cannot be found out in other ways.

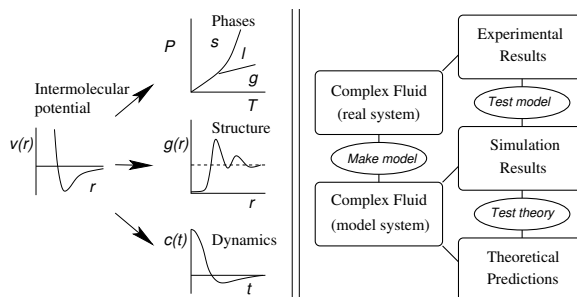


Figure 1.3: Simulations as a bridge between microscopic and macroscopic on one hand and theory and experiment on the other.

Computer simulations act as a bridge (see fig. 1.3) between microscopic length and time scales and the macroscopic world of the laboratory: we provide a guess at the interactions between molecules, and obtain “exact” predictions of bulk properties. The predictions are “exact” in the sense that they can be made as accurate as we like, subject to the limitations imposed by our computer budget. At the same time, the hidden detail behind bulk measurements can be revealed. An example is the link between the diffusion coefficient and velocity autocorrelation function (the former easy to measure experimentally, the latter much harder). Simulations act as a bridge in another sense: between theory and experiment. We may test a theory by conducting a simulation using the same model. We may test the model by comparing with experimental results. We may also carry out simulations on the computer that are difficult or impossible in the laboratory. Examples for this are measurements under extreme conditions that are experimentally prohibitive. Simulations can also provide details of molecular motion and structure concerning events that are too fast or too slow to study experimentally.

Ultimately we may want to make direct comparisons with experimental measurements made on specific materials, in which case a good model of molecular interactions is essential. On the other hand, we may be interested in phenomena of a rather generic nature, or we may simply want to discriminate between good and bad theories. When it comes to aims of this kind, it is not necessary to have a perfectly realistic molecular model; one that contains the essential physics may be quite suitable.

The two main families of simulation technique are molecular dynamics (MD) and Monte Carlo (MC); additionally, there is a whole range of hybrid techniques which combine features from both. In this work we mainly use

MD. The obvious advantage of MD over MC is that it gives a route to dynamical properties of the system: transport coefficients, time-dependent responses to perturbations, rheological properties and easily allows non equilibrium simulations. All simulations were performed with the LAMMPS ([Large-scale Atomic/Molecular Massively Parallel Simulator](http://lammps.sandia.gov/)) code (<http://lammps.sandia.gov/>) [24]. It is an open source, rich, flexible and fast simulation software package, that met (modified whenever needed) all the needs of the present work.

### 1.3 Overview

The present work is organized as follows: at first a description of the basic problems and theoretical concepts widely used later will be given. In the second chapter we will discuss in microscopic detail the viscoelastic behavior of a pure bulk polymer material. While exposing comprehensively the molecular mechanisms involved, we will also concentrate on the development and calibration of computational and mathematical tools to be used later. In the third and fourth chapter we will turn to the detailed local study of polymer interfaces and polymer based nanocomposites. We explain the local static and dynamical behavior of the chains in the interfacial region, very important for the macroscopic properties of a nanocomposite. We also study the properties of the entanglement network at an interface as a function of its chemical nature. We discuss model systems of polymer nanocomposites and provide insights about the microscopic basis of reinforcement. In the last chapter we turn to the study of heat transfer in nanofluids, revealing the role of the interface in the enhancement of thermal properties in these materials.



## Chapter 2

# Theoretical background

### Contents

---

<b>2.1</b>	<b>Coarse grained models</b>	<b>11</b>
<b>2.2</b>	<b>Static properties of a polymer</b>	<b>13</b>
<b>2.3</b>	<b>The Rouse model</b>	<b>14</b>
<b>2.4</b>	<b>The reptation concept</b>	<b>18</b>
<b>2.5</b>	<b>Polymer based composites - reinforcement and Payne effect</b>	<b>22</b>

---

In the present section some basic concepts of polymer physics will be described. Also some experimental results and ideas for explaining the composite materials properties will be enumerated. Those concepts are essential for the understanding of the interpretations given in the following chapters, as well as to motivate the particular numerical measurements in the studied systems.

### 2.1 Coarse grained models

Often the simulations of physical systems cannot and do not need to take into account all possible detail and all the degrees of freedom of the real system. Simulating the electrons in the molecules would be irrelevant for determining a liquid's viscosity. Furthermore simulation can become virtually impossible if one takes into account all the chemical details of the system.

This situation is particularly unfavorable in the case of polymers since these long molecules span very different length (and in consequence time) scales (see fig. 2.1). Simulation of specific polymer systems has been greatly advanced by employing systematically derived coarse-grained molecular models. These models vary in the details of their development and implementation, yet all seek to construct particle- or lattice- based chain-like objects

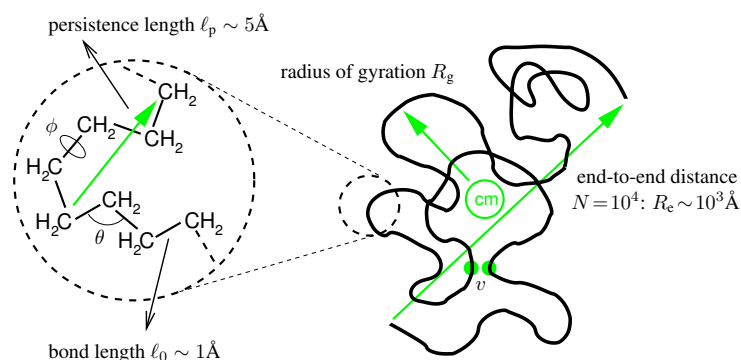


Figure 2.1: Schematic representation of a polymer molecule (polyethylene)

whose constituents represent at most a few chemical repeating units of any specific polymer (see fig. 2.2 and fig. 2.3).

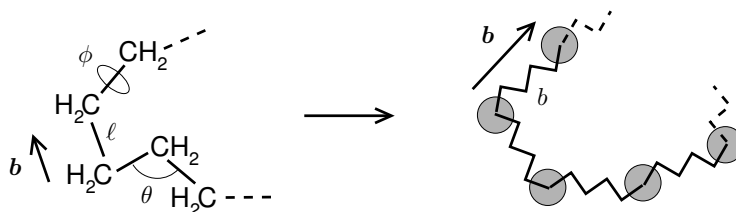


Figure 2.2: From a chemically realistic model to a coarse-grained bead-spring type model. Local properties of the realistic model are determined by its microscopic degrees of freedom:  $l$ ,  $\theta$  and  $\phi$ . On the global level of the chain, however, the influence of the microscopic degrees of freedom can be lumped into one parameter, the effective bond length.

This is meant to circumvent the great difficulty in producing equilibrated samples of atomically-resolved polymers due to the up to ten orders of magnitude spread between the resolution required in time for standard atomistic molecular dynamics (MD) simulation ( $10^{-15}s$ ) and the slow molecular relaxation times ( $\sim 10^{-5}s$ ) which must be achieved. Monte Carlo simulation fares no better as an alternative approach, especially in dense multi-molecular systems, because local moves are constrained to impractically small values by steep bonded potentials, and enormous numbers of successful moves have to accumulate in order to move chain sections larger than a repeat unit or so. Integrating out these fast motions, or put another way, averaging over their underlying steep potentials, allows us in principle to construct models that can produce equilibrated configurations with relatively much less computational effort. Coarse-graining aims to guarantee that the chain conformations in a simulation sample represent true equilibrium conformations of

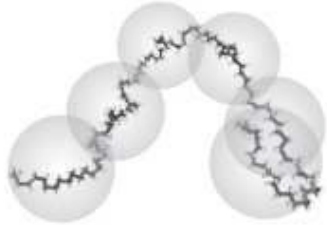


Figure 2.3: Representation of a polymer molecule and a corresponding coarse grained model

the specific polymer considered. A central feature of coarse-graining is that the models retain only as much unique and relevant information as needed about the specific polymer(s) under investigation, using significantly fewer degrees of freedom (i.e., particles) than required for full atomistic detail. The coarsened degrees of freedom must be constrained within ensembles of configurations which represent an appropriate average over the microscopic atomic-scale potential energy surface of the fully resolved system.

## 2.2 Static properties of a polymer

As polymers have a great number of equilibrium conformations, characteristic quantities are defined as statistical mean values.

If we consider a chain as a sequence of non correlated randomly oriented vectors of length  $b_0$  - an ideal (or Gaussian) chain, the mean end-to-end square distance is simply given by  $\langle R^2 \rangle = \langle (\vec{R}_N - \vec{R}_1)^2 \rangle = Nb_0^2$ . If the chain is subject to additional constraints (like fixing the angle between two consecutive segments) the previous relation becomes:

$$\langle R^2 \rangle = Nb^2 \quad (2.1)$$

where  $b$  is the effective segment length. This length is the distance over which correlation is lost in the chain. If we consider for example a freely rotating chain model with an angle  $\theta$  between segments the end to end vector becomes  $\langle R^2 \rangle = Nb_0^2(1 + \cos \theta)/(1 - \cos \theta)$  and the effective bond length in this case is given by  $b = b_0((1 + \cos \theta)/(1 - \cos \theta))^{1/2}$ . The effective bond length depends on one hand on the microscopic structure of the chain, on its stiffness and on the monomer concentration on the other hand. For melt densities close to 1, due to mutual screening of interactions polymers behave like Gaussian chains with their effective bond length function of the microscopic structure alone. The microscopic stiffness of the chain is represented by the ratio

$$C_\infty = b^2/b_0^2 \quad (2.2)$$

This coefficient can be calculated from the local structure of the chain. The stiffness can also be represented by another parameter, the Kuhn statistical segment length defined by:

$$b_K = \langle R^2 \rangle / R_{max} = b^2 / b_0 \quad (2.3)$$

where  $R_{max}$  is the maximum length of the end to end vector. The typical spatial extension of a polymer chain is given by its radius of gyration:

$$R_g^2 = \frac{1}{N} \sum_{n=1}^N \langle (\vec{r}_n - \vec{r}_{CM})^2 \rangle \quad (2.4)$$

where  $r_{CM}$  is the position of the center of mass of the chain. The radius of gyration is also the mean square distance between all pairs of the segments of the chain:

$$R_g^2 = \frac{1}{2N^2} \sum_{n,m=1}^N \langle (\vec{r}_n - \vec{r}_m)^2 \rangle \quad (2.5)$$

This relation can easily be obtained by replacing the expression for the center of mass in equation 2.4 and developing. For a linear polymer, if we assume Gaussian behavior on all length scales,  $R_g$  can easily be calculated:

$$\begin{aligned} R_g^2 &= \frac{1}{2N^2} \sum_{n,m=1}^N |n - m| b^2 \\ &= \frac{1}{2N^2} \int_0^N dn \int_0^N dm |n - m| b^2 \\ &= \frac{1}{N^2} \int_0^N dn \int_0^N dm (n - m) b^2 \\ &= \frac{1}{6} N b^2 \end{aligned} \quad (2.6)$$

Thus the typical dimension of the linear polymer is given by  $\bar{R}/\sqrt{6}$ .

### 2.3 The Rouse model

The motion of a single monomer is governed by the connectivity of the chain and the interaction of the monomer with its surroundings. In a simple model, called the Rouse model [25], one can think that for such a situation all the complicated non-bond interactions are adsorbed into a monomeric friction and a coupling to a heat bath. In this entropy governed model the motion of the bead is described by a Langevin equation:

$$\zeta \frac{\partial \vec{r}_i}{\partial t} = -\nabla U(\{\vec{r}_i\}) + \vec{f}_i(t) \quad (2.7)$$

where  $r_i$  denotes the position of monomer  $i$ ,  $\zeta$  is the friction coefficient with the viscous background,  $U$  is the bond potential that keeps the chain connected and  $\vec{f}_i(t)$  is a random Langevin force related to  $\zeta$  via a fluctuation-dissipation relation. If we consider the case of a harmonic bond potential:  $U(\vec{r}) = -k \frac{\partial^2 \vec{r}}{\partial i^2}$  where  $k = 3k_B T/b^2$  is the spring stiffness ( $b$  is the bond length) the model can be solved exactly. The choice of this potential comes from the idea that interactions in the coarse grained chain backbone are due to entropic springs. Taking free boundary conditions and rewriting the equation (2.7) in terms of vibration modes one has:

$$2N\zeta \frac{\partial \vec{X}_0}{\partial t} = \vec{g}_0 \quad (2.8)$$

$$2N\zeta \frac{\partial \vec{X}_p}{\partial t} = -k_p \vec{X}_p + \vec{g}_p, \quad p > 0 \quad (2.9)$$

where  $k_p = k6Np^2\pi^2/(Nb)^2$ ,  $\vec{g}_p$  is a random force and the proper modes  $\vec{X}_p$  are related to positions by:

$$\vec{X}_p = \frac{1}{N} \int_0^N dn \vec{R}_n(t) \cos\left(\frac{np\pi}{N}\right) \quad (2.10)$$

From equations (2.9) the time correlation functions of the modes can be calculated:

$$\langle X_{p,i}(t) X_{q,j}(0) \rangle = \frac{k_B T}{k_p} \delta_{ij} \delta_{pq} \exp(-t/\tau_p) \quad (2.11)$$

Finally, 2.11 yields the diffusion constant of the center of mass of the chain

$$D = k_B T / N\zeta \quad (2.12)$$

and the relaxation time of the mode  $p$ :

$$\tau_p = \frac{\zeta N^2 b^2}{3\pi^2 k_B T p^2} = \frac{\zeta N \langle R^2(N) \rangle}{3\pi^2 k_B T p^2} \quad (2.13)$$

The largest relaxation time  $\tau_1 = \tau_R$  is called Rouse time. The times  $\tau_p$  can be viewed as the relaxation times of a chain of length  $N/p$  monomers.

The evolution of the mean square displacement of a single monomer  $g_1(t)$

$$g_1(t) = \frac{1}{N} \sum_{i=1}^N \langle (\vec{r}_i(t) - \vec{r}_i(0))^2 \rangle \quad (2.14)$$

with time is governed by the fact that as time increases an increasing number of monomers have to be carried along. As the chain structure is that of a random walk, one can show that:

$$g_1(t) \propto \begin{cases} t^1, & t < \tau_0, g_1(t) < a^2 \\ t^{1/2}, & \tau_0 < t < \tau_R, g_1(t) < \langle R^2 \rangle \\ t^1, & t > \tau_R, g_1(t) > \langle R^2 \rangle \end{cases} \quad (2.15)$$

It turns out experimentally that this simple model provides an excellent description of polymer dynamics in the case of a melt and provided that the chains are short enough. The calculation above made in the continuous limit has to be slightly modified to be used in simulations. For the discrete polymer models we will be considering the Rouse modes can be written as [26]:

$$\vec{X}_p(t) = \frac{1}{N} \sum_{n=1}^N \vec{r}_n(t) \cos\left(\frac{(n-1/2)p\pi}{N}\right), \quad p = 0, \dots, N-1 \quad (2.16)$$

with  $N$  the chain length,  $\rho$  the monomer number density and  $\vec{r}_n(t)$  - the position of the  $n$ -th monomer in the chain at the time  $t$ . In this case the mean square value of a mode  $p$  is:

$$\langle X_p^2 \rangle = \frac{b^2}{8N(\sin p\pi/2N)^2} \xrightarrow{p/N \ll 1} \frac{Nb^2}{2\pi^2 p^2} \quad (2.17)$$

and the relaxation time of the mode is given by:

$$\tau_p = \frac{\zeta b^2}{12k_B T (\sin p\pi/2N)^2} \xrightarrow{p/N \ll 1} \frac{\zeta N^2 b^2}{3\pi^2 k_B T p^2} \quad (2.18)$$

The modes calculated in a simulated melt remain orthogonal to each other. This was tested in the present study by measuring cross correlations between modes  $p$  and  $q \neq p$ . The value of the resulting function is about two to three orders of magnitude smaller than the autocorrelation of the modes.

### Microscopic expression for the stress tensor

An essential quantity for the study of the viscoelastic properties of a material is the stress tensor. We will briefly present here a rather general definition of the stress and see how it can be related to the Rouse modes. We consider a small portion of fluid, small enough for all macroscopic gradients to be zero, and large enough to represent a homogeneous phase. Now let us consider the quantity (virial):

$$A_{\alpha\beta} = \left\langle \frac{1}{V} \frac{d}{dt} \sum_i m_i r_\alpha^i v_\beta^i \right\rangle$$

where the average is an ensemble average, or a time average over a time span long enough to smooth out fluctuations, and short enough to assume that the macroscopic flow is stationary. The sum is over all particles in our control volume, i.e. particles leaving the control volume are from that moment on left out of the sum, and particles entering the control volume will from that moment on contribute to the sum. Since in this case  $\sum m_i r_\alpha^i v_\beta^i$  is a bounded quantity, with a well defined average, the average of its time variation must

be zero, i. e.  $A_{\alpha\beta} = 0$  for  $\alpha, \beta = x, y, z$ . Evaluating the derivative we obtain:

$$0 = \left\langle \frac{1}{V} \sum_i v_\alpha^i v_\beta^i \right\rangle + \left\langle \frac{1}{V} \sum_i m_i r_\alpha^i \frac{dv_\beta^i}{dt} \right\rangle \quad (2.19)$$

We can quite generally divide the forces acting on a particle  $i$  in two parts: internal and external to the considered volume  $\vec{F}_i = m_i d\vec{v}_i/dt = \vec{F}_i^{int} + \vec{F}_i^{ext}$ . The stress tensor component  $\sigma_{\alpha\beta}$  is defined as the  $\alpha$  component of the force (per unit area) that the material above a plane perpendicular to the  $\beta$  direction exerts on the material below this plane. In this case, assuming that the net flow is zero (zero average macroscopic velocity), the stress is given by:

$$\sigma_{\alpha\beta} = \left\langle \frac{1}{V} \sum_i r_{i,\alpha} F_{i,\beta}^{ext} \right\rangle$$

Reintroducing this term in equation 2.19 we obtain the microscopic expression for the stress:

$$\sigma_{\alpha\beta} = -\left\langle \frac{1}{V} \sum_i v_\alpha^i v_\beta^i \right\rangle - \left\langle \frac{1}{V} \sum_i r_\alpha^i F_\beta^i \right\rangle \quad (2.20)$$

At melt densities the first term in equation 2.20 associated with convective motion is usually negligible. The second term can be rewritten as

$$\sigma_{\alpha\beta} = \frac{\rho}{N} \sum_1^N \left\langle \frac{\partial U}{\partial r_{n,\beta}} r_{n,\alpha} \right\rangle \quad (2.21)$$

where  $N$  is the chain length and  $\vec{r}_n$  is the position of the  $n$ th monomer of the chain. The prefactor accounts for the number of polymer molecules per unit volume. Assuming that the interaction potential is the same coarse grained entropic spring potential in the previous section, this expression is transformed into:

$$\begin{aligned} \sigma_{\alpha\beta} &= \frac{\rho}{N} \frac{3k_B T}{b^2} \sum_1^N \left\langle -(\vec{r}_{n+1} + \vec{r}_{n-1} - 2\vec{r}_n)_\beta r_{n,\alpha} \right\rangle \\ &= \frac{\rho}{N} \frac{3k_B T}{b^2} \sum_1^N \left\langle (\vec{r}_{n+1} - \vec{r}_n)_\alpha (\vec{r}_{n+1} - \vec{r}_n)_\beta \right\rangle \end{aligned} \quad (2.22)$$

or in the continuous limit

$$\sigma_{\alpha\beta} = \frac{\rho}{N} \frac{3k_B T}{b^2} \int_0^N dn \left\langle \frac{\partial r_{n,\alpha}}{\partial n} \frac{\partial r_{n,\beta}}{\partial n} \right\rangle \quad (2.23)$$

Strictly speaking, one has to add an excluded volume interaction to the potential  $U$ . Let us model the excluded volume by the potential:

$$U_V = \frac{v}{2} k_B T \sum_{m,n} \delta(\vec{r}_n - \vec{r}_m) \quad (2.24)$$

the stress arising from this potential can be neglected because:

$$\begin{aligned}
\left\langle \sum_n \frac{\partial U_V}{\partial r_{n,\alpha}} r_{n,\beta} \right\rangle &= \frac{v}{2} k_B T \sum_{m,n} \left\langle \left( \frac{\partial}{\partial r_{n,\alpha}} \delta(\vec{r}_n - \vec{r}_m) \right) r_{n,\beta} \right\rangle \\
&= \frac{v}{4} k_B T \sum_{m,n} \left\langle \left( \frac{\partial}{\partial r_{n,\alpha}} \delta(\vec{r}_n - \vec{r}_m) \right) (r_{n,\beta} - r_{m,\beta}) \right\rangle \\
&= \frac{v}{4} k_B T \sum_{m,n} \left\langle \frac{\partial}{\partial r_{n,\alpha}} [\delta(\vec{r}_n - \vec{r}_m) (r_{n,\beta} - r_{m,\beta})] \right\rangle \\
&\quad - \frac{v}{4} k_B T \sum_{m,n} \langle \delta(\vec{r}_n - \vec{r}_m) \delta_{\alpha\beta} \rangle \tag{2.25}
\end{aligned}$$

the first term in equation 2.25 is zero and the second term can be omitted because it is isotropic. Therefore the expression 2.23 holds even for the chain with the excluded volume effect. This of course does not mean that the excluded volume does not have any effect on the stress tensor, it does play a role via the distribution function over which the average in equation 2.23 is taken. Finally we can rewrite 2.23 in normal coordinates, using the modes:

$$\begin{aligned}
\sigma_{\alpha\beta} &= \frac{\rho}{N} \frac{3k_B T}{b^2} \sum_{p,q} 4 \frac{p\pi}{N} \frac{q\pi}{N} \langle X_{p\alpha}(t) X_{q\beta}(t) \rangle \\
&\quad \times \int_0^N dn \sin \frac{p\pi n}{N} \sin \frac{q\pi n}{N} \\
&= \frac{\rho}{N} \sum_p k_p \langle X_{p\alpha}(t) X_{p\beta}(t) \rangle \\
&= \frac{\rho k_B T}{N} \sum_p \frac{\langle X_{p\alpha}(t) X_{p\beta}(t) \rangle}{\langle X_{p\alpha}^2 \rangle} \tag{2.26}
\end{aligned}$$

## 2.4 The reptation concept

If longer chains are considered, other important effects change the dynamics and they are no longer predicted by the Rouse model. Entanglement effects become important when chains exceed significantly an entanglement length  $N_e$ . The motion is slowed down drastically, experimentally one finds  $D \propto N^{-2}$  and  $\eta \propto N^{3.4}$  (see fig. 2.4). The reptation concept [28] gives a nice physical picture for this slowing down. The idea is that the chain moves mainly along its own contour. The reason for this is that the topology of the surroundings, due to entangled chains, suppresses the motion transverse to its contour (see fig. 2.5). This contour is called primitive path and its characteristics are crucial for the rheological properties of the material. The quantity characterizing the microscopic topology of an entangled melt is the

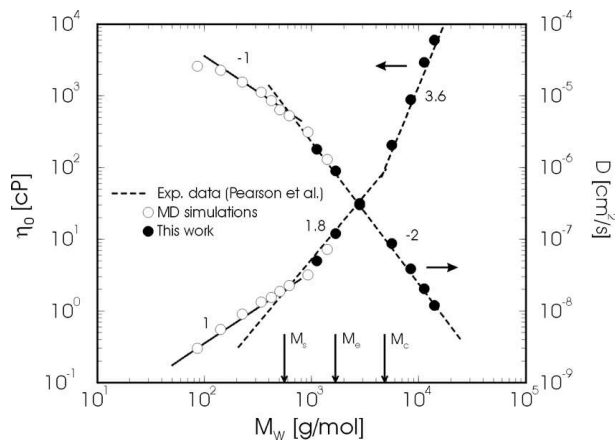


Figure 2.4: Evolution of the diffusion coefficient and the viscosity with the chain length (data from [27])

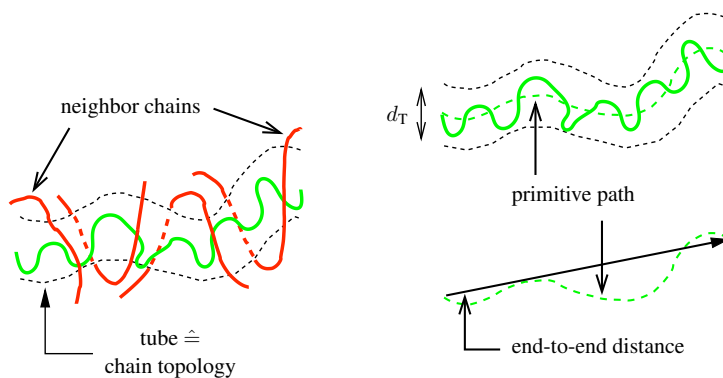


Figure 2.5: Representation of the chain primitive path.

entanglement length - the number of monomer units between entanglements  $N_e$  (and also its related quantities such as the tube diameter). Here we present a calculation of these quantities inspired by ref. [29] and ref. [6, 30]. The following model is based on the idea that there is a relation between the sizes of the polymer coils and the degree to which they are entangled with each other. Basically, the idea is that the larger the dimensions of a chain, the greater the volume it sweeps out, so the greater the number of other chains it will encounter and with which it might entangle. This requires a knowledge of the volume the chain occupies (just given by  $1/\rho_{ch}$ , with  $\rho_{ch}$  the number of chains per unit volume) and also the volume “pervaded” by the chain, that is, the volume spanned by the chain, which is quite difficult to calculate. Here we will approximate this volume by  $V_{sp}$ , the volume of the smallest sphere which completely contains the chain. We assume this is

proportional to the cube of the radius of gyration:

$$V_{sp} = A \times R_G^3 \quad (2.27)$$

where  $A$  is a constant of order unity. Let  $n_{ch}$  be the number of chains of length  $N$  that would completely fill a volume  $V_{sp}$ . Then we have

$$n_{ch} = V_{sp} \rho_{ch} \quad (2.28)$$

Now  $n_{ch} - 1$  can also be considered as the number of chains with which a particular chain is entangled, since that is the number of other chains that are in the volume it pervades. In a highly entangled melt,  $n_{ch}$  will be a large number. For shorter chains, there is less entanglement and  $n_{ch}$  becomes smaller. We may now ask, what is the number of chains  $n_{ch}$  in  $V_{sp}$  when  $N = N_e$ ? Let us define  $N_e$  as the length of a chain at which  $n_{ch} = 2$ , that is, when there is just one other chain in the spanned volume. For  $N < N_e$ , there is thus no full chain in that volume, so there is no entanglement. Using equation 2.6 this leads to the following expression:

$$V_{sp}(N_e) \rho / N_e = \frac{A}{\sqrt{6}} b^3 \sqrt{N_e} \rho = 2 \quad (2.29)$$

and thus the entanglement length is

$$N_e = \frac{24}{A^2} \frac{1}{b^6 \rho^2} \quad (2.30)$$

We see that this parameter depends only on the microscopic structure of the polymer. To quantify the bulkiness of the polymer we can define a microscopic characteristic length called the packing length:

$$p = \frac{v_0}{b^2} = \frac{1}{\rho b^2} = \frac{1}{\rho_{ch} \langle R^2 \rangle} \quad (2.31)$$

where  $v_0$  is the volume of a monomer and  $b$  is the effective bond length (equation 2.1). So the universal relation between the microscopic structure and the entanglement length is

$$N_e \propto p^3 \rho \quad (2.32)$$

and the tube diameter or equivalently the Kuhn length of the primitive path is given by

$$\begin{aligned} d_T^2 = a_{pp}^2 &= N_e b^2 \\ &= \frac{\langle R^2 \rangle}{L_{pp}} \\ &= N_e b_0 b_K \end{aligned} \quad (2.33)$$

where  $L_{pp}$  is the length of the primitive path.

From a dynamical point of view for short time scales the motion of the chain cannot be distinguished from that of a Rouse chain. The typical time for the onset of entanglement constraint motion is  $\tau_e \propto N_e^2$ . As a result one has Rouse like behavior for short times, then a Rouse random walk relaxation along a coarse grained structure of displacements of length  $d_T$  so that the power law for  $g_1(t)$  becomes a  $t^{1/4}$  power law. On this time scale the chain is going back and forth in the reptation tube - the so called "local reptation". After the chain along this coarse grained path is relaxed ( $t > \tau_R \propto N^2$ ), it has only moved a distance on the order of the square root of the contour length of the tube. Then an overall diffusion along the tube yields a second  $t^{1/2}$  regime for the motion in space. Finally, after a time  $\tau_d \propto N^3/N_e$ , called the disentanglement time, an overall diffusion in space takes place - on this time scale the chain "reptates out" of the initial tube it was constraint in. Thus the following general power law is expected:

$$g_1(t) \propto \begin{cases} t^1, & t < \tau_0 \\ t^{1/2}, & t < \tau_e \sim N_e^2 \\ t^{1/4}, & t < \tau_R \sim N^2 \\ t^{1/2}, & t < \tau_d \sim N^3/N_e \\ t^1, & t > \tau_d \end{cases} \quad (2.34)$$

The presence of entanglements is experimentally well seen in the stress autocorrelation function:

$$G(t) = \frac{V}{k_B T} \langle \sigma_{\alpha\beta}(t) \sigma_{\alpha\beta}(0) \rangle, \quad \alpha \neq \beta \quad (2.35)$$

This function displays a plateau for  $\tau_e < t < \tau_d$  called the plateau modulus  $G_N^0$  that is related to the presence of entanglements (see fig. 2.6).

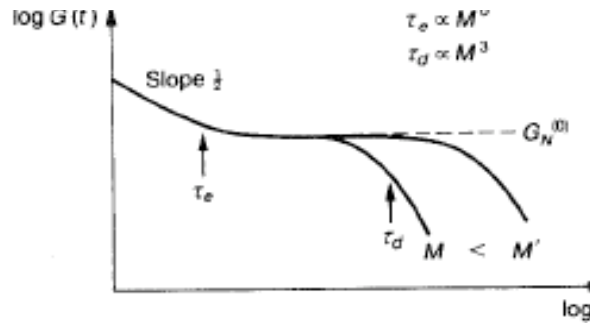


Figure 2.6: A log-log plot of the stress correlation function as a function of time as predicted by the reptation theory

Its value is given by: [31]

$$G_N^0 = \frac{4}{5} \rho \frac{k_B T}{N_e} = \frac{4}{5} \rho k_B T \frac{b^2}{a_{pp}^2} \quad (2.36)$$

However, the reptation idea leaves some unanswered questions. The measured viscosity scales as  $N^{3.4}$ , contradicting the fact that the largest relaxation time  $\tau_d \propto N^3$ . It is essentially a single chain scenario and the idea of rigid topological obstacles forming the entanglements is still under discussion. It is clear that the background moves as well and this leads to release and reconstruction of constraints. Still the reptation idea remains the simplest physical frame partially explaining the dynamics of long chains.

## 2.5 Polymer based composites - reinforcement and Payne effect

It has long been known that the addition of filler to a polymer matrix results in reinforcement and nonlinear viscoelastic behavior. In 1960 Payne [32] investigated the amplitude dependence of the shear moduli of elastomers filled with carbon black. When an oscillatory stress is applied to a linear viscoelastic material the strain will oscillate out of phase with the stress. The strain,  $\gamma$ , and stress,  $\sigma$ , can be written as

$$\gamma = \gamma_0 e^{i\omega t} \quad (2.37)$$

$$\sigma = \sigma_0 e^{i(\omega t + \delta)} \quad (2.38)$$

The complex shear modulus is defined as the stress-strain ratio

$$G^* = \sigma(t)/\gamma(t) = \sigma_0/\gamma_0 e^{i\delta} = G' + iG'' \quad (2.39)$$

where  $G'$  is the storage modulus

$$G' = \sigma_0/\gamma_0 \cos \delta \quad (2.40)$$

and  $G''$  is the loss modulus

$$G'' = \sigma_0/\gamma_0 \sin \delta \quad (2.41)$$

$\sigma_0$  and  $\gamma_0$  are the maximum amplitudes of stress and strain respectively. The loss factor is defined as

$$\text{loss factor} = \tan \delta = G''/G' \quad (2.42)$$

that is, the ratio of energy lost to energy stored.

The addition of even a small portion of fillers in a polymer melt leads to a substantial increase of the storage and loss modulus. This phenomenon is known as reinforcement and is one of the main reasons for the wide interest in filled polymer melts. Another effect is related to the behavior of reinforcement for different shear strain amplitudes. For a linear viscoelastic material (such as an unfilled rubber for shear deformation smaller than about

## 2.5. Polymer based composites - reinforcement and Payne effect 23

10%), the response depends only on the frequency of the imposed oscillation. However for filled rubbers the response is also known to depend upon the dynamic strain amplitude. Thus they are termed nonlinear viscoelastic materials. The resulting behavior is known as the Payne effect. The storage modulus decreases monotonically with amplitude while the loss modulus has a maximum at a certain amplitude (see fig. (2.7), (2.8)). The nature of

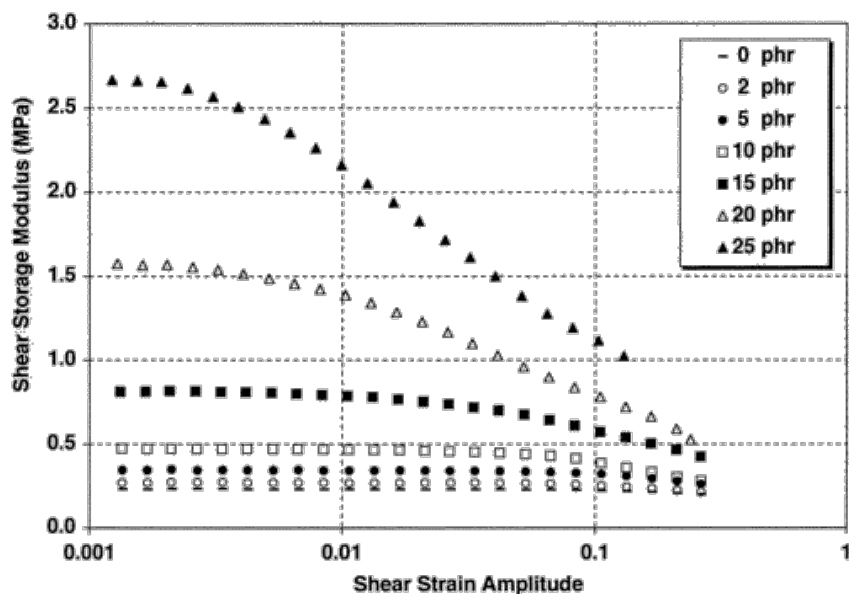


Figure 2.7: Shear storage modulus vs shear strain amplitude at 90 C and 5 Hz for NT-380 silica filled 83K PVAc from 0 to 25 phr. [33]

the reinforcement mechanism remains an open question. It has long been believed that reinforcement is caused by agglomeration and network formation of the filler particles [34]. Experimental evidence has indeed shown that agglomeration and percolation occur at sufficiently high filler concentration. In addition Payne [32] showed that reinforcement also occurs in non polymeric liquids (n-decane and liquid paraffins) with a filler concentration of 28 vol%. As Payne did not concentrate at lower filler concentrations this is taken as evidence that the Payne effect can be caused by agglomeration and/or network formation without regard to interaction between filler and polymer.

However, more recently the Payne effect has been observed even at very low filler concentrations (below 12.5% - well below the percolation threshold) [33]. In this limit filler particles are assumed to reside far from one another and thus the most probable mechanism involves interaction between individual particles and the polymer matrix. In addition the shear moduli varies continuously with filler concentration, arguing against an effect which

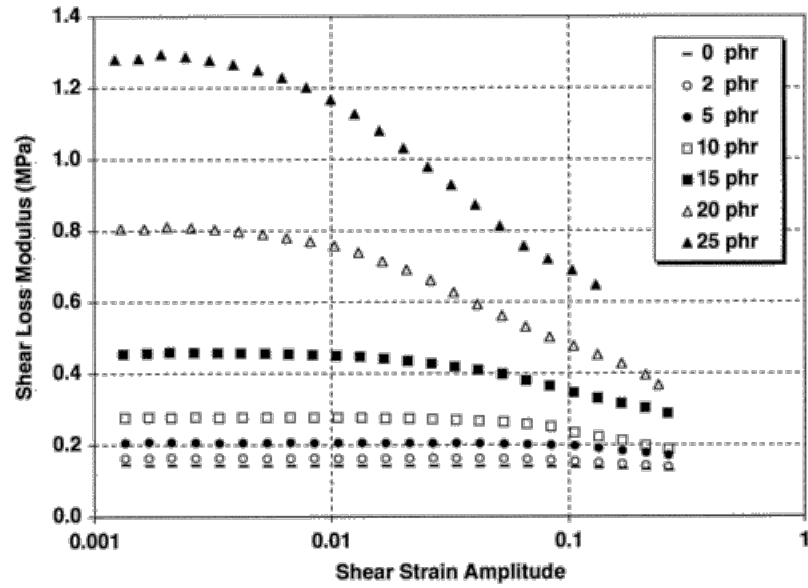


Figure 2.8: Shear loss modulus vs shear strain amplitude at 90 C and 5 Hz for NT-380 silica filled 83K PVAc from 0 to 25 phr. [33]

occurs at the percolation threshold. An explanation of reinforcement in this case has been proposed for temperatures close to the glass transition temperature of the matrix [35]. A shift of the glass transition temperature can occur at the filler matrix interface thus leading to the formation of glassy bridges (see fig. 2.9). Still this explanation is not universal. For example the reinforcement shown in fig. 2.7, 2.8 has been measured for  $T \geq 2T_g$  of the polymer matrix [36, 33, 37]. The authors propose an explanation in terms of trapped entanglements near the filler particles (see fig. 2.10).

## 2.5. Polymer based composites - reinforcement and Payne effect



Figure 2.9: Schematic representation of reinforcement through glassy bridges. The glassy layers are much tougher than the polymer matrix and their percolation increases the macroscopic mechanical properties of the material.

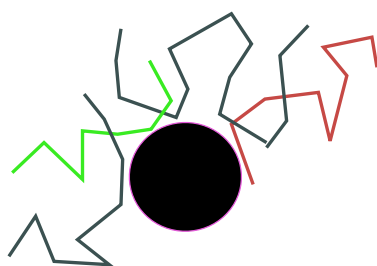


Figure 2.10: Schematic representation of reinforcement through trapped entanglements. The interface changes the number and/or mobility of entanglements thus altering the mechanical properties of the sample.



# Chapter 3

## Viscoelasticity of Pure Polymer Melts

### Contents

---

<b>3.1</b>	<b>Introduction</b>	<b>27</b>
<b>3.2</b>	<b>System description and methods</b>	<b>28</b>
<b>3.3</b>	<b>Viscosity determination by NEMD</b>	<b>32</b>
3.3.1	Green-Kubo approach	35
3.3.2	Rouse modes	38
<b>3.4</b>	<b>Elastic Moduli</b>	<b>43</b>
3.4.1	Method	43
3.4.2	Results	45
<b>3.5</b>	<b>Discussion and Conclusions</b>	<b>52</b>

---

In this chapter we examine the mechanical properties of a bulk polymer material. The study is limited to short chain lengths in the unentangled regime so that a large frequency domain can be explored. An overview of the viscoelastic behavior is given and a new method for studying local viscoelastic properties is developed and discussed.

### 3.1 Introduction

The response of polymer melts to mechanical perturbations, involving either oscillatory or steady flow, is of great practical importance, and has been the object of extensive experimental and theoretical studies [38, 39, 31]. This response is well known to be viscoelastic and non-linear, i.e. the storage and loss moduli exhibit a strong dependence on frequency, shear rate and shear amplitude, with a typical shear thinning behavior for the viscosity.

On the simulation side, the steady state viscosity and shear thinning effects have been studied quite extensively in various configurations for model

systems. An extensive review of recent work is given in reference [40]. A spectacular success was the reproduction of the Rouse-Reptation (or unentangled-entangled) crossover in the rheological behavior for model polymer melts of the bead spring type [41]. This crossover is obtained for chain lengths of the order of  $N = 100$  monomers. According to the popular wisdom in the field, melts with  $N < 100$  should therefore be amenable to a description in terms of the Rouse model, which is considered as a reasonable phenomenological description of unentangled melts.

Investigation of frequency dependent response are much less numerous than for steady state viscosity. In fact we are aware of only one recent study,[42] with objectives similar to those treated in the present chapter. Our aim is to investigate the mechanical response of model polymer melts submitted to steady or oscillatory shear, in order to obtain a characterization in terms of frequency *and* amplitude of the solicitation. In view of the numerical cost of such calculations, our study will be limited to short chains, but will explore several values of amplitudes and frequencies, concentrating on relatively low frequencies.

As it turns out, a direct assessment of mechanical properties using non equilibrium molecular dynamics (NEMD) is very costly from a computational viewpoint. Hence it is desirable to explore methods that could provide the same information with a lesser computational effort. We will in particular explore the possibility of obtaining viscoelastic properties directly from a study of Rouse modes. Those, being single chain properties, offer a much better statistical accuracy than the stress itself, which is a global property of the system.

The systems under study are briefly described in the next section. We then discuss the steady state viscosity, both in the linear and nonlinear regime. We use three different methods to determine the viscosity - NEMD simulations, equilibrium Green-Kubo approach and show how the viscosity can be obtained in a third way from the analysis of equilibrium Rouse modes, provided the contribution from short times is correctly taken into account. We then turn to the study of oscillatory strains by means of NEMD simulations. The conditions for linear response at low frequency are discussed, and the various contributions to stress response - storage and loss - are estimated. Again, the results are compared to an equilibrium analysis based on the Rouse model.

## 3.2 System description and methods

The chains are modelled by an abstract and generic, though well studied, bead spring model - the rather common “Lennard-Jones + FENE” model [43]. All monomers in the system are interacting through the Lennard-Jones

potential:

$$U_{lj}(r) = \begin{cases} 4\varepsilon((\sigma/r)^{12} - (\sigma/r)^6), & r \leq r_c \\ 0, & r > r_c \end{cases} \quad (3.1)$$

where  $r_c = 2.5\sigma$ . Neighbor monomers in the same chain are linked by the FENE (Finite extension non-linear elastic) potential:

$$U_{FENE}(r) = -\frac{k}{2}R_0 \ln(1 - (\frac{r}{R_0})^2) + 4\varepsilon((\sigma/r)^{12} - (\sigma/r)^6) + \varepsilon \quad (3.2)$$

where  $R_0 = 1.5\sigma$  and  $k = 30.0\varepsilon/\sigma^2$ . The first term is attractive, the second Lennard-Jones term is repulsive. The first term extends to  $r < R_0$ , the maximum extent of the bond. The second is cut off at  $\sqrt[6]{2}\sigma$ , the minimum of the LJ potential. The temperature of the melt was fixed in all simulations at  $k_B T = \varepsilon$ , well above the glass transition temperature for our model ( $k_B T_g \sim 0.42\varepsilon$ ). With these parameters and for the temperature of our system the bonds have a very narrow distribution around the mean value ( $0.965 \pm 0.013\sigma$ ). The time step in the simulation runs was set to  $0.005\tau$ . All results are presented in conventional Lennard-Jones (LJ) reduced units: length scale -  $\sigma$ , energy scale -  $\varepsilon$ , mass - monomer mass  $m$ . All other units can be deduced: time - reduced LJ  $\tau = \sqrt{\frac{m\sigma^2}{\varepsilon}}$ , velocity -  $\sigma/\tau$ , force -  $\sigma/\tau^2$ , reduced temperature, pressure, etc.

As we are interested in the bulk properties of the material the choice of the non equilibrium simulation method to be used is very important. Two methods are possible to impose a shear flow in the system. One can simulate a confined slice of material between two walls and impose a given velocity or force on the walls thus shearing the particles in between. In order to assess bulk properties in this kind of system the measurements should be restricted to the inmost region so that altered interfacial properties do not affect the results. In the case of polymer melts (as discussed thoroughly in chapter 4) we know that the size of this region is of the order of the polymer bulk radius of gyration and could possibly vary in a non trivial manner as a function of the stresses on the wall. In order to obtain bulk properties from a simulation of a confined system, taking a large system is important so that bulk behavior can be measured and this typically leads to a large computational cost. The second solution are the so called Lees Edwards periodic boundary conditions [44]. These allow the simulation of an unconfined periodic system under shear, achieved through a modification of the periodic boundaries (sliding bricks, fig 3.1). The sole application of the modified boundary conditions is referred to as boundary driven algorithm. As the particles move under Newton's equations of motion they feel the inter atomic forces exerted by the particles within the unit cell and by the image particles whose positions are determined by the instantaneous lattice vectors of the periodic array of cells. The motion of the image cells defines the shear rate,  $\dot{\gamma} = \frac{\partial v_x}{\partial y}$ , for the flow. The motion of the cell images is such that their individual origins move

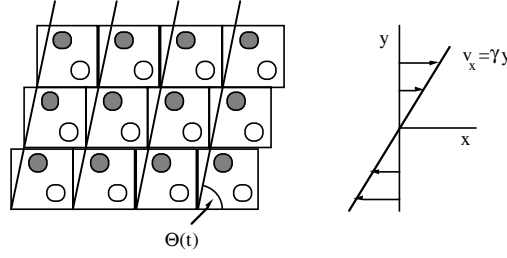


Figure 3.1: The modified boundary conditions following the Lees Edwards scheme

with an x-velocity which is proportional to the y-coordinate of the particular cell origin. If the Reynolds number is sufficiently small and turbulence does not occur, we expect that the motion of image particles above and below any given cell will, in time, induce a linear streaming velocity  $v_x = \dot{\gamma}y$ , on each of the particles within the cell. If a particle  $i$  moves out the bottom of the simulation cube, it is replaced by the image particle with coordinates:

$$\vec{r}_{i,new} = (\vec{r}_i + \vec{e}_x \dot{\gamma} L t)_{mod L} \quad (3.3)$$

or if  $i$  moves out of the top of the simulation cube, it is replaced by

$$\vec{r}_{i,new} = (\vec{r}_i - \vec{e}_x \dot{\gamma} L t)_{mod L} \quad (3.4)$$

where  $L$  is the box size.

There is a major difficulty with the boundary driven algorithm. The way in which the boundaries induce a shearing motion to the particles takes time to occur, approximately given by the sound propagation time across the primitive cell. This is the minimum time taken for the particles to realise that the shear is taking place, and the shear profile is fully established after the momentum has diffused in the cell. The boundary driven method as described above, therefore cannot be used to study time dependent flows. The most elegant solution to this problem introduces the SLLOD algorithm [44]. The equations of motion to be integrated for the motion of the particles are:

$$\frac{d\vec{r}_i}{dt} = \frac{\vec{p}_i}{m} + \vec{e}_x \dot{\gamma} y_i \quad (3.5)$$

$$\frac{d\vec{p}_i}{dt} = \vec{F}_i - \vec{e}_x \dot{\gamma} p_{yi} \quad (3.6)$$

The above equations are equivalent to:

$$m \frac{d^2 \vec{r}_i}{dt^2} = \vec{F}_i + \vec{e}_x m \frac{d\dot{\gamma}}{dt} y_i \quad (3.7)$$

For example if the shear rate is a step function its derivative in the equation above is a delta function  $d\dot{\gamma}/dt = \dot{\gamma}\delta(t)$  and the  $t = 0$  velocities are

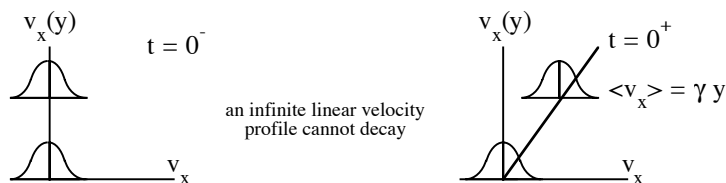


Figure 3.2: The SLLOD equations of motion give an exact representation of planar Couette flow

incremented with respect to the flow (fig. 3.2). We note that the SLLOD equations of motion should be implemented with the Lees Edwards boundary conditions. Compared to the boundary driven methods, the advantages of using the SLLOD algorithm in computer simulations are many. Under periodic boundaries the SLLOD momenta are continuous functions of time and space. For simulations of viscoelasticity special measures have to be taken in the boundary driven algorithm to ensure that the time varying strain rate is actually what you expect it to be. In the SLLOD method no special techniques are required for simulations of time dependent flows. One simply has to solve the equations of motion with a time dependent strain rate and ensure that the periodic boundary conditions are precisely consistent with the strain derived by integrating the imposed shear rate. The imposed shear causes a major change in the microscopic fluid structure. This is manifest in all the thermodynamic properties of the system changing with shear rate.

The NEMD simulations were performed with a modified version of the LAMMPS code [24]. In practice the implementation of the Lees Edwards boundaries in a parallel code using spatial decomposition of the simulation box between processors is not an easy task. Special care should be taken when establishing the communication lists as they become time and shear rate dependent. Parallel efficiency is considerably reduced due to increased communication time. Still the simulations are considerably faster than those of systems with walls as the total number of particles is much lower as the system remains periodic in all three dimensions and there are no interfacial effects.

The typical size of the studied systems in this chapter was of 1280 and 2560 particles (for chain lengths of 10 and 20) in a cubic simulation box periodic in all three dimensions. The temperature of the melt was fixed in all simulations at  $k_B T = 1$  and the density was  $\rho = 0.85$ . A straightforward application of a thermostat should be avoided in NEMD. The thermostat should be applied to the thermal velocity field, which is the actual velocities of the particles minus the imposed shear velocity field. In practice one does not have to couple a thermostat to all the velocity components, as different directions are coupled to each other. In our case the velocity component in

the direction of the shear flow  $v_x$  is left unchanged and the other components are rescaled.

### 3.3 Viscosity determination by NEMD

The most direct method to obtain shear viscosities is undoubtedly the non equilibrium approach that generates homogeneous, planar Couette flow using Lees-Edwards boundary conditions and the SLLOD algorithm, imposing a constant shear rate. For a shear rate  $\dot{\gamma}$  and a velocity profile  $v_x(y) = \dot{\gamma}y$ , the viscosity is given by

$$\eta = \frac{\langle \sigma(t) \rangle}{\dot{\gamma}} \quad (3.8)$$

Where  $\sigma(t)$  is the  $xy$  component of the stress tensor in the sample. The stress tensor in the melt is calculated as  $\sigma_{\alpha\beta}(t) = -\frac{1}{V} \sum r_{ij}^\alpha F_{ij}^\beta$ , where  $F_{ij}^\beta$  the  $\beta$  component of the force between particles  $i$  and  $j$ . The kinetic contribution of the stress ( $\propto \sum v_i^\alpha v_i^\beta$ ) was also evaluated and found to have a negligible contribution to the stress. As discussed in section 2.3, this result is expected at high density and for the shear rates that we simulate as there is no convection in our system. The viscosity obtained by this method depends on the shear rate, generally decreasing with  $\dot{\gamma}$ . This behavior, known as shear thinning is typical for complex fluids and has been observed for polymer melts in a number of studies [44, 45]. An extrapolation is required to estimate the zero shear rate value. Shear thinning generally takes place when  $\dot{\gamma} > 1/\tau_c$ , where  $\tau_c$  is a characteristic relaxation time of the polymer melt (usually, for unentangled melts, the Rouse time  $\tau_R$ , as can be seen in fig. 3.3).

Precise measurements for low shear rates are very time consuming as substantial statistics are needed for the accurate determination of  $\langle \sigma(t) \rangle$  which has a small value for small shear rates. An accurate estimation of the error bars in this kind of study is of essence in order to evaluate the potential utility of the presented method. If we neglect all systematic error sources such as finite size effects or possible deviations of the algorithm from physical reality we have to precisely estimate the statistical accuracy of the data. A method providing the statistical error value without any assumption of the nature of the physical system is the block averaging. Let's suppose we measure a quantity  $A$ . We define

$$A_n = \frac{1}{n} \sum_{i=0}^n A_i \quad (3.9)$$

as the mean value over  $n$  measurements. Assuming that the true value of the quantity, i.e. the expectation value with respect to the exact but unknown probability distribution is  $a$ , what we measure in reality is  $A_i = a + \delta_i$ . If

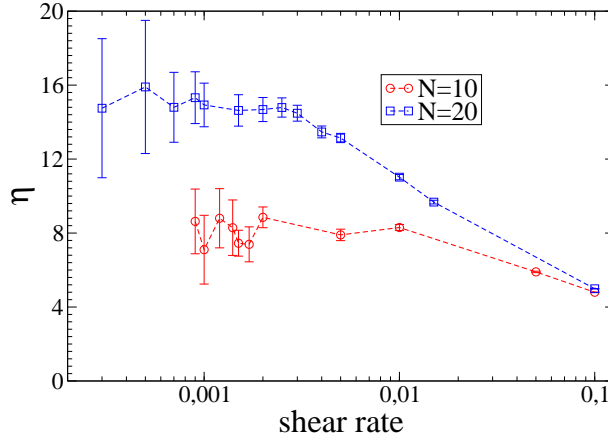


Figure 3.3: Shear viscosity as a function of shear rate  $\dot{\gamma}$  measured in simulations of planar flow (equation 3.8). Shear thinning takes place for approximately  $\dot{\gamma} > 0.01$  for  $N = 10$  and  $\dot{\gamma} > 0.0025$  for  $N = 20$ . The estimated Rouse relaxation times for the two chain lengths are respectively about 100 and 400. Stress was measured every  $2\tau_{LJ}$  for a time ranging from  $15000\tau_{LJ}$  for high shear rates to  $55000\tau_{LJ}$  for low shear rates. Error bars are estimated using block averages for data correlation.[46]

our estimations are unbiased the mean value of the random variable  $\delta_i$  is 0. If every measurement was statistically independent from any other the standard error ( $\delta$ ) of the true value would be related to the measured values as

$$\delta_n^2 = \frac{1}{n}\delta^2 \quad (3.10)$$

Assuming there is some correlation between the measurements typically spanning over  $k_c$  measurements

$$\langle \delta_i \delta_j \rangle = f(|i - j|) = \exp(-|i - j|/k_c) \quad (3.11)$$

the equation 3.10 is changed to

$$\delta_n^2 = \frac{1}{n}\delta^2 \sum_{k=0}^n f(k) \approx \frac{1}{n}\delta^2 k_c \quad (3.12)$$

If we have  $n_{tot}$  measurements we divide the data into  $n_b$  blocks each of length  $n$ . We calculate the block averages  $A_1, \dots, A_{n_b}$  and the variance:

$$\delta_n^2 = \frac{1}{n_b} \sum_{i=0}^{n_b} (A_i - \langle A \rangle_{run})^2 \quad (3.13)$$

where  $\langle A \rangle_{run}$  is the global mean value calculated from all data points. Given that  $n$  is large enough the so calculated variance is related to the error of the

real distribution and the data correlation via equation 3.12. In practice we repeat this procedure several times for different values of the block length  $n$  and then plot  $\delta_n^2$  versus  $1/n$  (see fig. 3.4). The estimated slope from this plot indicates the “real” variance  $\delta^2 k_c$  we are looking for and the error bar for the measured value of the stress is then  $(\delta^2 k_c / T_{run})^{1/2}$ . More detailed discussion about the error estimation can be found mostly in [47] as well as in [46] and [48].

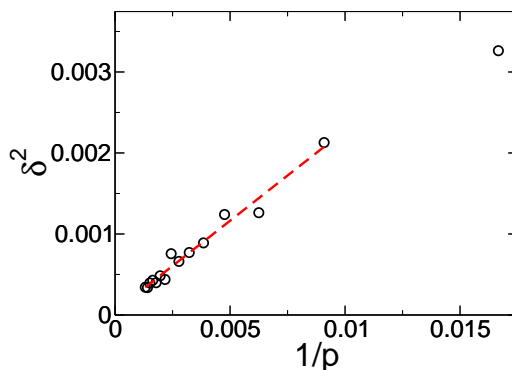


Figure 3.4: Variance estimated from the data (equation 3.13) as a function of the inverse block length. The fit slope gives the statistical variance and correlation and is used to calculate error bars of the mean stress value (here for  $N = 10$  and  $\dot{\gamma} = 0.07$ )

The greatest shortcoming of the NEMD measurement comes from the fact that as the relaxation time of the polymer chains increases rapidly with the chain length ( $\tau_c \propto N^2$  and  $\propto N^3$  in the entangled regime), for long chains very low shear rates  $\dot{\gamma} < 1/\tau_c$ , should be used to reach the Newtonian plateau in  $\eta(\dot{\gamma})$ . The low shear rates yield a low value of the stress whereas the fluctuations remain large. Furthermore the mean stress is divided by the small shear rate to obtain the viscosity so the uncertainty is increased. This is illustrated by the large error bars on the low shear rate side of figure 3.3. We note that by using the Lees-Edwards/SLLOD method we do not have any error on the shear rate value as it is imposed via the equations of motion and the boundary conditions. If we were shearing the melt with external walls the shear rate would be obtained from the velocity profile and would be therefore prone to some error itself. This can be stated as another advantage of the SLLOD method. For chains of lengths  $N = 10$  and  $N = 20$ , our extrapolation at zero shear rate is consistent with the scaling expected for unentangled melts,  $\eta \propto N$ , and with earlier estimates found in the literature [42].

### 3.3.1 Green-Kubo approach

The problem of extrapolating the shear rate dependent viscosity value does not occur in equilibrium methods. Using linear response theory one can relate the value of the transport coefficients to the equilibrium fluctuations of their associated thermodynamic flux. The resulting formulae are the Green-Kubo relations widely used in computer simulations [44, 46]. The zero shear rate viscosity is thus given by the integral of the stress correlation function

$$G(t) = \frac{V}{k_B T} \langle \sigma_{xy}(t) \sigma_{xy}(0) \rangle \quad (3.14)$$

$$\eta = \int_0^\infty G(t) dt \quad (3.15)$$

with  $T$  and  $V$  the melt temperature and volume. It is well known that obtaining an accurate value for the slowly decaying stress correlation function involves very long runs in order to have sufficient statistics. The results we present here are obtained by calculating the stress correlation over a time series of data covering  $25000\tau$  of the  $N = 10$  system. This simulation time is roughly 250 times the largest relaxation time of the polymer chains of length 10 and is hardly attainable for longer chains. The most natural way of estimating the error in the viscosity from the Green Kubo formula is to compare the three different values obtained from the three different (and independent) off diagonal components of the stress tensor. The results are shown on fig. 3.5. The uncertainty of the Green-Kubo formula concerning viscosity is on the order of 30% when the integral is carried out to several relaxation times and grows much larger as the correlation function is further integrated.

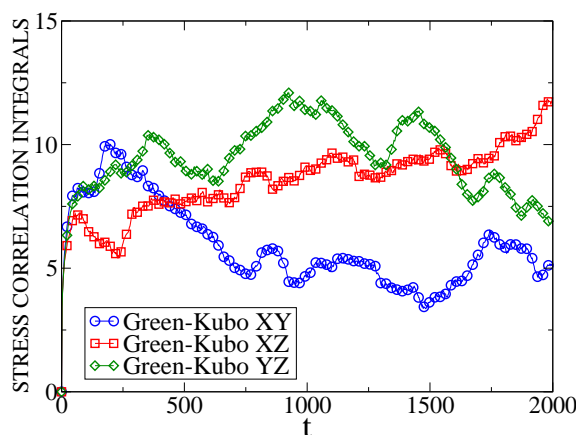


Figure 3.5: Integrals of the stress correlation function  $G(t)$  for  $N = 10$  (equation 3.15). More details for the measurements are given on fig. 3.6.

We know that the correlation function is non zero for times smaller than the largest relaxation time in our system (the Rouse time in our case). To understand the unstable behavior of the integrals and identify the possible error sources a more detailed study of the statistical accuracy of the correlation functions is needed. Such information is also vital in order to evaluate the usefulness of this method in practical situations.

In the following calculation we will omit the prefactor  $V/k_B T$  in the stress correlation as it does not play a role in the error calculation. From a MD run we measure the auto correlation of the stress as:

$$G(t) = \frac{1}{T_{run}} \int_0^{T_{run}} \sigma_{xy}(s+t)\sigma_{xy}(s)ds \quad (3.16)$$

Let's consider the variance in  $G(t)$ :

$$\begin{aligned} \langle G(t)^2 \rangle - \langle G(t) \rangle^2 &= \\ &= \frac{1}{T_{run}^2} \int_0^{T_{run}} \int_0^{T_{run}} \langle \sigma_{xy}(s+t)\sigma_{xy}(s)\sigma_{xy}(u+t)\sigma_{xy}(u) \rangle dsdu \quad (3.17) \\ &- \frac{1}{T_{run}^2} \int_0^{T_{run}} \int_0^{T_{run}} \langle \sigma_{xy}(s+t)\sigma_{xy}(s) \rangle \langle \sigma_{xy}(u+t)\sigma_{xy}(u) \rangle dsdu \end{aligned}$$

This rather complicated expression can be simplified if we assume that the fluctuations of the stress follow Gaussian statistics. For Gaussian variables we can factorize all high order correlation functions and in particular:

$$\begin{aligned} \langle \sigma_{xy}(s+t)\sigma_{xy}(s)\sigma_{xy}(u+t)\sigma_{xy}(u) \rangle &= \\ &= \langle \sigma_{xy}(s+t)\sigma_{xy}(s) \rangle \langle \sigma_{xy}(u+t)\sigma_{xy}(u) \rangle \quad (3.18) \\ &+ \langle \sigma_{xy}(s)\sigma_{xy}(u) \rangle \langle \sigma_{xy}(u+t)\sigma_{xy}(s+t) \rangle \\ &+ \langle \sigma_{xy}(s+t)\sigma_{xy}(u) \rangle \langle \sigma_{xy}(u+t)\sigma_{xy}(s) \rangle \end{aligned}$$

inserting this into equation 3.17 and simplifying we obtain:

$$\begin{aligned} \langle G(t)^2 \rangle - \langle G(t) \rangle^2 &= \\ &= \frac{1}{T_{run}} \int_{-\infty}^{\infty} (\langle \sigma_{xy}(v)\sigma_{xy}(0) \rangle^2 - \langle \sigma_{xy}(v-t)\sigma_{xy}(0) \rangle \langle \sigma_{xy}(v+t)\sigma_{xy}(0) \rangle) dv \quad (3.19) \end{aligned}$$

where we consider the simulation time much longer than the characteristic decay time of the stress and we have defined  $v = s - u$ . Let us define a typical correlation time of the data as:

$$\tau_c = 2 \int_0^{\infty} \frac{\langle \sigma_{xy}(v)\sigma_{xy}(0) \rangle^2}{\langle \sigma_{xy}(0)^2 \rangle^2} dv \quad (3.20)$$

We note that if our correlation is a simple exponential the definition above gives the decay time of the exponential. Now we can easily estimate the variance of the stress correlation in the two limiting cases of short times and long times. For  $t \rightarrow 0$  we have:

$$\langle G(t)^2 \rangle - \langle G(t) \rangle^2 = 4G(0)^2 \frac{\tau_c}{T_{run}} \quad (3.21)$$

For  $t \rightarrow \infty$  the second term in the integral in equation 3.19 vanishes and we have:

$$\langle G(t)^2 \rangle - \langle G(t) \rangle^2 = 2G(0)^2 \frac{\tau_c}{T_{run}} \quad (3.22)$$

and the standard absolute error in the correlation function is given by the square root of the variance above. It should be stressed that the preceding estimate is only approximative, relying on the validity of the Gaussian approximation. It is also very general and does not take into account the specific physical nature of the stress correlation function in a polymer melt. Additional details about this type of calculation are given in ref. [49]. Comparing the  $t \rightarrow \infty$  and  $t \rightarrow 0$  behavior we see that the absolute error in  $G(t)$  changes very little with the time  $t$ . As a consequence, the relative error increases rapidly as  $G(t)$  goes to zero. Furthermore, this derivation assumes that the total number of samples for each  $t$  is equal, so strictly speaking if we have fewer samples for large  $t$  this approach is not valid. In practice this is the case for nearly any correlation function so this calculation should underestimate error for long times. Estimating the statistical correlation time from the correlation function (equation 3.20) we find  $\tau_c \sim 0.05$ . The problem with the stress auto correlation is that it has a high initial value and drops rather quickly to a small plateau, we have  $\langle \sigma^2 \rangle \approx 10^3 \langle \sigma(10)\sigma(0) \rangle$  (this can be seen on fig. 3.8). This means that in order to obtain a relative precision of  $\sim 10\%$  for  $\langle \sigma(10)\sigma(0) \rangle$  it would be necessary to run a simulation of  $\sim 10^7$  (units of LJ time). Hence the stress correlation function in the polymeric case is long ranged in time and has a low amplitude, easily masked by noise associated with the rapid pair and bond-potential part of the stress that does not involve polymer chain relaxation. This estimate is indeed very pessimistic and should be seen as an upper bound of the possible error in the Green Kubo formula. In practice a partial solution can be to average out the oscillations in the stress correlation due to bond vibrations and short time relaxation. This has been done by performing sliding averages in ref. [50]. The procedure affects only slightly the viscosity in the case of long chains but can alter its value for shorter chains where short time relaxation is important as we will discuss later in the present chapter. In this case the observed error on viscosity (at least at intermediate times) is lower than the straightforward statistical prediction but still consistent with the picture on fig. 3.5. An issue worth discussing is the fact that the correlation time estimated via equation 3.20 is rather small compared to the physical times involved in the system, being of the same order of magnitude as the period of the bond vibrations in the chains (fig. 3.8). On one hand this indicates that the largest error source tends to be the bond high frequency vibrations and justifies to a certain extent the averaging procedure. In practice the stress auto correlation function has several contributions with different weights and correlation times. If  $G(t)$  has a structure of the form  $\sum_i A_i \exp(-t/\tau_i)$  exhibiting a series of relaxation times, a calculation using 3.20 produces a correlation time

in which each  $\tau_i$  have a weighing factor  $\sim A_i^2$ . For more precise estimation knowledge of the values of the prefactors would be required. The error value should in reality be chain length dependent. For longer chains the largest correlation times as well as their prefactors are expected to increase as the long time stress relaxation's contribution to the viscosity grows rapidly with chain length, as well as the chain relaxation times. A complete picture of the uncertainties in those cases requires additional measurements and stands outside of the goals of the present study. The best way to estimate uncertainty in this case seems to remain the comparison of the viscosity value from the three independent components of the stress correlation (fig. 3.5).

We did not examine the influence of system size on the statistical accuracy of our data. If a larger system should diminish stress fluctuations (by a factor  $\propto \sqrt{N}$ , where  $N$  is the number of particles), a similar effect is expected by longer simulation time (a factor  $\propto \sqrt{T}$ ). As the computational effort for larger system increases roughly as  $N \log N$ , we do not expect to gain better precision for less computational time this way, so we did not examine the trade off between system size and run time.

We are aware of several determinations of polymer melt viscosity using the Green-Kubo approach. In [51] a good agreement with NEMD results was obtained for short simulation times without discussion on uncertainty. Another calculation was made in [50], where the authors reported the existence of a large noise in the correlation function. This problem was solved, as mentioned above, by performing running averages to smooth the data, a method that can reduce the noise due to rapid bond vibrations but whose effect on the intrinsic statistical accuracy of the stress correlation is not obvious. Our data still indicate a large error bar (30%), when this error bar is estimated from the three independent components of the stress tensor. A similar result is also reached when using this estimation in other systems [52]. A viscosity determination based on a Green-Kubo formula in terms of an Einstein relation was presented in [53], unfortunately with relatively little details that would allow us to compare with our results in terms of efficiency and accuracy. It is clear that the Green-Kubo formula remains the only exact way of determining the viscosity from equilibrium simulations, and should be used whenever an "exact" result is required. Although this is feasible with a large computational effort [53], a detailed report on its accuracy for polymers is still missing (see however [52]). Therefore it seems interesting to discuss an alternative, faster, approach that can be used for example in comparative studies at a moderate computational cost.

### 3.3.2 Rouse modes

It is well known that, at least at a qualitative level, the Rouse model can account for the viscoelastic behavior of unentangled polymer melts. Hence, it is tempting to attempt to bypass the difficulty in obtaining the viscoelastic

properties stricto-sensu by directly using this model. A major motivation for this is that the large uncertainties discussed above are highly reduced, when we turn to the calculation of single-particle (or single-chain) correlation functions, which are the essential ingredient of the Rouse model. As the final result is an average over  $M$  separate functions the standard error at long times (equation 3.22) is in this case be  $(2G(0)^2\tau_c/(M \times T_{run}))^{1/2}$ . This is the reason why single particle correlation functions (such as the velocity auto correlation) are relatively easily measured in computer simulations.

The spirit of the Rouse model consists in assuming that the melt mechanical behavior is dictated by the relaxation of a single polymer chain, the influence of inter chain interactions being limited to the phenomenological friction constant (section 2.3). Consistent with this assumption, the mechanical stress can be calculated from the Rouse modes of the chains [31] as described in section 2.3

$$\sigma_{xy}(t) = \frac{\rho k_B T}{N} \sum_{p=1}^{N-1} \frac{\langle X_{px}(t) X_{py}(t) \rangle}{\langle X_{px}^2 \rangle_{eq}} \quad (3.23)$$

where  $X_p(t)$  are the Rouse modes given by equation 2.16. Assuming, again in the spirit of the Rouse model, independent Rouse modes, the stress correlation from equation (3.14) can be rewritten as a function of the equilibrium correlation functions for individual Rouse modes at equilibrium:

$$\begin{aligned} G(t) &= \frac{V}{k_B T} \langle \sigma_{xy}(t) \sigma_{xy}(0) \rangle \\ &= \frac{V}{k_B T} \frac{1}{T^{sim}} \int_0^{T^{sim}} d\tau \left( \frac{\rho k_B T}{N} \right)^2 \sum_{p,q} \frac{\langle X_{px}(t+\tau) X_{py}(t+\tau) \rangle}{\langle X_{px}^2 \rangle} \frac{\langle X_{qx}(\tau) X_{qy}(\tau) \rangle}{\langle X_{qx}^2 \rangle} \\ &= \frac{V}{k_B T} \frac{1}{T^{sim}} \int_0^{T^{sim}} d\tau \left( \frac{\rho k_B T}{N} \right)^2 \frac{1}{N_c^2} \sum_{c,c'} \sum_{p,q} \frac{X_{px}^c(t+\tau) X_{py}^c(t+\tau)}{\langle X_{px}^2 \rangle} \frac{X_{qx}^{c'}(\tau) X_{qy}^{c'}(\tau)}{\langle X_{qx}^2 \rangle} \\ &= \frac{1}{T^{sim}} \int_0^{T^{sim}} d\tau \frac{\rho k_B T}{N} \frac{1}{N_c} \sum_{c=1}^{N_c} \sum_{p=1}^{N-1} \frac{X_{px}^c(t+\tau) X_{py}^c(t+\tau) X_{px}^c(\tau) X_{py}^c(\tau)}{\langle X_{px}^2 \rangle} \\ &= \frac{\rho k_B T}{N} \sum_{p=1}^{N-1} \frac{\langle X_{px}(t) X_{py}(t) X_{px}(0) X_{py}(0) \rangle}{\langle X_{px}^2 \rangle^2} \end{aligned} \quad (3.24)$$

The viscosity is then calculated using equation (3.15). With this method we observe a substantial gain in precision (see figure 3.6) using as criterion the viscosity determination via the three off diagonal stress components. This better accuracy is achieved for a shorter simulation time. The values obtained are smaller than the non equilibrium estimates, by about the same amount for the two different chain lengths ( $\eta_{NEMD} - \eta_{eq} \sim 5$  [LJ units]).

This result is not surprising given the simplifications of the latter calculation. The interactions between chains in the melt are not taken into account and the Rouse model cannot yield information about stress relaxation on very short “non - polymer” time scales. In order to get a better

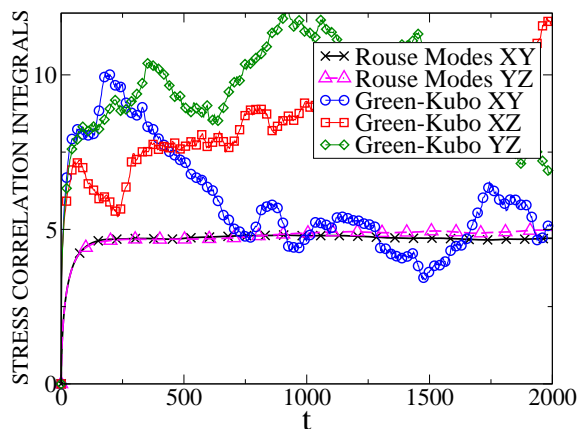


Figure 3.6: Integrals of the stress correlation function  $G(t)$  for  $N = 10$  obtained from the global stress (Green-Kubo) and the Rouse modes stress. A distinct plateau that stays stable for very long times ( $\sim 50\tau_R$ ) is clearly reached with the Rouse modes formulation. For comparison the Green-Kubo integral value has important fluctuations for times longer than several times the Rouse relaxation time  $\tau_R$  as predicted by the uncertainty calculation. Global stress was measured every  $0.01\tau_{LJ}$  for a time span of  $25000\tau_{LJ}$  and  $G(t)$  was calculated by taking every point as a starting state and averaging. Such fine sampling is needed to capture the fast oscillations in  $G(t)$  shown in fig. 3.8. Rouse modes were measured every  $0.5\tau_{LJ}$  for every chain for a time of  $15000\tau_{LJ}$ . Then  $G^{Rouse}(t)$  was calculated averaging over starting states and chains.

understanding of the deficiencies in the calculation using the Rouse model, we first compute the individual relaxation times of the modes. The relaxation times, shown in figure 3.7, are extracted from the exponential decay of these correlation functions. The Rouse scaling  $\tau_p \propto 1/p^2$  is well obeyed for the first modes.[26] While this is a typical result for the bead-spring model [26], we note that using more detailed atomistic simulations larger deviations from the Rouse scaling can be observed, especially in higher modes [54]. For both chain lengths, the relaxation time of the fastest mode was found to be  $\tau_{N-1} \sim 2$ .

It is clear that the Rouse calculation cannot account for the contribution to the viscosity associated with time scales shorter than  $\tau_{N-1}$ . On such short time scales the Green-Kubo viscosity integrand can however be obtained with high accuracy, as illustrated in 3.8. As statistics decrease linearly with time when we perform averaging over initial states, for short times  $G(t)$  has higher precision. This stress-stress correlation function first decreases rapidly, and displays a short time damped oscillatory behavior, with a time constant

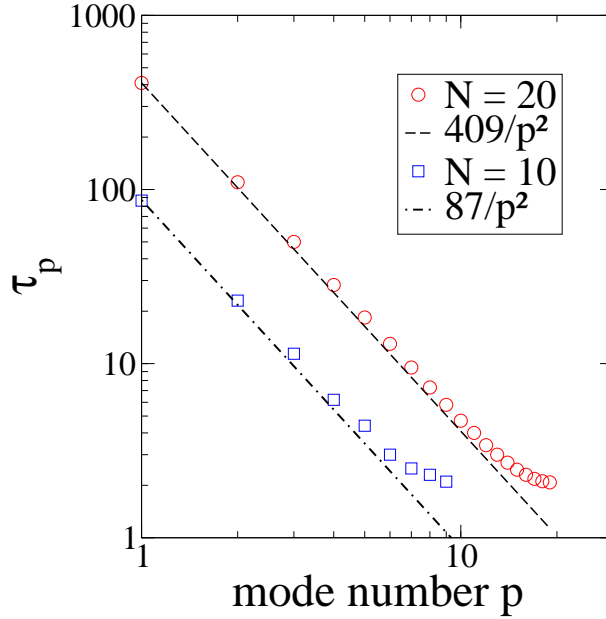


Figure 3.7: Relaxation times of the Rouse modes of the chains versus the mode number. Relaxation times were estimated by an exponential fit of the normalized correlation function of the mode, which had in all cases an exponential behavior. Dashed lines show the Rouse theory prediction  $\tau_p \propto 1/p^2$ , followed closely by the first several modes as discussed in [26].

smaller than 0.5. Similar stress oscillations were reported for n-alkanes as well as for a bead-spring melt [53, 50]. In our case, a detailed study of the FENE bonds and Lennard-Jones forces contributions to the stress, shows that these oscillations are due bond vibrations, and that their frequency is close to the intrinsic frequency of the FENE bonds.

Integrating this short time stress correlation function gives the contribution to the melt viscosity of the rapidly decaying part of the global stress, unaccounted for in the Rouse model.

$$\eta = \int_0^{\infty} G(t) dt \quad (3.25)$$

$$= \int_0^{\infty} G^{Rouse}(t) dt + \int_0^{\tau_{N-1}} \frac{V}{k_B T} \langle \sigma_{\alpha\beta}(t) \sigma_{\alpha\beta}(0) \rangle dt \quad (3.26)$$

Adding the contribution of the second term of equation 3.26 to the viscosity from the Rouse model provides a significantly more accurate estimate of the viscosity, compared to that calculated from non equilibrium runs (table 3.1). The short time behavior of the stress correlation function is the same for chain lengths  $N = 10$  and  $N = 20$ , which is an evidence that this short times contribution is independent of chain length and represents the

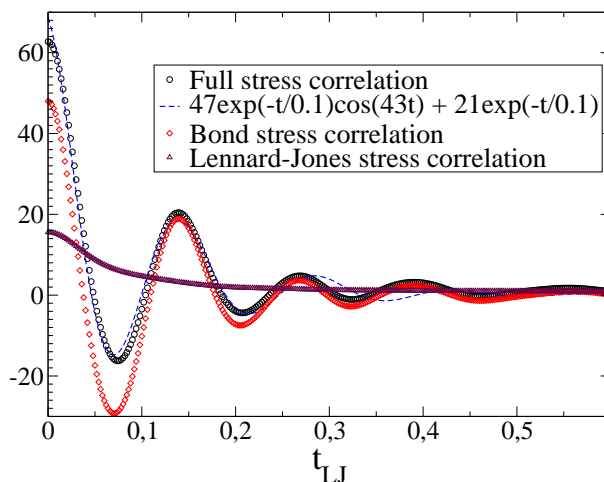


Figure 3.8: Global stress correlation functions for short times. Correlations of the pair Lennard-Jones and FENE bond interactions contribution to the global stress are also shown. Dashed line shows a fit of the global stress correlation to indicate the relevant decay time scales and oscillation frequency.

missing “non-polymeric” part of the mechanical properties of the melt. In fact it provides a contribution to viscosity on the order of the viscosity of a simple LJ fluid at the considered density and temperature [40].

Viscosity	$N = 10$	$N = 20$
Green-Kubo estimate	$8 \pm 4$	N/A
Rouse modes value	$4.88 \pm 0.28$	$10.2 \pm 1.0$
Short times correction	3.38	3.43
NEMD extrapolation	$8.2 \pm 1.3$	$14.9 \pm 1.9$
Corrected Rouse value	$8.26 \pm 0.28$	$13.6 \pm 1.0$

Table 3.1: Viscosity values from the different methods. Uncertainties in Green-Kubo and Rouse modes  $G(t)$  integrals are estimated by evaluating the  $\langle \sigma_{xy}(t)\sigma_{xy}(0) \rangle$ ,  $\langle \sigma_{xz}(t)\sigma_{xz}(0) \rangle$  and  $\langle \sigma_{yz}(t)\sigma_{yz}(0) \rangle$  integrals.

Being chain length independent, short times stress relaxation represents a part in viscosity that diminishes with increasing chain length, about 40% for  $N = 10$  and  $\sim 30\%$  for  $N = 20$ . Still it cannot be neglected for predicting mechanical properties of a melt of unentangled chains. It is equally important for long chains at large shear rates, when the melt viscosity becomes comparable to the one of a simple fluid and can explain deviations from the stress-optic rule [55]. As we shall see in the next chapter, for long chains this contribution can be neglected in equilibrium as it is a minor correction.

The presented method provides a way to rapidly obtain an estimate of

the viscosity as it requires much less computational time than an accurate Green Kubo measurement. It is still less straightforward and one needs to monitor  $N$  (where  $N$  is the chain length) Rouse modes for every chain to build the correlation function. On the other hand as the modes variation is slower than the variation of the global stress, one does not need to store the modes values as frequently as the stress for a Green Kubo calculation. The method's main advantage is that, being based on a single chain quantity, it is local in nature and can be used to assess local viscoelastic properties in inhomogeneous systems such as confined melts or melts with filler particles. The calculation can be applied to a group of chains in a specific region thus studying the typical viscoelastic behavior of the considered area.

## 3.4 Elastic Moduli

### 3.4.1 Method

Like the viscosity, elastic moduli can be obtained using either equilibrium or non equilibrium simulation. If one is interested only in linear response properties, the moduli can be obtained by Fourier transforming the Green-Kubo integrand  $G(t)$  (equation 3.14) in the form

$$G'(\omega) = \omega \int_0^{\infty} dt G(t) \sin \omega t \quad (3.27)$$

$$G''(\omega) = \omega \int_0^{\infty} dt G(t) \cos \omega t \quad (3.28)$$

This equilibrium determination, however, suffers from the same drawbacks as the Green-Kubo determination of the viscosity, i.e. a long time, small amplitude tail of  $G(t)$  has to be known very accurately to obtain reasonable results. That is why we do not show any result concerning elastic moduli issued by a Green-Kubo method. Instead, the only practical way of using equations 3.27 and 3.28 is to start from a "model" calculation of  $G(t)$ , in the sense of the Rouse modeling described in the previous section.

To obtain information beyond the linear regime, the only possibility is to effectively do NEMD and submit the sample to an oscillatory strain, using the standard SLLOD algorithm discussed above. The strain is given by

$$\dot{\gamma}_0(t) = \gamma_0 \omega \sin \omega t \Rightarrow \gamma_0(t) = -\gamma_0 \cos \omega t \quad (3.29)$$

And we define the response of the system by the usual formulae for the stress  $\sigma(t)$

$$\sigma(t) = \int_{-\infty}^t G(t-t'; \gamma_0, \omega) \dot{\gamma}_0(t') dt' \quad (3.30)$$

A dependence on the shear amplitude and frequency is indicated in the response function  $G$ , to recall the possible existence of nonlinear effects.

The frequency dependent moduli are defined from the Fourier component of  $\sigma(t)$  at the imposed frequency  $\omega$

$$\sigma(t) = \gamma_0(G'(\omega, \gamma_0) \sin \omega t + G''(\omega, \gamma_0) \cos \omega t) + \text{harmonics at } 2\omega, 3\omega.. \quad (3.31)$$

The moduli are formally given by the Fourier transforms of the response function

$$G'(\omega; \gamma_0) = \omega \int_0^\infty dt G(t; \gamma_0, \omega) \sin \omega t \quad (3.32)$$

$$G''(\omega; \gamma_0) = \omega \int_0^\infty dt G(t; \gamma_0, \omega) \cos \omega t \quad (3.33)$$

In practice,  $G'$  (resp.  $G''$ ) is extracted from the time series for the stress by multiplying the signal by  $\cos(\omega t)$  (resp.  $\sin(\omega t)$ ), i.e.

$$G'(\omega, \gamma_0) \int_0^{T_r} dt \cos^2 \omega t = -\frac{1}{\gamma_0} \int_0^{T_r} dt \sigma(t) \cos \omega t + G''(\omega) \int_0^{T_r} dt \cos \omega t \sin \omega t \quad (3.34)$$

with  $T_r$  the length of the simulation run. Thus we obtain the storage and loss moduli as a function of stress :

$$G'(\omega, \gamma_0) = \frac{2}{T_r + \frac{\sin 2\omega T_r}{2\omega}} \times \left( -\frac{1}{\gamma_0} \int_0^{T_r} dt \sigma(t) \cos \omega t + G''(\omega; \gamma_0) \frac{\sin^2 \omega T_r}{2\omega} \right) \quad (3.35)$$

$$G''(\omega) = \frac{2}{T_r - \frac{\sin 2\omega T_r}{2\omega}} \times \left( \frac{1}{\gamma_0} \int_0^{T_r} dt \sigma(t) \sin \omega t + G'(\omega; \gamma_0) \frac{\sin^2 \omega T_r}{2\omega} \right) \quad (3.36)$$

In the above formulae potential harmonic terms were ignored for simplicity, their contribution being of order  $1/T_r$ . In the limit  $T_r \gg 1/\omega$  one has simply

$$G'(\omega; \gamma_0) = -\frac{2}{T_r \gamma_0} \int_0^T dt \sigma(t) \cos \omega t \quad (3.37)$$

$$G''(\omega; \gamma_0) = \frac{2}{T_r \gamma_0} \int_0^T dt \sigma(t) \sin \omega t \quad (3.38)$$

In order to elucidate the role of the different interactions for the elastic moduli we focus on their respective contribution. The stress can very generally be separated into an intramolecular stress component associated with FENE bonds and intra chain Lennard-Jones forces, and a intermolecular stress component associated with inter-chain Lennard-Jones interactions. In the following the moduli issued from NEMD simulations will be discussed

in terms of these two separate intra and inter molecular contributions. During a NEMD run the full stress in the system as well as its inter and intra molecular components are stored and then elastic moduli are calculated as described above.

### 3.4.2 Results

#### NEMD Results

The first question that we investigated is the extent of the linear regime, in terms of the strain amplitude. Nonlinear effects can in principle be detected by a dependence of  $G(\omega)$  on  $\gamma_0$ , or by the presence of higher harmonics in the stress signal.

There is a clear softening of the response at frequency  $\omega$  as amplitude is increased. This softening is obtained above a value of the strain rate  $\gamma_0\omega$  on the order of  $1/\tau_R$  at low frequencies, as illustrated in figure 3.9. The situation is very similar to the shear thinning behavior of the viscosity, namely the relevant parameter is the shear rate rather than the strain amplitude or frequency.

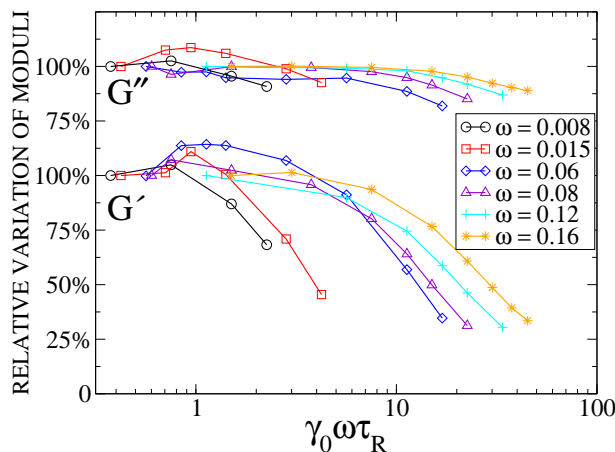


Figure 3.9: Dependence of elastic moduli on strain rate amplitude  $\gamma_0\omega$  for  $N = 10$ . Elastic moduli are normalized by their lowest shear rate amplitude value. For all frequencies the linear regime extends at least to  $\gamma_0\omega \approx 1/\tau_R$ , for  $\omega \gg 1/\tau_R$  the linear behavior breaks down for  $\gamma_0\omega \propto \omega$ . The same behavior was measured for  $N = 20$  (data not shown)

For frequencies  $\omega \gg 1/\tau_R$ , the softening is observed for values of  $\gamma_0\omega$  significantly larger than  $1/\tau_R$ . The behavior of chains in this frequency range is further discussed below. Harmonics were detected in the time series for  $\sigma(t)$  at high values of the strain amplitude  $\gamma_0 > 2.5$  at a frequency of  $3\omega$ , where  $\omega$  is the solicitation frequency, for all frequencies. For symmetry reasons the stress must be an odd function of the strain, so that the response function  $G$

is an even function of  $\gamma$ . Hence harmonic contributions are observed only for odd multiples of the solicitation frequency. The amplitudes of the harmonic terms in the power spectrum are small, about 8% and 3% of the  $\omega$  peak for respectively  $G'(\omega)$  and  $G''(\omega)$ . In the molecular stress harmonics are more visible with about 17% and 5% for the storage and loss moduli, respectively. We have not been able to distinguish harmonics for strain amplitudes  $\gamma_0$  below 2.5. The observation of harmonics can thus be attributed to physical extension of the chains in which the non linear terms in the interaction potentials become inevitably important. Given this preliminary investigation of the non linear regime, we choose first to explore the linear response and place ourselves at shear rates  $\gamma_0\omega < 1/\tau_R$ .

Figures 3.10 and 3.11 display the frequency dependence of the elastic moduli. As discussed above, the important uncertainty in  $G(t)$  obtained from equilibrium calculations imposes the use of non equilibrium methods.

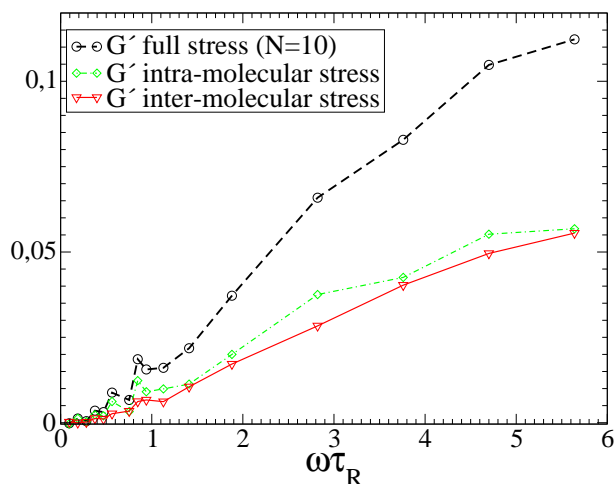


Figure 3.10:  $G'(\omega)$  for  $N = 10$ , measured by NEMD. Contributions from the intra-molecular and inter-molecular forces are shown. Intra molecular forces are important for stress storage up to high frequencies. As  $\omega > 1/\tau_p$ , the modes  $X_i$ ,  $i < p$  are “frozen” and behave like stiff springs and store stress efficiently, so that the intra-molecular component of  $G'(\omega)$  grows with frequency.

The contributions of the different interactions to the elastic moduli (calculated by eqn. (3.37) and (3.38)) can be examined by measuring the different contributions to the global stress. The loss modulus, which is a measure of stress dissipation in the melt has several contributions depending on the time scale (fig. 3.11): at short times stress is relaxed through the pair interactions between monomers, in a “liquid like” manner. At longer times, relaxation of chain fragments of length  $N_p = 1, 2, \dots, N$ , take place on increasingly larger time scales. Knowing that a mode  $p$  can be viewed as

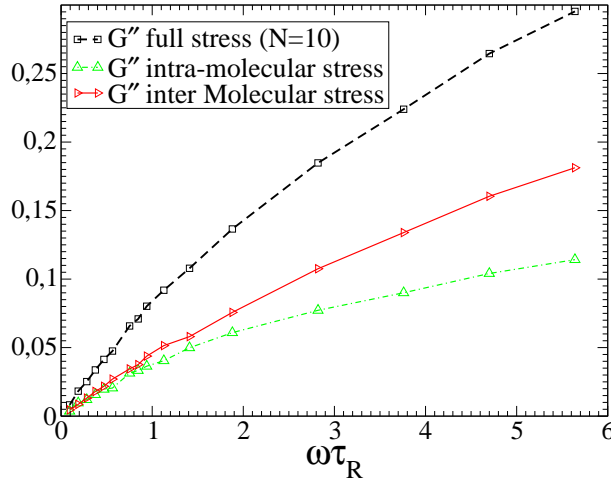


Figure 3.11:  $G''(\omega)$  for  $N = 10$ , measured by NEMD. Contributions to the moduli from the intra-molecular and inter-molecular stress components are also shown. For  $\omega > 1/\tau_R$  the inter-molecular contribution to the loss modulus grows larger than the molecular component and the system crosses over to a liquid-like regime.

the relaxation of a sub chain of  $N_p = N/p$  monomers, for a given mode  $p$  relaxing over  $\tau_p$ , if the frequency is such that  $\omega > 1/\tau_p$ , the mode cannot relax over one oscillation and does not take part in the stress relaxation, meaning that stress is relaxed on scales smaller than  $N/p$  monomers. This leads to the Rouse model prediction that, if chain relaxation was the only process in the melt, the loss modulus had to decrease at high frequencies. This decrease was not observed in our model melt (fig. 3.11), due to non-polymer relaxation. As non-polymer relaxation we refer to the relaxation of stress occurring on a time scale smaller than the relaxation of the fastest Rouse mode and independent of chain length. Results show that at high frequencies the behavior of the loss modulus is dictated by inter molecular interactions, the inter molecular stress component is dominant. There is a crossover from polymer melt behavior where stress dissipation is carried out mainly by chain relaxation to a behavior of a liquid of interacting chains that do not have time to significantly change their conformation over one period. In this regime there is no stress dissipation due to internal polymer chain relaxation and the increase of the loss modulus with frequency is entirely due to Lennard Jones pair interactions on very short time scales. The situation is somewhat different for the storage modulus, where simulations show that internal polymer chain interactions and chain modes are important for the elastic response of the melt up to high frequencies (fig. 3.10). For a simple liquid the value of  $G'(\omega)$  is very small in the considered frequency range, so it is not surprising that its value for the melt is due to the chains. The

stress storage thus takes place to a large extent in the slowly varying chain conformations. Over a large frequency range the slow vibration modes act as an energy reservoir and the higher the frequency, the more the chains remain rigid at the time scale of a single period and thus cause the increase in the storage modulus with frequency. The melt exhibits an elastic behavior due to the chains that grows stronger with frequency, in fact the mechanism exposed for the loss modulus can be applied the other way around for  $G'(\omega)$ . A given mode  $p$  goes rigid as  $\omega > 1/\tau_p$  and thus stores stress (rigid behavior) instead of relaxing it (liquid behavior). As  $\omega > 1/\tau_p$ , the modes  $X_i$ ,  $i < p$  are “frozen” and take an important part in energy storage. For very high frequencies  $\omega > 1/\tau_{N-1}$  the chain behaves more like a spring than a flexible polymer.

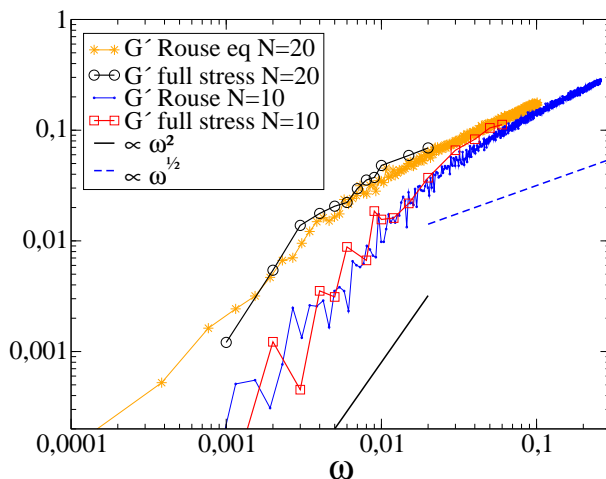


Figure 3.12: Storage modulus from NEMD and equilibrium Rouse modes calculation for chains of length  $N = 10$  and  $N = 20$ . For high frequencies the response of both systems:  $N = 10$  and  $N = 20$ , becomes identical.

### Calculation from Rouse modes and comparison to NEMD data

An analytical calculation of  $G'(\omega)$  and  $G''(\omega)$  can be done using the Rouse model [31, 38]. For the bead-spring polymer melt studied here these functions can be estimated using  $G^{Rouse}(t)$  (eqn. 3.24) via the integrals in equations (3.32) and (3.33). Given that, as discussed above, the stress storage is dictated by slow, “frozen” chain vibration modes for the whole frequency range, the melt elastic response is well reproduced by this calculation (see fig. 3.12). As shown in fig. 3.13, the Rouse approach leads to an underestimate of the loss modulus, especially at high frequencies ( $\omega > 1/\tau_R$ ). The increase in  $G''(\omega)$  for high frequencies is due to short time non-polymeric stress relaxation discussed in the previous section. As discussed in the first

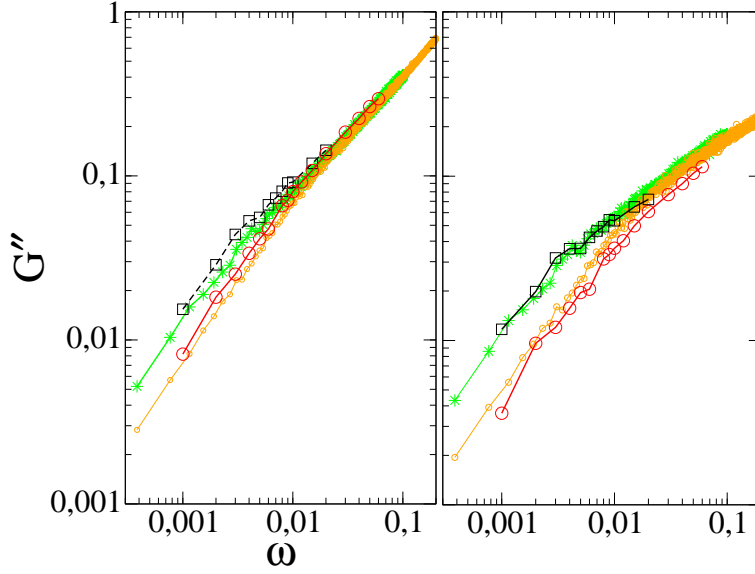


Figure 3.13: Elastic loss modulus from NEMD full stress (left,  $N = 20$  - squares,  $N = 10$  - circles), NEMD intra molecular stress (right,  $N = 20$  - squares,  $N = 10$  - circles), corrected equilibrium Rouse modes calculation (en. 3.42) (left,  $N = 20$  - stars,  $N = 10$  - small circles) and Rouse calculation without short times corrections (right,  $N = 20$  - stars,  $N = 10$  - small circles). The uncorrected Rouse calculation fits well the intra molecular moduli component. Stress relaxation for high frequencies is identical for the two systems, dictated by short sub chain and inter molecular forces relaxation on short time scales as discussed.

part concerning viscosity, this contribution cannot be predicted by  $G^{Rouse}(t)$  that takes into account only chain vibration modes. As no inter molecular forces whatsoever can be taken into account by the single chain Rouse model,  $G^{Rouse}(t)$  provides a good approximation of the loss modulus calculated from the intra molecular stress component and shows a discrepancy with the full stress loss modulus that grows with frequency. In order to obtain an equilibrium single chain estimate of the mechanical behavior of the melt for all frequencies, we estimate the short time corrections to  $G^{Rouse}(t)$  in a manner similar to the one used for viscosity. We use the fit of the short times stress correlation function (fig. 3.8) to calculate the short times correction to the elastic moduli in the frequency domain by equations (3.32) and (3.33). Writing the short time stress correlation in the form

$$G^{fast}(t) = Ae^{-t/\tau_1} \cos \Omega t + Be^{-t/\tau_2} \quad (3.39)$$

leads to

$$G'(\omega) = \omega \int_0^\infty G^{Rouse}(t) \sin \omega t dt \quad (3.40)$$

$$+ \frac{A}{2} \left( \frac{\omega(\omega + \Omega)\tau_1^2}{1 + (\omega + \Omega)^2\tau_1^2} + \frac{\omega(\omega - \Omega)\tau_1^2}{1 + (\omega - \Omega)^2\tau_1^2} \right) + B \frac{\omega^2\tau_2^2}{1 + \omega^2\tau_2^2}$$

$$G''(\omega) = \omega \int_0^\infty G^{Rouse}(t) \cos \omega t dt \quad (3.41)$$

$$+ \frac{\omega\tau_1 A}{2} \left( \frac{1}{1 + (\omega + \Omega)^2\tau_1^2} + \frac{1}{1 + (\omega - \Omega)^2\tau_1^2} \right) + B \frac{\omega\tau_2}{1 + \omega^2\tau_2^2}$$

where we determine the parameters  $A$ ,  $B$ ,  $\Omega$ ,  $\tau_1$  and  $\tau_2$  from the stress correlation function ( $A = 45$ ,  $\Omega = 43$ ,  $\tau_1 = \tau_2 = 0.1$  and  $B = 21$  for both  $N = 10$  and  $N = 20$ ). Adding these terms to the equilibrium Rouse modes loss modulus gives a much better estimate of  $G''(\omega)$ , producing the curves referred to as corrected Rouse (fig. 3.13, corrected Rouse). The correction concerning  $G'(\omega)$  is negligible for the frequency range studied here and the corrected curve falls on top of the original Rouse curve. This is the expected result knowing that, as already mentioned, the liquid like interactions that dominate at short times participate in stress storage only at very high frequencies. We find the expected linear dependence of  $G''(\omega)$  for  $\omega < 1/\tau_R$  (fig. 3.15), the slope being within error bars the value of the viscosity estimated by planar Couette flow simulations. The storage modulus has, as expected,  $\sim \omega^2$  behavior at low frequencies ( $\omega < 1/\tau_R$ ) (fig. 3.14). The Rouse theory predicts a cross over towards a  $\propto \sqrt{\omega}$  behavior for higher frequencies [31]. Our simulations show that  $G'(\omega)$ , estimated by NEMD and Rouse modes measurements, grows slightly faster than  $\sqrt{\omega}$  at high frequencies (fig. 3.14). We can relate this to the discrepancy between theoretical and measured modes relaxation times and argue that the “mean field” presence of multiple chains in our vibration modes determination promotes more efficient stress storage in the melt at high frequencies. Simulations show that  $G''(\omega)$  does not follow the  $\sqrt{\omega}$  behavior at high frequencies either. The loss modulus calculated from the intra molecular stress component, as well as the direct Rouse determination follow closely the square root behavior, but the contribution of “non polymer” short time scale inter chain forces change this behavior to almost completely mask the “polymeric” cross over.

Following the discussion of the linear properties of the melt we can further explore the non linear behavior studied by NEMD, considering the results presented in fig. 3.9. Both the relative decrease in moduli and the harmonics intensity show that the storage modulus has a stronger non linear behavior compared to the loss modulus at a given shear rate. As we have shown that  $G'(\omega)$  has, at all considered frequencies, a large intra molecular contribution, and given that the bond potential is much steeper than the pair potential acting between all monomers, it is reasonable to expect that

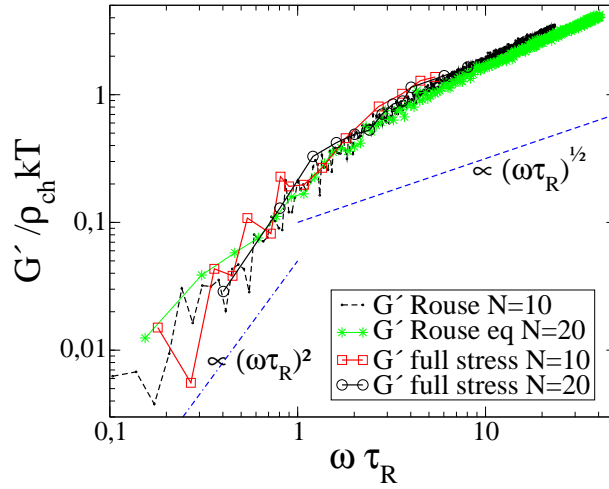


Figure 3.14: Storage modulus divided by the chain density times  $k_B T$  as a function of the reduced frequency  $\omega \tau_R$  for the two systems. A cross over in the behavior is visible for  $\omega = 1/\tau_R$ .

non linear effects due to large deformations would be more pronounced and would appear earlier for the storage modulus. From fig. 3.9 one can see that for  $\omega > 1/\tau_R$ , the higher the frequency, the higher the shear rate determining the onset of non-linear behavior. This critical value of the shear rate was found to vary linearly with frequency  $(\gamma_0 \omega)_c \propto \omega$ . The system starts behaving as viscoelastic, and the linear regime extends to higher shear rates. In fact, as global chain relaxation does not take place on the time scale of the oscillations, there are already “frozen” slow vibration modes in the linear regime at low shear rates. Thus the relevant shear rate for the onset of non-linearity is shifted from  $1/\tau_R = 1/\tau_1$  to  $1/\tau_p$ , where  $p > 1$  is the number of a higher vibration mode that still relaxes on the oscillations time scale at the given frequency.

Finally, we can summarize the overall mechanical behavior of the studied polymer melt exhibiting several distinct regimes as shown in fig. 3.16. At low frequencies  $0 \leq \omega < 1/\tau_R$  and low shear rate amplitudes  $\gamma_0 \omega < 1/\tau_R$  the melt has Newtonian behavior. The viscosity is independent of shear rate and the elastic response is rather small as most of the stress is relaxed by the chain conformations. At low frequencies and high shear rates  $\gamma_0 \omega > 1/\tau_R$  the system is non linear: shear thinning in viscosity, softening in moduli and harmonics in the measured stress. When we shift to high frequencies  $\omega > 1/\tau_R$  the melt exhibits more pronounced viscoelastic behavior with increasing storage modulus due to “frozen” modes and less intra molecular stress relaxation. The non linear boundary becomes frequency dependent and is shifted to higher shear rates determined by the relaxation time scale of chain segments of length  $< N$ . The melt is then expected to exhibit glassy

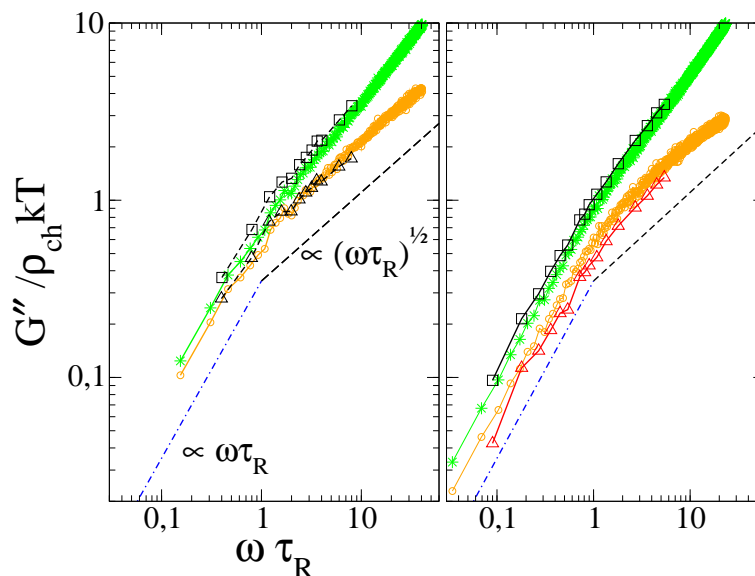


Figure 3.15: Loss modulus divided by the chain density times  $k_B T$  as a function of the reduced frequency  $\omega \tau_R$  for the two systems ( $N = 20$  - left,  $N = 10$  - right). NEMD full stress  $G''$  - squares, NEMD intra molecular stress  $G''$  - triangles, corrected Rouse calculation - stars, Rouse calculation without short times correction - small circles. A crossover in the intra molecular component can be seen for  $\omega = 1/\tau_R$ . “Non polymer” relaxation mask the slope change for the full stress  $G''(\omega)$ .

behavior at very high frequencies when no sub chain relaxation whatsoever can occur within an oscillation.

### 3.5 Discussion and Conclusions

We have discussed the visco-elastic response of a model unentangled polymer melt to external shear strain. We use non equilibrium molecular dynamics methods to directly measure the elastic moduli and the viscosity of the melt. Our aim was also to investigate an equilibrium based method for these quantities, inspired by Green-Kubo relations and possibly offering greater precision. A both statistical and practical study of the uncertainties inherent to the Green Kubo method for measuring viscosity revealed that a precise determination needs a large computational effort. The method we proposed is inspired by the Rouse model, and based on a measurement of the vibration modes of the chains at equilibrium. This single chain quantity can be rather accurately measured from an equilibrium simulation. Following the philosophy of the Rouse model, we use the Rouse modes of the chains to estimate the long times mechanical behavior of the melt and the equilib-

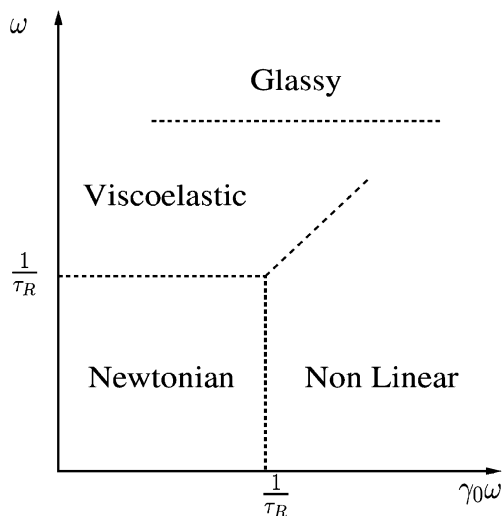


Figure 3.16: Mechanical behavior of the melt for different frequencies and shear rates

rium stress correlation function to estimate small times, independent of chain length non-polymeric behavior. The resulting model provides a satisfactory description of the viscosity and of the elastic moduli of the melt. The part of the different contributions in the mechanical stress played in the viscoelastic melt behavior was also discussed. The NEMD results show that inter chain interactions in the melt add a non negligible background part to the storage modulus and dictate the loss modulus behavior at high frequencies. These interactions should be taken into account for a precise description of the mechanical properties of a polymer melt made of relatively short chains. More generally, these contributions are important for longer chains in several far from equilibrium situations including relaxation. We measured the chain Rouse modes mean square equilibrium values and mode correlations directly from our simulation, so that these quantities already contain, in a “mean field” way, some information about the background environment of the polymer chains. After completing this measurements quantitatively with short times estimate of the stress behavior, the obtained values for the mechanical properties of the melt are accurate, compared to non equilibrium “direct” measurements. The NEMD results show that the storage modulus depends on mode relaxation over a large frequency range, the energy storage takes place in chain conformations whereas for the loss modulus vibration modes are “frozen” one by one as the frequency grows higher than the inverse chain relaxation time and dissipation is dictated by short time scales “non polymer” stress relaxation. A given vibration mode  $p$  relaxing over  $\tau_p$ , interpreted as the relaxation of a sub-chain of length  $N/p$  monomers, can contribute mostly to the loss modulus ( $\omega < 1/\tau_p$ ) or to the storage modulus,

if  $\omega > 1/\tau_p$ . This picture provides an explanation for the overall behavior of the elastic moduli in the studied frequency range. Our results are in quantitative agreement with previous studies, [42] but here we focused on lower frequencies for the elastic moduli, based on the chain relaxation time that we estimated, in order to interpret the microscopic mechanisms involved. Different stress contributions on different time scales were measured from the simulations, thus allowing the determination of mechanical response from equilibrium properties involving Rouse modes measurements and short times corrections.

We examined the onset of non linear effects in the measured quantities, manifested by shear thinning, moduli softening and harmonics in the stress time series. The non linear regime is dictated by the shear rate of the solicitation and takes place at  $\gamma_0\omega > 1/\tau_R$  for  $\omega < 1/\tau_R$ . At higher frequencies, onset of nonlinear effects is related to the strain amplitude rather than rate, as full chain relaxation does not take place on the time scale of the oscillations. Our study allows a comprehensive description of the melt mechanical behavior in the form of a schematic frequency - shear rate diagram shown in fig. 3.16.

We finally mention that the general method presented here is not, in principle, limited to unentangled melts. Indeed, in the general reptation picture, the formula used for the stress tensor is the same as that used in the Rouse model, formula 3.24. The relaxation of the modes will be dramatically slowed down by entanglement effects, so that the viscosity will increase rapidly. Prefactors, however, are associated with equilibrium correlation functions and are not affected by entanglement effects.

## Chapter 4

# Static properties and adsorption desorption at interfaces

### Contents

---

<b>4.1</b>	<b>Introduction</b>	<b>55</b>
<b>4.2</b>	<b>Systems description and preparation</b>	<b>56</b>
<b>4.3</b>	<b>Static properties of chains at the interface</b>	<b>61</b>
<b>4.4</b>	<b>Adsorption and desorption dynamics</b>	<b>69</b>
<b>4.5</b>	<b>Conclusion</b>	<b>84</b>

---

### 4.1 Introduction

Historically, polymer materials were characterized solely by their bulk properties including stiffness, elongation, gas permeability, impact and modulus. Because the bulk polymers were essentially homogeneous, characterization of substructure was not important. Advances in polymer science require advanced methods for polymer micro and nano structure characterization. Polymer nanocomposite materials are now created having clusters, layers, rods, and networks of nanometer sized materials blended with a bulk polymer. A unique aspect of the nanocomposites is the high interfacial volume of the materials, just the opposite of traditional bulk polymers. The chemical and physical properties of the interfaces are what give rise to unique and often desirable properties. The dependence of those properties on the matrix molecular detail and the type of filler is under intense investigation and is far from being understood on a fundamental physical level. The nature of nanocomposites indicates that the key to the understanding of their unique

properties lies in the local microscopic influence of the additive on the matrix. While those effects are for now experimentally inaccessible, computer simulation is well suited to examine features of filler-polymer interaction.

The statics and dynamics of polymer solutions near solid surfaces (adsorption in solution) have been widely studied, but it is not the case concerning polymer melts. Relatively basic questions of the chains statics (such as the number of loops and adsorbed sites of a given chain) have been studied on lattice but not with more realistic continuum-space models. The dynamics (the exchange time of an adsorbed chain with a chain in the bulk melt and its dependence on the molecular weight) has never been studied. Such a study is necessary to fix the relevant time scales involved in the polymer dynamics under mechanical perturbation.

The inhomogeneous systems under study in the present and the following chapter are briefly described in the next section. We will then study the influence of a flat or grafted surface as well as a single spherical filler particle on the static properties of interfacial chains. We will also examine the micro scale dynamics of monomer adsorption/desorption from the flat surface, comparing the measurements to theoretical calculations for simple models.

## 4.2 Systems description and preparation

The polymer model used in this and the following chapters was described previously (see section 3.2). We will discuss simulations of polymer melts near a flat Lennard-Jones potential surface and study the chain conformations in the immediate vicinity of the surface and the microscopic adsorption desorption dynamics.

### Unentangled melt near a flat wall

The typical size of the studied systems was of 6400 particles (for chain lengths of 10 and 50) in semi-periodic cubic simulation box of dimension about  $20\sigma$ .

The introduction of a flat wall or a particle in the system is a process that needs rearrangement and careful equilibration of the system. A wall at  $z = z_w$  is in this case represented by a Lennard-Jones potential  $U_w$  applied to the monomers in the  $z$  direction with  $U_w \rightarrow \infty$  for  $z \rightarrow z_w$ . An attractive wall has the same cutoff distance as the bulk interaction and a given intensity  $\varepsilon_w$  (in the simulation presented here  $\varepsilon_w = 2\varepsilon_{bulk}$ ) whereas a “repulsive” wall has the same intensity but a cutoff of  $\sqrt[6]{2}\sigma$  so that only excluded volume effects are taken into account. The initial state is a pure polymer melt in a three dimensional periodic box. At first the boundary condition following the wall direction ( $z$ ) is set to free, non periodic and coordinates are rescaled accordingly. Then the wall potential is introduced  $z_w$  being large enough (i.e. larger than the system size following  $z$  plus a bulk cutoff distance). In

practice two symmetric walls are set at  $z_w$  and  $-z_w$  and periodic boundaries are kept following the  $x$  and  $y$  directions. Then the walls are moved slowly confining the system roughly to the desired density (the examined density is about 0.925). The obtained state is then equilibrated in a constant NPT ensemble in order to relax to the equilibrium value of the volume. After another equilibration in a constant NVT ensemble, simulations can be ran measuring the system equilibrium properties in the NVT ensemble. A similar scenario is applied for the insertion of a particle - first an insertion phase with a growing sphere in the box center and then NPT-NVT equilibration. The monomer-filler interaction is modeled by a Lennard Jones potential with a shifted distance:

$$U_{fill}(r) = 4\epsilon \left( \left( \frac{\sigma}{r - \Delta} \right)^{12} - \left( \frac{\sigma}{r - \Delta} \right)^6 \right), \quad r \leq r_c + \Delta \quad (4.1)$$

with  $\Delta = 3\sigma$ . The representation chosen for the surfaces as an interaction potential implies that they are perfectly smooth and there is no energy barrier for sliding along the surface while keeping the distance constant.

### Polymer melt near bare or grafted wall

In order to investigate the chain relaxation in the interfacial layer and the influence of the presence of grafted chains additional systems were prepared. We studied chain lengths of 10, 20, 50, 100 and 200 beads with a total number of beads ranging from 6400 to 110000. This allows us to investigate the crossover into the weakly entangled regime, with an entanglement mass  $N_e$  estimated for this model in the vicinity of 65[7]. The melt was confined between walls in the  $z$  direction with  $L_z > 5R_g$  in all cases. The interaction between the wall and the beads consists of an integrated 9-3 Lennard-Jones short range potential. Its parameters were chosen to crudely reproduce the PE - silica interaction. The bead diameter was mapped through the polymer  $C_\infty$  ratio [56] to give  $\sigma \sim 8$ . In order to determine both the number of chemical units per bead and the bead diameter we resolve the equations:

$$(N - 1)b_0^2 C_\infty = (N_{PE} - 1)b_{PE}^2 C_\infty^{PE} \quad (4.2)$$

$$(N - 1)b_0 = (N_{PE} - 1)b_{PE} \cos(\theta/2) \quad (4.3)$$

where  $b_0 = 0.96\sigma$  and  $b_{PE}$  are respectively the bond distance in the bead spring chain and in the PE molecule,  $N$  and  $N_{PE}$  are the number of beads and ethylene monomers and  $C_\infty$  and  $C_\infty^{PE}$  are the stiffness ratios measured in the simulation and experimentally for a PE chain. The described procedure imposes that the statistical coil size and the contour length of the chains in the simulation map the corresponding values in a polyethylene melt. Determining the numerical ratios  $b_0/b_{PE}$  and  $N/N_{PE}$  thus crudely sets the length scale and the number of monomers per bead for the simulation.

We apply a mixing rule using values for the PE and silica interaction intensity found in the literature [57] to obtain for the wall potential length scale  $\sigma_{wall} = 0.6875\sigma$  and intensity  $\varepsilon_{wall} = 0.82\varepsilon$ . The potential is cut off at  $2^{1/6}\sigma_{wall} = 0.77\sigma$  and shifted. It has a repulsive part ( $|z - z_w| \leq 0.59\sigma$ ) and a short range attraction ( $0.59\sigma < |z - z_w| \leq 0.77\sigma$ ). The potential well depth seen by the particles is thus  $0.3\varepsilon$ , much smaller than  $k_B T = 1\varepsilon$ , so that the attraction is very weak. The wall is represented either by the flat wall potential only or by a 111 surface of an FCC lattice made of spherical particles (of size  $\sigma_{wall}$ ), supplemented by the same flat repulsive potential in the second layer to prevent beads from escaping. We have established that the microscopic roughness of the surface does not affect the chain relaxation times. No significant difference was detected when using a flat potential, FCC atomic plane or a square lattice atomic plane with different lattice spacing. Dynamics slowing down due to surface roughness was observed in binary LJ mixtures [58] but this mechanism is irrelevant for our system. As the wall is made of particles smaller than the beads, surface “caging” does not occur, moreover a bead trapped on the surface is immediately pulled out by its bond neighbors. In view of the results above, we believe that with the silica-like wall structure a surface roughness on a scale smaller than the polymer radius of gyration would have a negligible effect on dynamics. For each chain length two systems were prepared: one with a flat wall and one with chemisorbing sites on the wall, where grafted chains are anchored. Silica surface treatment consists in introducing very short chain molecules on the surface that covalently bond with some sites on the surface on one side and with monomers on the other side. The number of bonding sites in the simulation was calculated assuming that 4% of the silica molecules covering the surface of the wall are active and react with the bonding molecule, this number being chosen to reflect experimental situations [57]. The surface density of active sites is therefore  $0.2\sigma^{-2}$ . The resulting bond between a wall particle and a coarse grained bead is chosen to be a soft entropic spring of finite length on the order of several chemical units modelled by a non-harmonic spring:

$$U_{bond} = \frac{\varepsilon_{bond}(r - r_0)^2}{[\lambda^2 - (r - r_0)^2]} \quad (4.4)$$

The spring constant was set to  $\varepsilon_{bond} = \frac{3}{2}k_B T = 1.5\varepsilon$ , the equilibrium distance and the finite extension length are set to  $r_0 = \lambda = 0.8\sigma$ . These parameters define a soft spring freely fluctuating with ambient temperature, that cannot extend further than  $1.6\sigma$  away from the surface. This bond model is inspired by experiment as the grafting molecules are short chains (around 10 carbons). The resulting entropic spring length easily varies with temperature but it has a finite extension.

At first a pure polymer melt was confined at a given pressure ( $0 \leq P \leq 0.8$  depending on the system) between two flat walls. Pressure is monitored

by calculating the normal force on the walls. Then, in order to obtain the system with grafted chains from this initial configuration, a new bond is created between each active wall site and the closest monomer of the melt. Only one bond per active wall site is allowed while a monomer can be bonded to several wall atoms as it is a coarse-grained bead representing several chemical units ( $1 \text{ bead} \sim 6CH_2$ ). There is no preferential bonding for end or middle monomers, matching the physical situation of polymers bonding to silica beads. The new system is now equilibrated at the same pressure as the original system, its pressure being calculated via the force on the wall *and* the grafted chains. All systems were equilibrated for  $5 \times 10^3\tau$  ( $N = 10$ ) to  $5 \times 10^4\tau$  ( $N = 100$ ) and  $4 \times 10^5\tau$  ( $N = 200$ ) before production runs of about  $10^5\tau$ . The equilibration time is in all cases larger than twice the longest polymer relaxation time. For chain lengths smaller than 200 we study both dynamics and entanglements, for the  $N = 200$  systems we perform primitive path analysis only (results in the next chapter), due to the high computational cost for simulating such large systems and the long runs needed to measure relaxation times accurately.

The grafting procedure creates a population of grafted chains near the wall having from 1.4 for  $N = 10$  up to 7 for  $N = 200$  grafted beads per chain (fig. 4.1). The grafted chains extend in all systems a distance of maximum  $2.5R_G$  in the melt (fig. 4.2). There are no bridges between the walls.

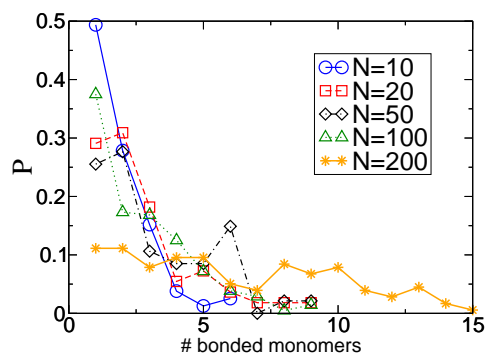


Figure 4.1: Distribution of the number of bonded monomers per grafted chain in the systems with treated surface

### Polymer melt with spherical filler particles

The last family of systems discussed in the next chapter consists of an entangled melt with spherical fillers. The polymer model used differs slightly from the previous one. Monomers are interacting through the previously described Lennard Jones potential (equation 6.1). Chain connectivity is achieved with

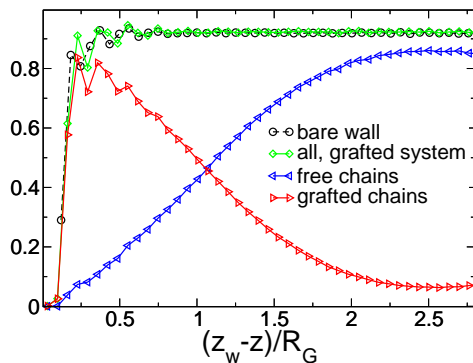


Figure 4.2: Monomer density profile of the system with and without grafted chains for  $N=100$ . The densities of the monomers of the grafted and the free chains are also shown. The density profiles in the other systems have similar behavior.

a harmonic bond potential:

$$U_h(r) = \frac{k}{2}(r - r_0)^2 \quad (4.5)$$

where  $k = 1000\varepsilon$  and  $r_0 = 1\sigma$ . The resulting equilibrium bond length ( $\approx 0.998$ ) is slightly larger than the FENE bond ( $\approx 0.965$ ). The high bond stiffness requires a smaller time step for this system  $dt = 0.002\tau$ , this drawback being partially compensated by the fact that the calculation time for the simpler bond potential is slightly shorter. The length of the polymer chains was 500 beads. The filler-monomer interaction is modelled by the distance shifted Lennard Jones potential (equation 4.1) with  $\Delta = 2\sigma$ . This results in an effective filler diameter of  $\approx 6\sigma$  which is about half the typical size of the chains ( $R_G = 12.1\sigma$ ). We compare the behavior of three different systems: a pure polymer melt (81 chains, 40500 atoms), and a polymer melt with 10% (81 chains and 42 fillers) and 20% (81 chains and 84 fillers) filler volume fraction. The systems were equilibrated in an NPT simulation to  $k_B T = 0.8\varepsilon$  and  $P = 1$ . The equilibration was achieved in the group of J. J. de Pablo (University of Wisconsin) with a Monte Carlo double bridging chain connectivity altering algorithm, which is by far the most efficient way to generate independent equilibrium configurations of highly entangled melts [59, 60]. In the systems obtained the polymer chains are fully relaxed around the filler particles.

### 4.3 Static properties of chains at the interface

#### Density profile and chain dimensions

The first measurements concerned the density profile of the monomers in the vicinity of the wall or the filler particle. The evolution of the fully equilibrated system was monitored during a time period of several times the bulk chain relaxation time (calculated from the Rouse model) and the data was used to build average densities. Given the high density of the melt the formation of layers of monomers close to the surface is expected and can be in fact observed in both the case of a wall and a spherical particle (fig. 4.3, 4.4). The first layer is centered at the equilibrium distance for the interaction potential ( $\sqrt[6]{2}\sigma_w$ ). The layer density is lower for a repulsive surface as expected

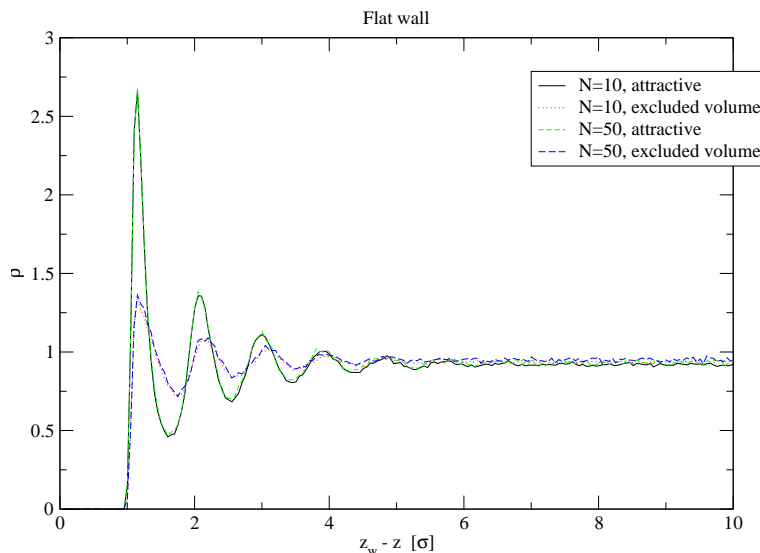


Figure 4.3: Density profile for a flat wall. Measurements have been made for two chain lengths - 10 and 50 monomers both for the attractive and the repulsive case

and the density peaks are a little bit wider and slightly shifted for the second and further layers from the surface. The profile relaxes to the mean bulk density in a distance of about  $4\sigma$  from the first peak. There is no significant dependence on the chain length of the polymers for the equilibrium density profiles. The relative intensity of the peaks depends on the pressure (and therefore density), we have observed slightly less pronounced peaks at lower density, the position of the maxima and minima is unaffected and determined by the length scale of the Lennard Jones potential between the wall and the monomers. These measurements are used to set layer boundaries and give the definition of an adsorbed monomer: we consider that a monomer is adsorbed if it is closer to the surface than the first minimum of the density

profile in the attractive case.

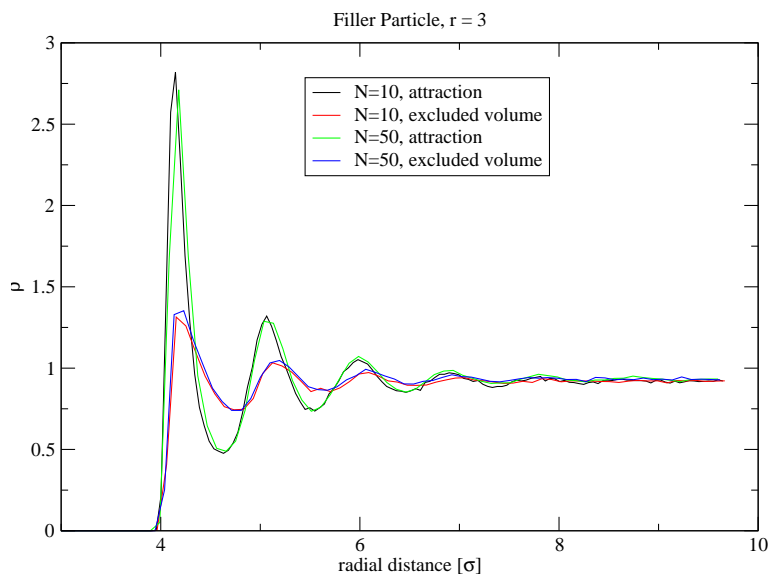


Figure 4.4: Density profile for a filler particle for chain lengths of 10 and 50 in the case of repulsion and attraction

Another important aspect is the relative change of the chain dimensions near the interface. We report these results in the case of a flat wall as well as for a surface bearing grafted chains. The  $z$  component of the mean end to end vector and the radius of gyration of the chains decreases in the vicinity of the wall and there is a very slight increase in the size of the chains parallel to the wall (see fig. 4.5). The effects are observed to extent within about one to two  $R_G$  (bulk value) from the wall, as was established in earlier simulations. [61, 62]

In systems with grafted chains the decrease is slightly more pronounced and extends farther into the melt, up to  $2R_G$  from the wall surface. This slightly larger length scale is close to the typical spatial extension of the grafted chains, that are on average more extended than the bulk chains (see fig. 4.6).

### Characteristics of the adsorbed chains

After obtaining the density profiles we established some more surface-specific static properties concerning the adsorption behavior of the system. Generally, an adsorbed chain consists of three types of segment sequences. These are adsorbed segments (trains), free segments connecting successive trains (loops) and terminal segments starting with a free chain end and terminating just before the first or last train (tails) (see fig. 4.7). A thorough study of the adsorbed chains conformations involves the measurement of the size

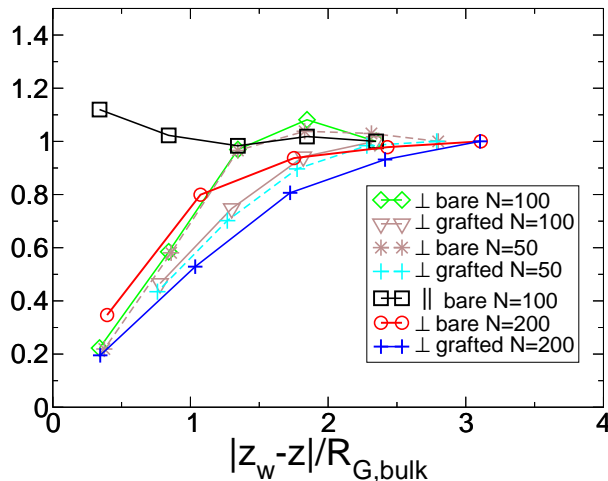


Figure 4.5: Variation of the perpendicular component of the radius of gyration squared, as a function of the distance to the wall divided by the bulk  $R_G$ . The results are normalized by the bulk value  $\langle R_G^2 \rangle$ . The parallel component is shown for  $N = 100$ , the other systems having similar behavior.

distribution of these quantities as well as the number of trains, loops, tails and adsorbed monomers per adsorbed chain.

An important quantity is the distribution of the number of adsorbed (attached) monomers per chain in the cases of different chain lengths, filler radii, and surface-melt interaction. This distribution is obtained by counting the mean number of chains with a given number of monomers in the first layer - results can be seen in fig. 4.8.

The influence of the surface-chain interaction as well as the surface curvature is visible in these results. The attractive surfaces give a broader distribution due to the presence of more strongly attached chains. Strong attachments are also more frequent for a flat surface, in accordance with the fact that a large radius filler is geometrically more favorable for adsorption. The formation of layers shown by the density profile also promotes adsorption independent of the surface-monomer interaction.

### Analytical calculation for the adsorption probability for a random walk

Since the conformations of a polymer chain in a melt are random walk conformations it is interesting to compare the obtained results with the case of a random walk. Here we present a calculation of the probability as a function of the number of attachments in the case of a one dimensional random walk and a flat surface (fig. 4.9). The calculation is based on two formulae con-

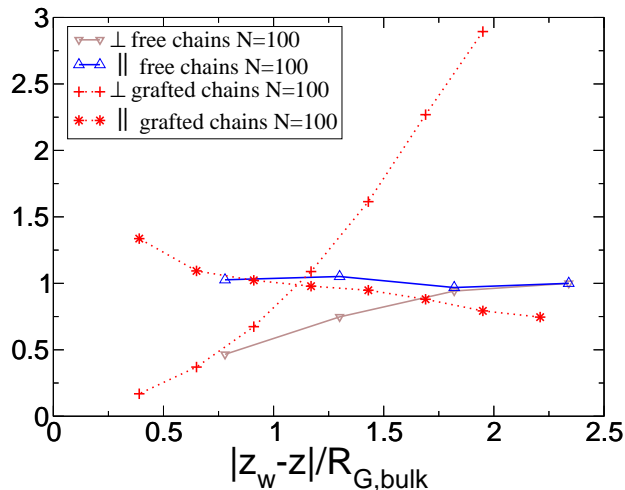


Figure 4.6: Variation of the radius of gyration squared, as a function of the distance to the wall divided by the bulk  $R_G$  for the grafted chains in the  $N = 100$  system. The variation of the dimensions of the free chains are shown for comparison. The results are normalized by the bulk value  $\langle R_G^2 \rangle$ .

cerning random walks, a brief idea of the proof is given here, for a detailed proof see ref. [63].

Let us consider a one dimensional random walk starting from the origin  $z_i = 0$  - the probability that up to and including the  $n - th$  step the random walk returns to  $z = 0$  exactly  $p$  times is given by:

$$z_n^{(p)} = \binom{n-p}{\frac{n}{2}} \frac{1}{2^{n-p}} \quad (4.6)$$

Where  $n$  is even. In fact the number of paths of length  $k$  (necessarily even) joining two  $z = 0$  points is equal to the number of ways to choose  $k/2$  elements among  $k - \binom{k}{k/2}$ . As all these paths have half of their steps going up and half going down a microscopic conformation is equivalent to choosing which  $k/2$  steps should go up among the  $k$  possible steps. This statement can be generalized to give equation 4.6 [63]. Let us again consider a one dimensional random walk starting from the origin  $z_i = 0$  - the probability for a first passage through  $0 < a < n$  on the  $n - th$  step is:

$$f_n^{(a)} = \frac{a}{n} \binom{n}{\frac{n+a}{2}} \frac{1}{2^n} \quad (4.7)$$

Here  $a + n$  is even. Hence a path of length  $n$  joining the origin and a site  $a > 0$  has to go  $(n+a)/2$  times up and  $(n-a)/2$  times down, so the number of those paths is given by  $\binom{n+a}{\frac{n+a}{2}} = \binom{n-a}{\frac{n-a}{2}}$ . The factor  $a/n$  accounts for the first passage and is much more difficult to derive [63].

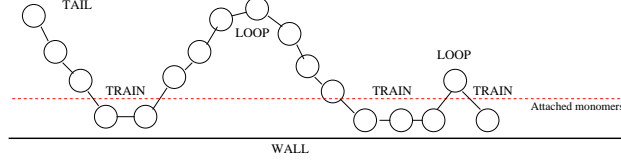


Figure 4.7: Different types of segments for an adsorbed chain. The chain presented here has six attached monomers and the following segments: one tail of length 3, three trains of length 2,3 and 1, and two loops of length 7 and 1. Note that the number of loops is always related to the number of trains as  $loops = trains - 1$ .

Now using equation (4.7) it is straightforward to find the number of paths of length  $n$  touching a plane at a distance  $0 < a < n$  from their origin for the first time after  $r$  steps:  $\frac{a}{r} \binom{r}{\frac{r+a}{2}} 2^{n-r}$ .

We now calculate the number of adsorbed paths: all possible one-dimensional random paths, starting from a given initial position  $z_i$ , having a length of  $n$  steps and touching at least once a plane at  $z_w$  (our wall). Let  $a = z_w - z_i$ , then the total number of adsorbed paths, using (4.7) is given by:

$$Z = 2^n + \sum_{a=1}^n \left[ \sum_{r=a, a+2, \dots}^n \frac{a}{r} \binom{r}{\frac{r+a}{2}} 2^{n-r} \right] \quad (4.8)$$

The term  $2^n$  accounts for the fact that all possible paths starting at the very plane are adsorbed. In the second sum the allowed values are  $r = a + 2k$ ,  $k = 0, 1, 2, \dots$  as follows from the condition  $a + n$  even in equation 4.7. In fact once the surface is reached the next contact can occur in minimum 2 steps and, in all cases, in an even number of steps (see also fig. 4.9). Now we can derive the probability that a random walk of length  $n$ , starting  $a$  positions away from the plane at  $z_w$  has exactly  $t$  contacts with the plane. Using equations (4.8) and (4.6) we have:

$$p_t^{(a)} = \sum_{r=a, a+2, \dots}^{n-2(t-1)} \left( \frac{1}{Z} \frac{a}{r} \binom{r}{\frac{r+a}{2}} 2^{n-r} z_{n-r}^{(t-1)} \right) \quad (4.9)$$

The latter expression is the product of the probability to reach  $z_w$  in  $r$  steps for the first time and then have  $t - 1$  more contacts within the  $n - r$  steps left. Note that any path of length  $n$  having  $t$  contacts cannot start further than  $n - 2(t - 1)$  step lengths from the wall. Normalizing by  $Z$  ensures that any adsorbed path has a probability of 1 to have at least one contact. Now the total probability for an adsorbed path to have exactly  $t$  contacts with the plane can easily be written using (4.9):

$$p(t) = \sum_{a=0}^{n-2(t-1)} p_t^{(a)} \quad (4.10)$$

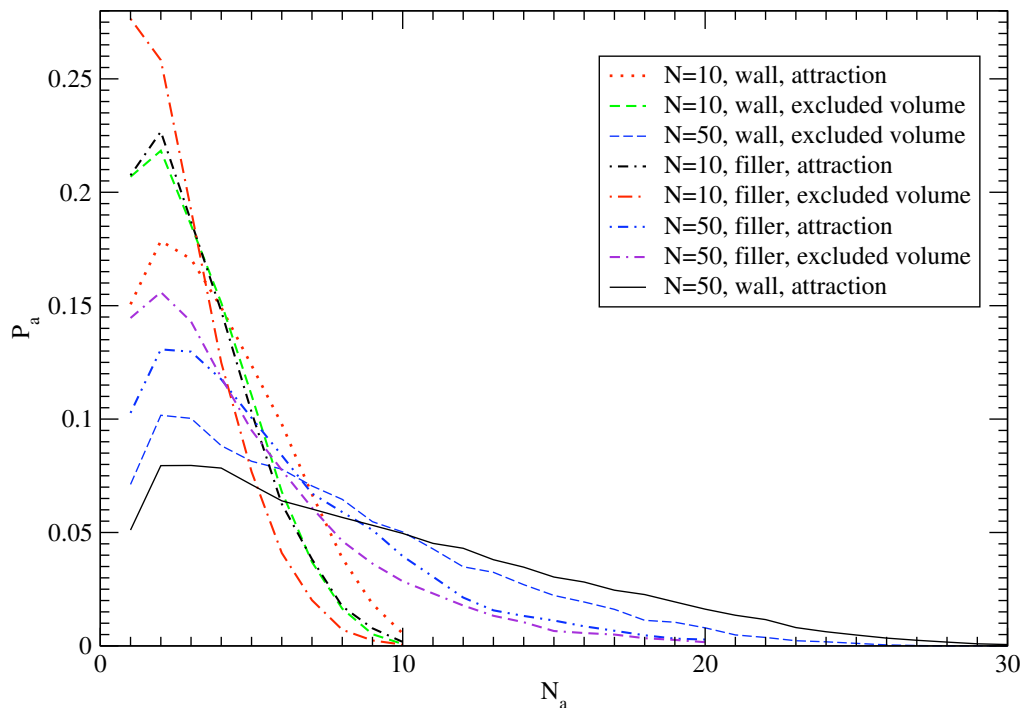


Figure 4.8: Distribution of attached monomers per chain

### Comparison with MD results

An attempt to compare numerical Monte-Carlo results concerning train distributions with random walk calculation was made by Bitsanis and Brinke [64]. Their study involved random walks only starting on the plane and a continuous approach that did not seem to reproduce our measurements. Measured chain conformations were compared with the result given by equation (4.10). The use of a one dimensional model reproduces the chain behavior in a single direction,  $z$ , perpendicular to the wall. As the train length for a one dimensional random walk is strictly zero steps, a single attachment point of the one dimensional walk corresponds to a train for the three dimensional chain (as steps in the  $x$  and  $y$  direction are not taken into account). Thus the probability given by (4.10) is relevant for the train distribution of the chains adsorbed from the melt. We should note also that, for the derivation of (4.10), the wall has been replaced by a penetrable plane. The use of this procedure for counting adsorbed chains makes good physical sense as the ensemble of “penetrating” paths maps onto the ensemble of “reflected” paths. This issue has been widely discussed by Silberberg [65, 64]. Still, the one dimensional walk length  $n$  has to be chosen in accordance with the 3D studied chains containing  $N$  monomers. As successive steps in the random

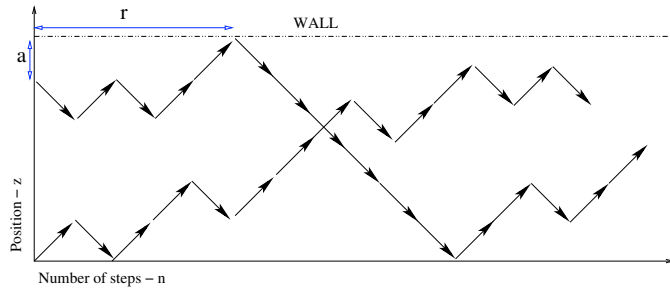


Figure 4.9: Representation of the 1D random walks used to calculate the adsorption probability

walk are uncorrelated the step length in a random path corresponds to the effective bond length  $b$  of the 3D chain. So the 1D number of uncorrelated steps has to verify  $nb^2 = \langle z^2 \rangle = \frac{1}{3} \langle R^2 \rangle = \frac{1}{3} (N - 1)b^2$ , where  $\langle R^2 \rangle$  is the end-to-end mean square distance of a bulk chain and is related to  $b$  by equation 2.1 [43]. A comparison of the analytical result with simulation can be seen in fig. (4.10). The adsorbed chains conformations, as far as the train

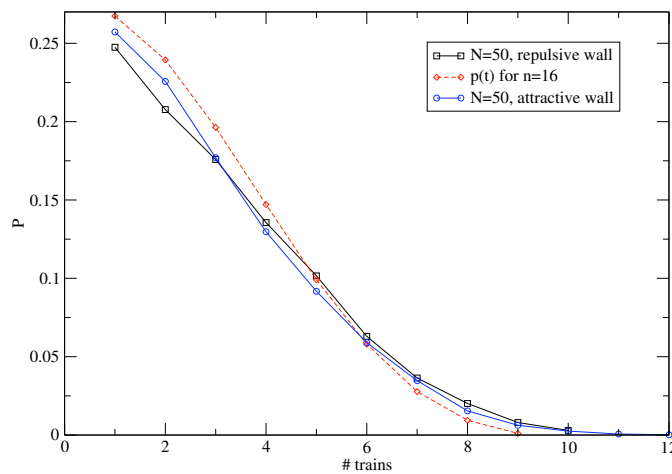


Figure 4.10: Comparison of the derived probability with simulation results in the case of a chain with 50 monomers.  $N = 50$ , which gives  $n = 16.3$

distribution is concerned, follow closely a random walk behavior as predicted by theory.

### Comparison with a 3D random walk

In the case of a filler particle the explicit calculation of probabilities is much more difficult. That is why, in order to compare actual MD results with

random walk results, computer simulations of three dimensional random walks were ran. The random walks were simulated in continuum space and their behavior studied in the presence of both a filler or a flat wall (no interaction whatsoever was implemented between the surface and the random walk and the surface is impenetrable). The step length for the random walk was chosen equal to the persistence length of the bulk chain as discussed above. The number of steps is equal to the number of bonds in the polymer ( $N - 1$  for a polymer of  $N$  monomers). Thus we have the same end-to-end mean square radius for the polymer and the random walk as:  $(N - 1)b^2 = \langle R^2 \rangle$ , and  $b^2 = 1.32$  [43]. These simulations permit also to obtain data for the adsorbed monomers distribution, loop size, train size and tail size distributions for a random walk. The result obtained earlier concerning the number of adsorbed trains is confirmed (see fig. 4.11) whereas the number of adsorbed monomers per chain in the polymer system is the quantity to differ the most from random walks values (see fig. 4.12). A thorough study of all the segment statistics is briefly presented in table (4.1).

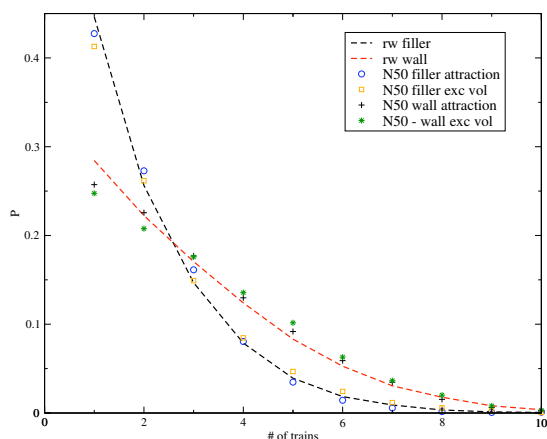


Figure 4.11: Train distributions fitted with values for a 3D random walk

The actual value of the number of adsorbed monomers ( $N_a$ ) is larger for the simulations. This is consistent with our finding that the number of trains per chain is predicted by the random walk model but the length of these trains is greater than predicted.

We associate this discrepancy with the known tendency of polymer chains to lie “flat” on the substrate (fig. 4.5). Since the FENE bond length is shorter than the equilibrium distance of the Lennard-Jones potential, longer trains allow for closer packing of monomers in the attached layer and are therefore favored.

The differences are thus related to the density profile, which is significantly altered by the presence of a wall or a filler both in the attractive

	$10w$	$10wx$	$10f$	$10fx$	$rw10w$	$rw10f$
Adsorbed monomers	3.85	3.27	3.21	2.64	2.25	1.93
Trains per chain	1.54	1.59	1.40	1.42	1.49	1.36
Tails per chain	1.20	1.28	1.36	1.42	1.58	1.63
Monomers per loop	1.99	2.08	2.03	2.06	1.83	1.81
Monomers per tail	4.04	4.13	4.11	4.30	3.42	3.43
Monomers per train	2.27	1.90	2.11	1.73	1.44	1.37
	$50w$	$50wx$	$50f$	$50fx$	$rw50w$	$rw50f$
Adsorbed monomers	9.22	7.30	5.53	4.54	4.74	3.17
Trains per chain	3.04	3.11	2.11	2.16	3.00	2.13
Tails per chain	1.58	1.62	1.76	1.78	1.84	1.88
Monomers per loop	5.03	5.06	4.66	4.74	5.28	5.22
Monomers per tail	19.00	19.50	21.94	22.09	17.99	20.75
Monomers per train	2.97	2.30	2.58	2.07	1.57	1.48

Table 4.1: Measured mean values for adsorbed chains in the studied systems.  $w$  - attractive wall;  $wx$  - wall with excluded volume interaction only;  $f$  - filler particle  $r = 3$  attraction;  $fx$  - filler  $r = 3$  excluded volume;  $rw$  - 3D random walk simulation in continuum space. The two chain lengths studied are 10 and 50

and the repulsive case. In the random walk simulation the distribution of chain starts (or ends) is uniform whereas in the MD simulation it follows the density profile so that the ends of the adsorbed chains are in average closer to the surface, especially for short chains. For this reason MD chains show less tails and more adsorbed monomers than random walks even in the case of non attractive interaction between the surface and the chain. Statistics in the non attractive case show about 0.25 less tails per chain for a length of 10, 0.16 less for a length of 50 and about 10% more adsorbed monomers for chain length of 10 and 5% more for a length of 50. Adsorption is further promoted by the presence of attraction (roughly 5% more adsorbed monomers than the repulsive case) and is stronger in the case of a flat wall (about 6% more adsorbed monomers in the case of a wall) (see table (4.1)).

## 4.4 Adsorption and desorption dynamics

In this section we will study in detail the microscopic dynamics of polymers in the *immediate* vicinity of a flat surface. In order to quantitatively describe those effects one has to gain insight into the relevant time scales involved in the polymer motion in a melt in the vicinity of a surface. The mechanism of desorption in the case of a melt is to a large extent unknown and there are no clear predictions of the typical desorption time. The nature of MD

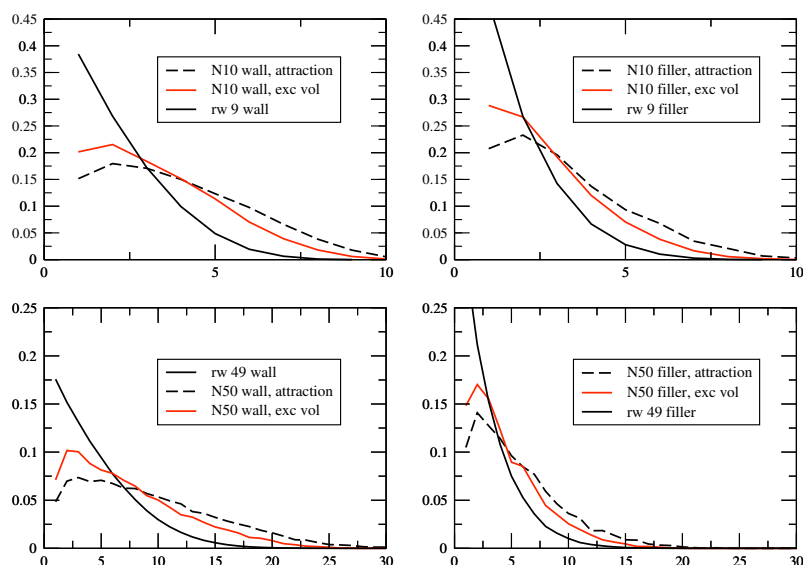


Figure 4.12: Adsorbed monomers distributions in comparison with the case of a random walk. MD distributions are broader than the random walk case due to interaction and density profiles.

simulations permits to reproduce a realistic dynamical evolution of the simulated system and offers, at least in principle, the opportunity to “directly” measure the adsorption and desorption of chains. In this section we will also propose a way to calculate measured times.

### Detachment dynamics by a diffusion model

The population of adsorbed chains in the melt is in constant evolution in equilibrium. Through its evolution we will define the state of an adsorbed chain as the instant value of the number of adsorbed monomers (monomers in the first layer next to the surface)  $0 \leq N_a(t) \leq N$ . We will suppose here that this is the unique parameter describing an attached chain, so that all attached chains having the same number of attached monomers will be considered as a whole regardless of further microscopic detail like trains, loops or tails or specific chain conformation. There are limitations of this approach as this behavior has to be related to the chain characteristics in the interfacial layer extending up to a  $R_G$  from the surface in order to give a more complete picture. Here at first we concentrate on the dynamics of the population of adsorbed monomers only. In order to put the measurements in a concrete theoretical framework, first we present a model describing the detachment dynamics of a population of attached chains, *diffusing* in a set of adsorbed states. In this case we can build a model that is exactly solvable

and gives simple clues about the times scaling behavior and detachment mechanism of the adsorbed chains. This model is not intended to predict exact numerical values, but to explain basic ideas about the detachment mechanism.

Let us consider the properties of the distribution  $P(N_a, t_{att})$  - the distribution for the subset of attached chains which have been continuously attached to the surface for a time of exactly  $t_{att}$ . The distribution will depend on this attachment time. Evidently for  $t_{att} = 0$ , that is for chains which have just arrived at the surface, all of the chains will be attached by exactly one monomer and  $P$  will be a delta function at  $N_a = 1$ . The form of the distribution at long time is of interest. One may expect that an equilibrium distribution is reached as  $t_{att} \rightarrow \infty$ . A prediction of this limit can be formulated.

An attached chain is continually varying  $N_a$  until it detaches. A characteristic transition time  $\tau_{i \rightarrow i \pm 1}$  is defined for each change in  $N_a$  from  $i$  to  $i \pm 1$ . (see fig. (4.13), one can alternatively speak in terms of a transition rate  $k_{i \rightarrow i \pm 1}$  which is the inverse of the respective transition time.)

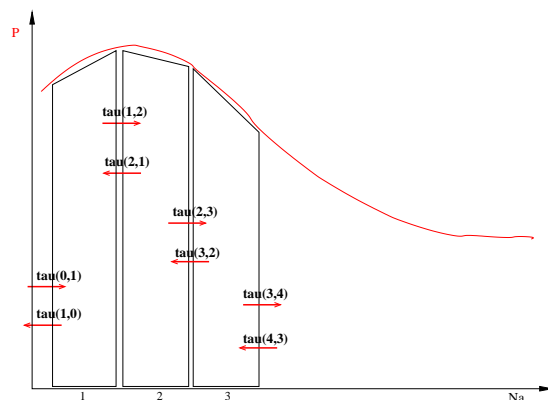


Figure 4.13: Representation of adsorption/desorption transition times. Adsorbed chains in equilibrium migrate between states of different  $N_a$  in a *a priori* transition specific characteristic time.

Now let us consider the evolution of the distribution  $P(N_a, t_{att})$  as a function of the time period the chains have been attached  $t_{att}$ . At any time  $t_{att}$  we are only interested in members of the original set which have *never* left the surface. Thus we are considering the properties of a population whose size decreases to zero over time. Newly attached chains are not considered, the distribution  $P(N_a, t_{att})$ , being independent of the initial time  $t_{att} = 0$ , will evolve following the equilibrium detachment dynamics of the chains. It is useful to distinguish here between absolute and normalized terms. For instance we define  $X(t_{att})$  as the number of chains remaining in the set at

time  $t_{att}$ . The distribution  $P(N_a)$  is of course normalized so that

$$\sum_{N_a=1}^N P(N_a, t_{att}) = 1 \quad (4.11)$$

We define the related value  $F(N_a, t_{att}) = P(N_a, t_{att})X(t_{att})$  which is the actual number of chains in the set with  $N_a$  attached monomers. It follows that

$$\sum_{N_a=1}^N F(N_a, t_{att}) = X(t_{att}) \quad (4.12)$$

The transition times govern the transitions between states of different  $N_a$  and also describe the rate of change of the absolute numbers of chains. For the evolution of the attached by  $i$  monomers chains we can write the following master equation:

$$\frac{\partial F(i, t)}{\partial t} = \frac{F(i+1, t)}{\tau_{i+1 \rightarrow i}} + \frac{F(i-1, t)}{\tau_{i-1 \rightarrow i}} - \frac{F(i, t)}{\tau_{i \rightarrow i+1}} - \frac{F(i, t)}{\tau_{i \rightarrow i-1}} \quad (4.13)$$

To simplify the calculation let us suppose transition times independent of  $i$ :

$$\tau \frac{\partial F(i, t)}{\partial t} = F(i+1, t) + F(i-1, t) - 2F(i, t) \quad (4.14)$$

Supposing the transition time constant means that chains diffuse between states with no preferable direction. So the equation above is a discrete diffusion equation with the diffusion coefficient  $\tau^{-1}$  - characterizing the diffusion between states of different  $N_a$ . So far the system has been treated in discrete terms. For large  $N$  it is reasonable to move to a continuous approach. Then the above equation becomes

$$\frac{\partial F}{\partial t} = \frac{1}{\tau} \frac{\partial^2}{\partial i^2} F \quad (4.15)$$

The boundary conditions are as follows. At  $N_a = N$  there are no more highly attached chains with which to exchange. In other words the flux at  $N_a = N$  is zero:

$$\frac{\partial F(N, t)}{\partial i} = 0 \quad (4.16)$$

As  $N_a \rightarrow 0$  we have the following situation. There is a flux from chains with one attached monomer to chains with no attached monomers which is equal to  $\tau^{-1}F(1)$ . However there is no flux in the opposite direction because chains which become unattached are immediately removed from the set and can no longer participate in its evolution. This is equivalent to requiring

$$F(0, t) = 0 \quad (4.17)$$

With the governing equation 4.15 and these boundary conditions the evolution of any set of attached chains, for instance the delta function at  $N_a = 1$  for chains which have just arrived at the surface, can be described. In particular one would like to know whether the *normalized* distribution  $P(i, t)$  attains a steady form at long times. If this is the case then only the total number of attached chains changes with time. Then

$$F(i, t) = X(t)P(i) \quad (4.18)$$

and equation 4.15 becomes

$$X'P = \tau^{-1}XP'' \quad (4.19)$$

By separation of variables

$$\frac{X'}{X} = \tau^{-1} \frac{P''}{P} = \text{constant} \quad (4.20)$$

The initial condition is  $X(0) = X_0$  and the long time limit is  $X(t \rightarrow \infty) = 0$  so that the constant on the right hand side is negative, say  $-K$ , and

$$X(t) = X_0 \exp(-Kt) \quad (4.21)$$

The boundary conditions for  $P$  are the same as those for  $F$

$$P(0) = 0 \quad (4.22)$$

$$\frac{\partial P(N)}{\partial i} = 0 \quad (4.23)$$

Then solving

$$P'' = -K\tau P \quad (4.24)$$

yields

$$P(n) = A \sin(\sqrt{K\tau}n) \quad (4.25)$$

and from the boundary condition at  $N$ ,  $K = (\frac{\pi}{2N})^2 \frac{1}{\tau}$ . Finally from the requirement that  $\int_0^N P(n)dn = 1$  we have

$$P(n) = \frac{\pi}{2N} \sin(\frac{\pi}{2}n/N) \quad (4.26)$$

This is the distribution of  $N_a$  in the limit of long attachment times. The average number of attached monomers in this limit is

$$\langle N_a \rangle = \int_0^N nP(n)dn = \frac{2}{\pi}N \quad (4.27)$$

And the global detachment time is deduced from the evolution of the total number of chains  $X(t) = X_0 \exp(-Kt) = X_0 \exp(-t/t_{dett})$  that gives

$$\tau_{dett} = \frac{2}{\pi}N^2\tau \quad (4.28)$$

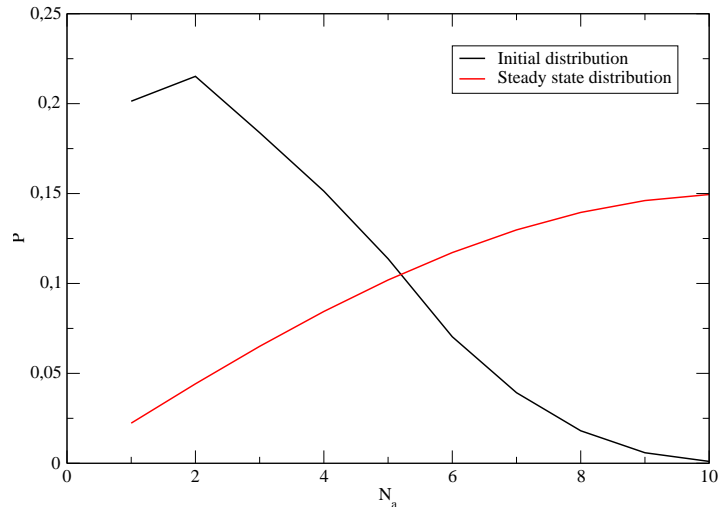


Figure 4.14: Evolution of an initial distribution predicted by the diffusion model. With time any initial condition ends up taking the form of the stationary state normalized distribution. Here the initial condition is the equilibrium distribution for repulsive wall  $N = 10$ . The single transition time is  $\tau = 20$  and the steady state is attained after about  $10 - 20\tau$ .

where  $\tau$  is the time of desorption/adsorption of a single monomer. The model indicates that any initial distribution will evolve towards a steady state described by the distribution from equation 4.26 (see fig. 4.14). The most populated states for the detaching chains are the strongly attached states, as weakly attached chains detach rapidly. The model predicts that the average number of attachments of chains attached for a long time scales as  $N$  - a chain spending a long time on the surface will have a tendency to inevitably lie flat on the surface.

The fact that transition time is constant (with respect to  $N_a$ ) implies that the equilibrium distribution (if incoming flow of attaching chains is included) is flat. This can be seen by applying the detailed balance condition:  $P(i)/\tau = P(i + 1)/\tau$ . Thus at this point it is clear that this model cannot quantitatively reproduce the differences between the different systems only by the adjustment of a single parameter - the transition time.

The scaling predicted for detachment time is  $N^2$  - this is the typical time for a chain attached with  $N_a \sim N$  to diffuse out of the attached population. One can calculate by this model the fraction of initially adsorbed chains that remain on the surface for a given time. This quantity -  $G_c(t)$  is defined as the number of adsorbed chains that stayed on the surface for a time  $t$  divided by the number of adsorbed chains at  $t = 0$ . The result according to the model is shown in fig. 4.15, where as initial distribution we took an equilibrium distribution of the simulated chains from fig. 4.8.

From this graph two distinct regimes are visible - a transition regime for

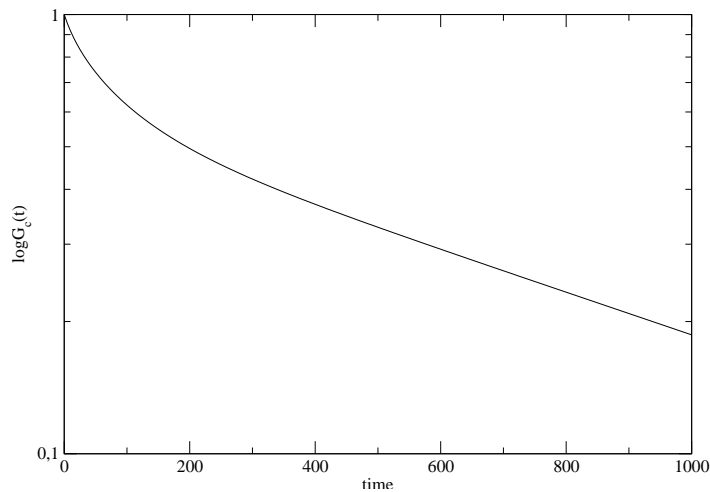


Figure 4.15: Semi log plot of the fraction of adsorbed chains remaining on the surface after a time of  $t$  according to the diffusion model with transition time  $\tau = 20$ . Two regimes are visible - transition period from the initial distribution to the steady state and, after about  $10 - 20\tau$ , an exponential decay in the steady state.

small times between the initial distribution <sup>1</sup> and the distribution given by equation 4.26, and an exponential regime for longer times. The exponential decay means that a steady state is attained and chains detach with a single typical detachment time given here by equation 4.28.

### Detachment times and attachment dynamics

We now turn to direct measurements of the dynamics in the simulations. At first the average lifetime of a chain on the surface has been measured. It is simply defined as the time chains spend in touch with the adsorbed layer divided by the number of adsorptions. This time does not fully characterizes the dynamics of adsorption/desorption: as chains greatly differ by their degree of adsorption a unique typical time is not relevant for all of the adsorbed chains. Here we try to determine the typical time for a complete renewal of an adsorbed chains population. To do so we measure the fraction of initially adsorbed chains that remain on the surface for a given time.  $G_c(t)$  (see fig. 4.16) is defined as the number of adsorbed chains that stayed on the surface for a time  $t$  divided by the number of adsorbed chains at  $t = 0$ .

As expected this fraction decays to zero with a rate dependent on the studied system. Two distinct regimes are visible from fig. 4.16. For short times desorption rate is faster than an exponential decay and becomes ex-

<sup>1</sup>The initial condition for resolving the equations was taken to be our measured equilibrium distribution of fig. 4.8

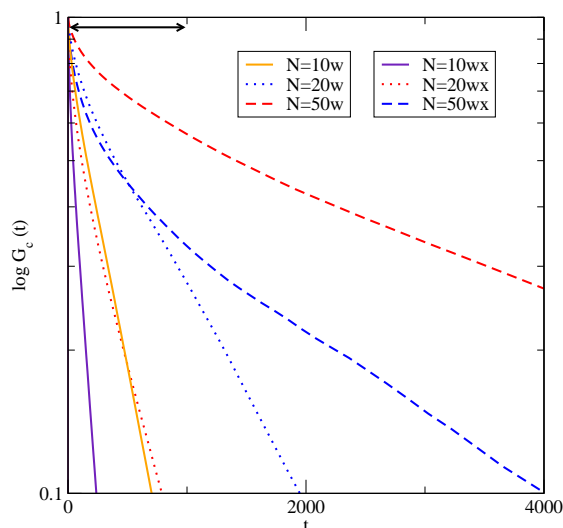


Figure 4.16: Semi log plot of the fraction of adsorbed chains versus time. The rapidly decreasing region is approximately indicated for chain length of 50.

ponential for long times with a well defined time constant. From fig. 4.16 we can define two characteristic times: long time detachment time  $\tau_d^l$  as  $G_c(t) \propto \exp(-t/\tau_d^l)$  for  $t \gg 1$  and mean desorption time -  $t_d = \int_0^\infty G_c(t) dt$ . Results are given in table 4.2.

System measured	10w	10wx	50w	50wx
Average Lifetime	61	24	135	61
$t_d$	270	88	2970	1208
$t_d^l$	333	123	6097	2762

Table 4.2: Measured lifetime, average desorption time and long time detachment time.  $w$  - attractive wall,  $wx$  - wall with excluded volume interaction

The average lifetime is relatively short due to chains that have few attachments. These chains have undoubtedly their center of mass in the outmost region of the interfacial layer. Chains closer to the surface have a substantially longer lifetime exceeding (especially for attractive interaction) their bulk Rouse time (estimated to be  $\tau_R(N = 10) \sim 100$  and  $\tau_R(N = 50) \sim 2600$ ).

### Evolution of attached chains and discussion

The existence of two regimes in fig. 4.16 is the signature of the existence of a steady state that is reached in a certain time from an initial condition, as discussed earlier for the theoretical model. If we consider the distribution

of the attached monomers of the chains that have stayed on the surface for a time of at least  $t$ , this distribution changes considerably with time. As expected from the two regime behavior the normalized distribution reaches a stable constant form with time, and this stationary state gives rise to the exponential decay. The measured evolution of the distribution of attached chains with time is shown in fig. 4.17. There is a significant shift in the distribution's mean value with time: for newly attached chains  $N_a \simeq 1$ , whereas for chains attached a long time  $N_a \sim N/2$ .

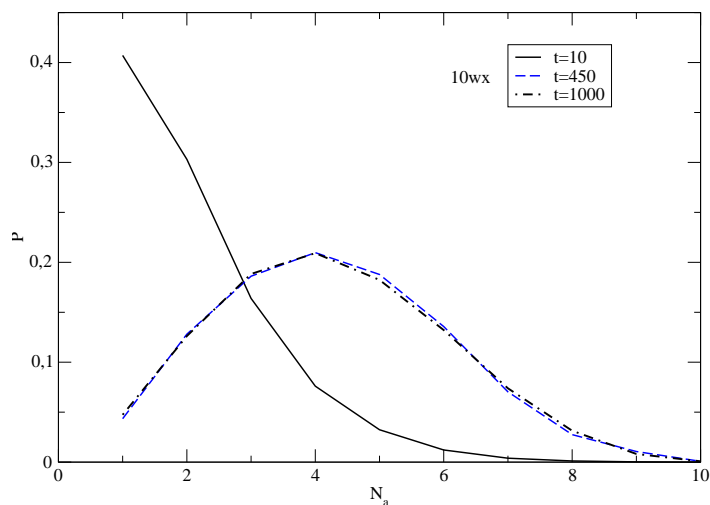


Figure 4.17: The distribution of the number of attached monomers for several times ( $N=10$ , repulsive wall). The initial form is the static equilibrium distribution that evolves towards the distribution of chains that have stayed at least a time of  $t$  on the surface. Newly attached chains meanwhile are not taken into account

If an attached chain survives longer on the surface it migrates towards states of bigger  $N_a$  and “diffuses” around a state of  $\langle N_a \rangle \propto N$  before detachment (fig. 4.18). Thus the first chains to detach are, in their vast majority, those that have stayed on the surface for a short time - they have few attached monomers and detach in a small time (see fig. 4.18). This fraction of “rapid” chains is frequently renewed, on a time scale smaller than the average lifetime, but in order to see *all* adsorbed chains detach one has to wait much longer - this is the second regime in  $G_c(t)$  evolving on a time scale orders of magnitude larger. As the chains that stayed on the surface for a short time are frequently renewed, their contribution to the measurement of the average lifetime is much greater (greater number of adsorptions) so the mean lifetime reflects approximately their time scale <sup>2</sup>.

Through measurement the scaling behavior of the average detachment

<sup>2</sup>For example for  $N = 10$ , *wall* no more than 20% of the newly adsorbed chains stay on the surface longer than  $t = 25$ . The question is further discussed in the next section.

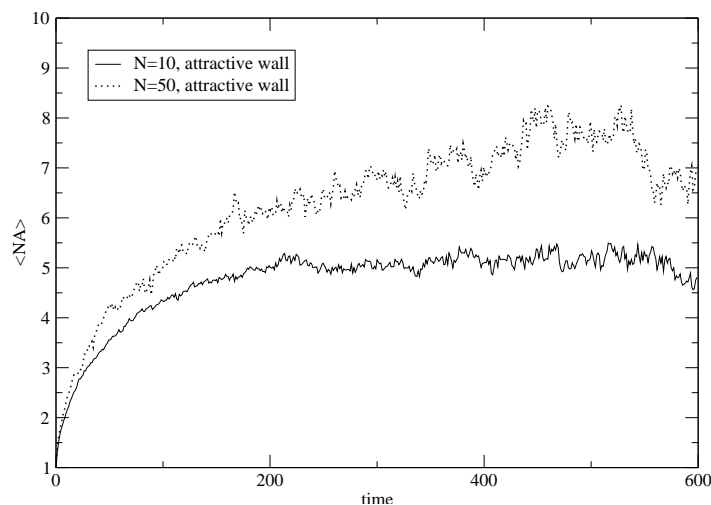


Figure 4.18: Evolution of the number of attached monomers of an attached chain.  $\langle N_a(t) \rangle$  is the mean number of attached monomers of the chains that have been adsorbed for a time of  $t$ . A newly attached chain that stays for a long time on the surface “relaxes” towards states of high number of attachments.

time can be estimated. Results are shown in fig. 4.19. The observed scaling of  $\tau_d$  is close to  $N^2$  ( $\sim N^{2.1}$ ) as predicted by the diffusion based calculation. Both long time detachment time and the average detachment time have the same scaling with  $N$ .

Thus, in an average sense it can be expected that the mean detachment time ( $\tau_d$ ) will be related to the time needed for an adsorbed chain to diffuse a distance on the order of  $R_G$ . According to the Rouse model this time is given by:

$$t_{diff} \approx \frac{\langle R_G^2 \rangle}{D_{CM}} \sim \tau_R \quad (4.29)$$

where  $D_{CM}$  is the center of mass diffusion coefficient (equation 2.12) and  $\tau_R$  is the Rouse time (equation 2.13). The measured scaling behavior is in agreement with the assumption of diffusive desorption. The bulk Rouse time is estimated to be  $\tau_R(N = 10) \sim 100$  and  $\tau_R(N = 50) \sim 2600$ . By comparing the numerical values we can conclude that the chains exhibiting few attachments have undoubtedly their center of mass in the outmost region of the interfacial layer and in consequence need less time to desorb. Chains closer to the surface have a substantially longer lifetime and desorb in a time exceeding, for attractive interaction, their bulk Rouse time. For a repulsive surface the desorption seem to be faster than a bulk relaxation time. It should be noted that, as will be discussed later, the relaxation times as well as diffusion coefficients are modified at the interface and the comparison to the bulk values does not necessarily have a quantitative meaning. We note

that the desorption time discussed here is the time it takes for a chain to take out its monomers from the first surface layer and is not necessarily relevant to the time scale at which the chain leaves the interfacial layer of thickness  $\sim R_G$ . The subject is further discussed in the next section.

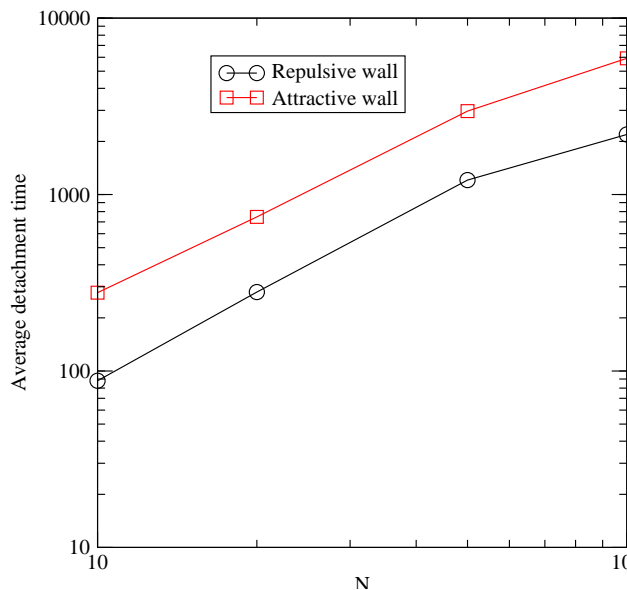


Figure 4.19: Log-Log plot of average detachment times versus chain length for an attractive and repulsive wall. The scaling of  $\tau_d$  is  $N^2$

To further explore the validity of the model the scaling of the average  $N_a$  was measured (fig. 4.20). Measurements do not indicate that for long times  $\langle N_a \rangle \propto N$  but rather a behavior close to  $\langle N_a \rangle \propto \sqrt{N}$  at least for the case of repulsive wall (for long times  $\langle N_a \rangle \propto N^{0.62}$  in the repulsive case). This disagreement should be attributed to the constant transition rates hypothesis and suggests that microscopic detachment needs to be further explored.

#### Microscopic transitions and residence times

After results concerning attachment and detachment phenomena on the scale of a whole chain, attempts were made to characterize the microscopic attachment/detachment dynamics on a typical scale of a single monomer, in order to clarify the behavior of microscopic transition times. To do so a series of measurements were set up. Adsorbed chains were directly monitored during runs - the residence time  $\tau_n$  of a chain in a state with a given number  $n$  of adsorbed monomers (or with a given number of trains) was measured, as well as the number of transitions between the different adsorbed states. There is a subtlety in these measurements, as dynamics at microscopic time scales is strongly blurred by thermal motion. A monomer is considered adsorbed

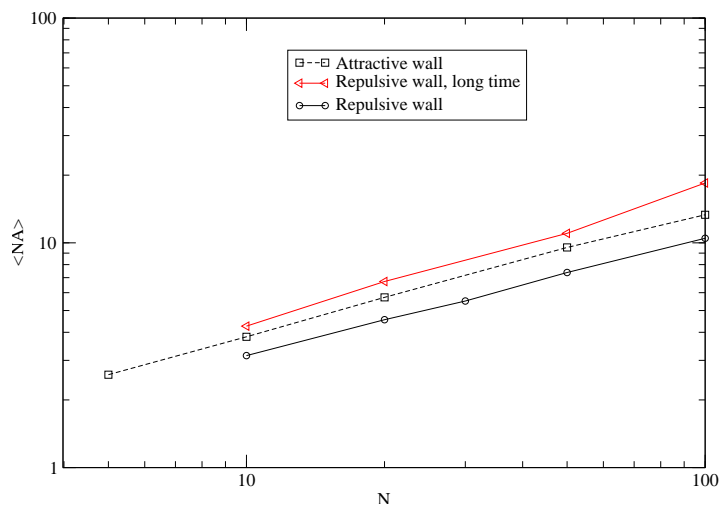


Figure 4.20: Log-Log plot of the average number of attached monomers versus chain length. Scaling is  $N^{0.52}$  for repulsive wall,  $N^{0.55}$  for attractive wall and  $N^{0.62}$  for a repulsive wall for chains attached a long time.

if it is inside a strictly defined region. This definition does not cause any problem for static measurements over a great number of conformations, but yields non physical data in microscopic dynamic measurements. A monomer close to the first layer frontier (set earlier from the density profile), undergoing thermal diffusion, may leave and reenter the adsorbed layer on very short time scales and this movement does not correspond to adsorption-desorption transitions, but to irrelevant thermal fluctuations. To overcome this problem the measurement procedure was modified - the current position of a monomer is replaced by its average position over a small time period  $\tau_0$  (see fig. 4.21) This time period has to be large enough to smooth out very high frequency thermal fluctuations and yet small enough to allow the measurement of sufficiently small time scale transition times. Considering the chain dynamics described by the Rouse model  $\tau_0$  was chosen equal to the smallest relaxation time of a bulk chain of length  $N$  (see equation (2.13)):

$$\tau_0 = \frac{\zeta b^2}{3\pi^2 k_B T} \quad (4.30)$$

this time corresponds to the relaxation of a single monomer inside an ideal chain. According to equation (4.30) with the simulation parameters ( $k_B T = 1, b^2 \approx 1.32, \zeta \approx 20$ , [43]), we have  $\tau_0 \approx 1$ . It should be mentioned that an overestimate of the value of  $\tau_0$  could lead to biased measurements and could mask transitions, that is why a control measurement has been set up to test the assumption that  $\tau_0$  is the proper time scale for a single monomer “pop-up”.

The control consisted in measuring the distribution  $p(\Delta N_a, \Delta t = 1)$  -

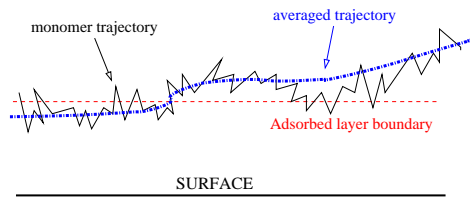


Figure 4.21: Thermal averaging of the monomers trajectory. Averaging over time  $\tau_0$  ensures that thermal fluctuations are not measured as physical transitions

the probability that an adsorbed chain adsorbs/desorbs  $\Delta N_a$  monomers in a time period of 1. Results show that  $\langle \Delta N_a \rangle_{\Delta t=1} < 0.5$  for all studied systems, so that an adsorbed chain has, in all the considered systems, less than 50% chance to desorb/adsorb a monomer in a time of  $\tau_0$ . Thus it is reasonable to state that the relevant time scale to consider for monomer adsorptions/desorption events is larger than  $\tau_0$ , which is also a value that is large enough to ensure the elimination of thermal noise in the dynamical measurements.

A transition time between two neighboring adsorption states (neighboring states of  $N_a = i$  are  $N_a = i + 1$  and  $N_a = i - 1$ ) is defined as the time a chain spends in state  $i$  before migrating to state  $i \pm 1$  (fig. 4.13). In order to verify the hypothesis of constant transition times the transition times of chains attached a long time on the surface have been measured (see fig. 4.22). They give rise to a stationary state distribution that matches the long time distribution of attached chains shown in fig. 4.17. This distribution is characteristic for the time scales proper to the attached chains that have stayed on the surface a long time<sup>3</sup>. If global transition times are measured, including the contribution of chains that have a short lifetime and only a few transitions on the surface, another steady state is to be expected. In order to obtain the right values for the transition times governing detachment one has to restrain measurements on the long-life chains. Results show that transition times are not constant and the approximation made to derive the diffusion model ( $\tau_{i \rightarrow i \pm 1} = const$ ) is not valid in our system<sup>4</sup>.

The average time a chain stays in a given  $N_a$  state was also measured. Residence times in highly attached states are shorter in all systems and essentially constant when  $N_a \rightarrow N$  (see fig. 4.23). This fact does not imply faster adsorption on a single monomer scale, but is due to the fact that strongly attached chains have many monomers near the adsorbed layer and thus more chances to exchange monomers with the first layer per time step.

<sup>3</sup>A time long enough for the initial distribution (which is the equilibrium distribution) to evolve towards the steady state distribution

<sup>4</sup>This was already stated before as the equilibrium distribution predicted by the diffusion model is flat, unlike those observed in the simulated systems

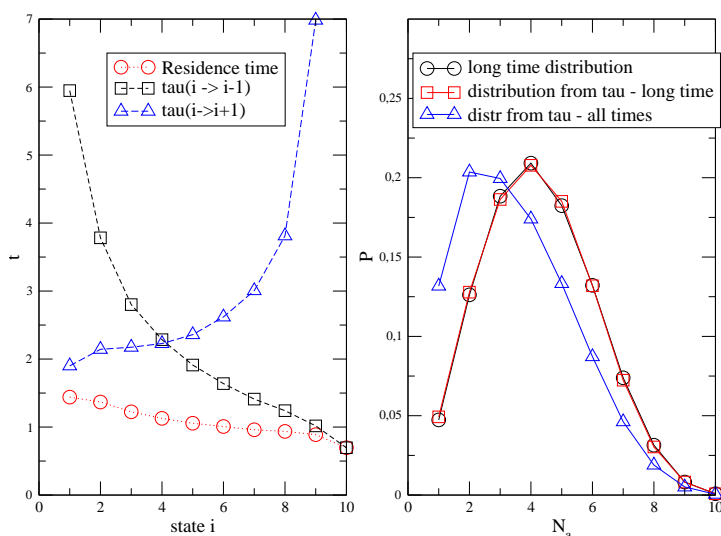


Figure 4.22: **Left:** Transition and residence times for adsorbed states and strongly attached chains ( $N=10$ , repulsive wall). **Right:**  $N=10$ , repulsive wall: The distribution of strongly attached chains calculated first from static data and then by finding a stationary state distribution for the master equation using the measured transition times. In blue is the stationary distribution according to overall transition times. It does not match the strongly attached chains stationary distribution (because of the contribution to transition times of weakly attached chains)

So a particular transition/residence time depends not only on the actual state, but also strongly on the particular chain conformation - the chain specific number of trains, tails and average position. As the number of trains of a chain is not simply related to its number of attached monomers, its influence on transition times is hard to extract. One can argue that if a chain is strongly attached it has *on average* the mean number of trains for the specific system (measurements shown in the previous section) so its residence times are expected to be constant *on average*, a hypothesis supported by measurements.

As the adsorption and desorption time depend on the chain's conformation (therefore on its past evolution), it is reasonable to think that a desorbed previously "strongly attached" chain has good chances to be strongly reattached again (see fig. 4.24). The real exchange between free melt chains and chains close to the surface could be further slowed down by a chain diffusion time. This question cannot be answered with our data for now and will be addressed further in the next chapter.

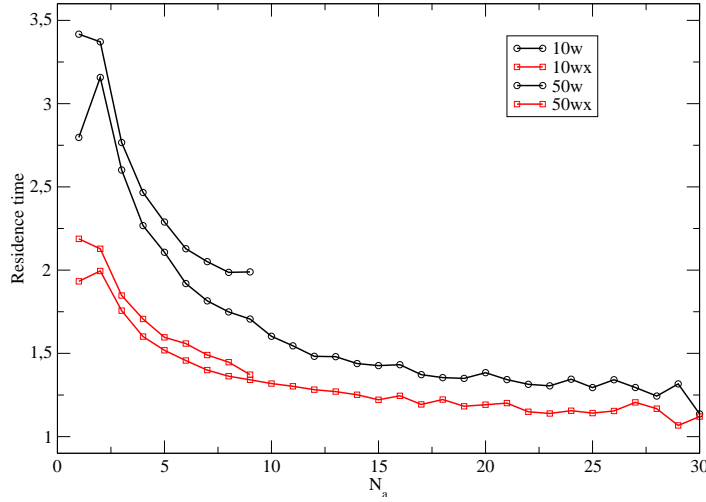


Figure 4.23: Average residence times per microscopic state considering all chains

#### Detachment times description in terms of master equation

Quantitatively more adequate description of the detachment dynamics is obtained by solving equation 4.13 without the hypothesis that all transition times are constant. Transition times are chosen as follows:

$$\tau_{i \rightarrow i-1} = \langle \tau_{tr} \rangle, \quad i = 1..N \quad (4.31)$$

$$\tau_{i-1 \rightarrow i} = \frac{P^l(i-1)}{P^l(i)} \tau_{i \rightarrow i-1} \quad (4.32)$$

where  $\langle \tau_{tr} \rangle$  is an average value over transition times and  $P^l$  is the long time  $N_a$  distribution (fig. 4.17). The initial condition is the overall static equilibrium  $N_a$  distribution and the choice of transition times shown above ensures that the initial distribution will evolve towards  $P^l(i)$  which is, making this choice for transition times, a stationary solution of the master equation. Desorption times calculated using this model are in good agreement with measured values (see fig. 4.25). The first regime is considerably shorter (but exists) for calculated values which is a logical consequence of replacing half of the transition times by a single average value. The implementation of the right long times  $N_a$  distribution in the model gives correct values for desorption times.

This calculation further emphasizes the ingredients that play a major role in the process of desorption. Using equilibrium distributions of attached monomers on the surface and a relevant microscopic transition time one could determine desorption time scales for different systems. Thus, by studying the dependence of microscopic transitions on surface interaction, chain length or filler radii, conclusions about global desorption times can be drawn.

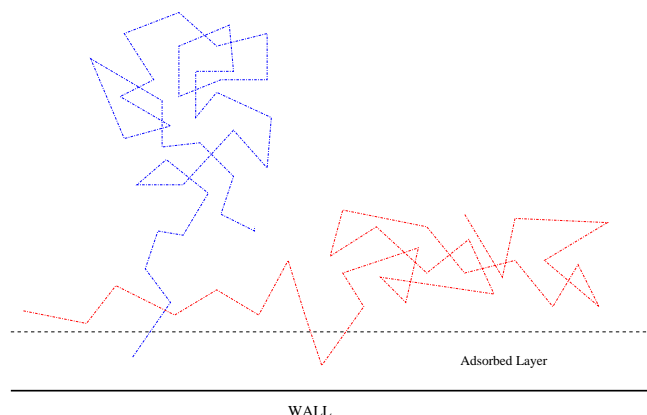


Figure 4.24: Two possible chain conformations for chains with  $N_a = 1$ . The blue chain is likely to rapidly detach and the red chain has good chances to turn out a “strongly attached” chain.

## 4.5 Conclusion

We first examined the static properties of polymers in a melt in the presence of a flat surface, flat surface bearing grafted chains or a filler particle. The chain size is affected by the presence of the wall in a layer up to two  $R_G$  from the wall surface. Static conformations near the surface were compared to predictions from a random walk model and found to be in good agreement for the number of trains per chain. The length of the trains is larger than in the random walk model, reflecting a tendency of chains to lie flat on the surface.

Next we measured the microscopic adsorption-desorption dynamics by following the evolution of chain conformations as described by a *single* parameter  $N_A$ , the number of “attached” monomers. The population of chains is shown to contain a portion of weakly adsorbed chains with rapid desorption dynamics and strongly adsorbed chains with slower desorption dynamics. The strongly adsorbed chains are responsible for a slow-down in dynamics immediately near the surface. Slower desorption is observed for an attractive surface. The desorption time is seen to scale slightly slower than  $N^2$ , for chains up to  $N = 100$ . A kinetic model for chain desorption was proposed to rationalize the behavior and conformation of strongly adsorbed chains. If a simple “diffusion” model in terms of the variable  $N_a$  (number of adsorbed monomers) was adopted, such a model would yield a desorption time scaling as  $N^2$ . Our results indicate a more complex behavior in that the behavior of chains depends not only on  $N_a$  but also on the time a chain has been attached to the surface. This suggests that to sufficiently describe the dynamics more parameters are needed, for instance, the distance of the chain center of mass from the surface. For a better understanding of the melt dynamical behavior

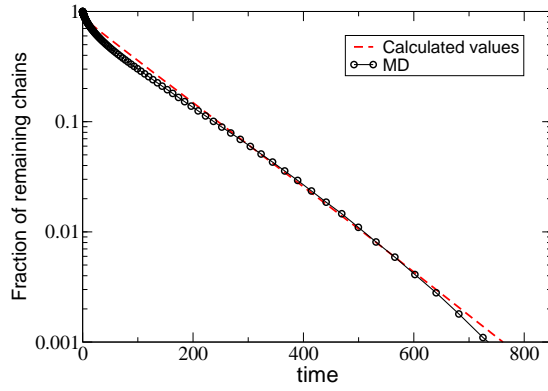


Figure 4.25:  $G_c(t)$  for  $N=10$ , repulsive wall. Comparison between values measured in simulation and obtained by solving the master equation.

at the interface a larger portion of material near the wall should be carefully considered.



## Chapter 5

# Dynamics and entanglements in the interfacial layer

### 5.1 Introduction

The properties of polymer-filler composites are often associated with filler clustering and percolation [32, 66] but several studies over the past years showed that the effect is also observable below the percolation threshold [36, 67]. This indicates that the particle-matrix interface is another crucial ingredient in the complex physics of filled elastomers. Another indication of the importance of surface effects lies in the fact that small size particles (nanoparticles) have a much greater effect compared to micron size fillers. The nature of the polymer filler interactions was shown to be very important, it was established by experiment [35] and simulation [58] that attractive interactions lead to an increase of the glass transition temperature near the interface. With this argument an explanation of reinforcement has been put forward involving the formation of “harder”, glassy layers with slow dynamics around attractive fillers. Yet this explanation is not sufficient as reinforcement (a lower value, but still around 100%) was experimentally measured in nanocomposites at temperatures twice as high as the glass transition temperature of the matrix [36]. Most of the fillers used in practical applications (tires) and leading to substantial reinforcement, such as treated silica particles, exhibit a globally repulsive interface with some sites that can covalently bond polymer chains from the melt. The micro scale physics of interfacial reinforcement remains unclear in this case. Experimental studies [36] suggested that chain entanglements in the vicinity of the surface should play a major role in the reinforcement which can be explained by the presence of trapped entanglements near the interface. Theoretical studies have qualitatively suggested that the density of entanglements decreases in the vicinity of a wall [68, 69] because of the average decrease in chain dimensions established earlier by simulation [62, 61]. On the experimental side the validity of

this assumption was recently questioned for free standing films [12]. Other experimental results suggest a depletion in the entanglement density and report a decrease in viscosity in thin films [11]. Clear evidence of this phenomenon on the microscopic level near a flat wall is still lacking, and it could not be related to mechanical properties.

Recent advances in molecular simulation has made possible a precise study of these problems. The well established concept of entanglement in a polymer melt can be “observed” by direct primitive path analysis [7, 70]. As we discussed in chapter 3, we developed an equilibrium method for studying the mechanical properties of a melt that can be used to assess local viscoelastic properties [71].

Using these tools, in the present chapter we analyze the dynamics and the entanglement density of a polymer melt near a repulsive wall with or without bonding sites and give a generic explanation of the melt slowing down or acceleration at the interface as a function of molecular weight. The systems under study were described in the previous chapter. We will concentrate on the chain relaxation and dynamics in the whole interfacial layer in the case of flat wall compared to the case of a wall bearing grafted chains. An analysis in terms of primitive paths will be used to study the entanglement network in these systems. At last a study of the entanglements in the previously described high molecular weight melts with a fraction of spherical filler particles (10% or 20%) will be presented.

## 5.2 Local dynamics near a bare and grafting wall

In this section we study the dynamics at a flat melt-wall interface compared to the case of a grafted wall. The position of the chains center of mass is taken into account so that the difference between interfacial and bulk dynamics can be clearly identified.

### 5.2.1 Desorption and Mean Square Displacement

We can get a qualitative idea of the melt dynamics in the bulk and near the surface by looking at the local mean square displacement of the polymer chains. We define the bulk and interfacial chains mean square displacement by:

$$\langle R^2(\tau) \rangle_{bulk} = \frac{1}{TN_{ch}^z} \int dt \sum_{i; -\sigma < Z_{cm}^i(t) < \sigma} (R_i(t+\tau) - R_i(t))^2 \quad (5.1)$$

$$\langle R^2(\tau) \rangle_{wall} = \frac{1}{TN_{ch}^z} \int dt \sum_{i; z_w - 2\sigma < |Z_{cm}^i(t)| < z_w} (R_i(t+\tau) - R_i(t))^2 \quad (5.2)$$

In the case of a bare surface we find that surface chains have increased mobility parallel to the surface in the  $x$  and  $y$  direction compared to bulk

chains and they are slowed down perpendicular to the surface. For a wall with grafted chains the free chains in the wall vicinity are slower in the parallel direction (fig. 5.1) - this is attributed to the presence of the grafted chains acting as obstacles for motion parallel to the wall.

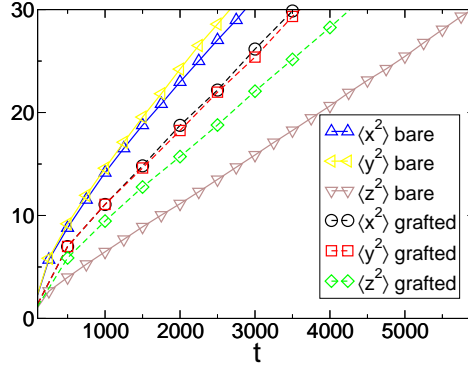


Figure 5.1: Monomer mean square displacement in the wall vicinity for the system  $N = 20$  with and without grafted chains.

A more surprising result is that, in the presence of grafted chains, the free chains are faster than the chains near a bare wall in the perpendicular direction (fig. 5.1). This kind of behavior can be understood knowing the desorption mechanism from a flat surface discussed in the previous chapter [72]. As was already mentioned, even in the case of a flat repulsive wall, surface chains having relaxed conformations with many monomers on the surface are very slow to desorb and are thus responsible for a slowing down in dynamics near the surface. This is seen in the perpendicular slowing down in the bare wall system. In the presence of grafted chains, there are fewer free chains near the surface, as the corresponding conformations are taken by the grafted chains that do not desorb. The presence of grafted chains makes the surface rough on a scale comparable to the polymer size, it can be argued that adsorption and desorption on a rough surface for polymers is faster as it involves less entropy loss than in the case of a flat wall [73]. Thus the free chains population near the surface has faster exchange dynamics with the bulk chains.

### 5.2.2 Local Dynamics from Rouse Modes

We study the local dynamics of the polymer chains by again monitoring the relaxation of the Rouse modes of the chains (equation 2.16). As correlation of the  $p$ -th Rouse mode describes the relaxation of a sub-chain of  $N/p$  monomers, the study of this quantity allows to probe the dynamics on different length scales. Being a local single chain quantity, the correlation of the

Rouse modes allows us to investigate the dynamics in different sub-volumes of a non-homogeneous system, provided they contain a large enough number of chains. It is also a route to estimate the local viscosity in each region (discussed in chapter 3). In our confined systems, we define the relaxation of local modes as a function of the  $z$  coordinate as:

$$\langle X(\tau)X(0) \rangle(z) = \frac{1}{TN_{ch}^z} \int dt \sum_{i; z-dz < Z_{cm}^i(t) < z+dz} X_i(t+\tau)X_i(t) \quad (5.3)$$

It is expected that the slowest Rouse mode relaxes on a time scale smaller than the time needed for a chain to diffuse its own size. Hence, we choose a slice width on the order of  $R_G$ , so that the center of mass of a chain stays (statistically) within the same slice while the correlation is measured. This allows us to access local dynamics with a spatial resolution on the order of  $R_G$ , which is better than the resolution associated with measurements of the mean square displacement. For the systems with grafted chains we define relaxation times by considering *only the modes of the free chains*. Hence the values of the relaxation times shown in this study are not affected directly by the frozen dynamics of the tethered chains. Our goal is to understand the influence of the presence of the grafted chains on the remaining melt and to capture, if any, matrix mediated slowing down.

For short chains ( $N \leq 20$ ) we estimate the Rouse times by an exponential fit of the normalized correlation function of the first mode, which have in all cases a clear exponential behavior. We estimate separately the relaxation of chain conformations following the three directions in order to take into account the spatial inhomogeneity near the surface. For chain lengths of  $N = 10$  and  $N = 20$  we observe a clear decrease in the relaxation times of the modes near the wall in all systems, regardless of the presence of grafted chains (fig. 5.2). In the case of a flat surface this acceleration is expected and can be understood in terms of reduction of the monomeric friction due to the repulsion of the surface [58]. We also studied the influence of the pressure and the microscopic wall roughness on the acceleration of the chains. They were found to have a negligible effect on the modes relaxation times in the melt. Cage effects associated with microscopic roughness of the wall are relatively unimportant for chain molecules compared to simple fluids, due to the competition with bond constraints associated with the neighboring monomers in the chain.

As the grafted chains act as soft obstacles for the free chains one could expect that the free chains will be slower close to the wall than in the bulk. Studying the local Rouse times we find that this assumption is not true for melts with chain lengths  $N = 10, 20$ . In the systems where there are attached chains on the surface, the free chains in the immediate vicinity of the wall are still accelerated with respect to the bulk chains. The effect of the grafted chains is seen when comparing the systems with and without

grafted chains. In the direction parallel to the surface the free chains in the immediate vicinity of the wall having grafted chains are about 20% ( $N = 10$ ) and 30% ( $N = 20$ ) slower compared to the chains seeing a bare repulsive surface, but they are still accelerated by 20% ( $N = 10$ ) and 10% ( $N = 20$ ) compared to the bulk dynamics (see fig. 5.2). In the perpendicular direction the chain conformations equilibrate in about the same time for the two types of systems. For these systems of short chains, the slowing down due to the grafted chains is not sufficient to overcome the acceleration due to the repulsive surface and we do not expect reinforcement with respect to the bulk properties of the material, as discussed in the next section.

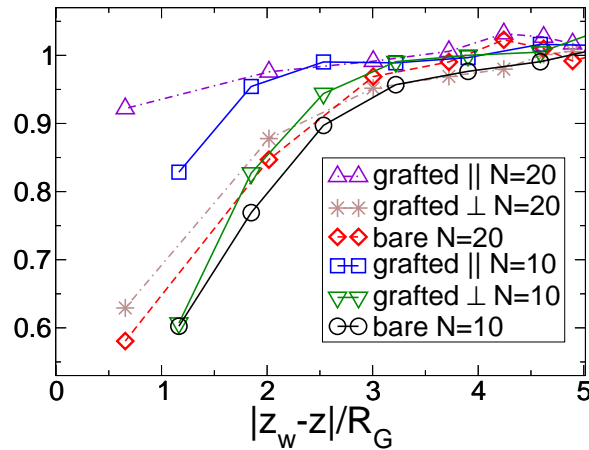


Figure 5.2: Local Rouse times normalized by the bulk value for chain lengths of 10 and 20 and for the free chains in the systems with grafted chains (referred to as “grafted”) and for the chains in the system without grafted chains (referred to as “bare”).

For chain lengths  $N > 20$  we measure the modes relaxation times as the integral of the normalized correlation function so that an exponential behavior of the latter is not required. Although the relaxation is not strictly exponential, the resulting values are close to those that would be obtained using an exponential fit. For chain lengths around and above the entanglement length we observe an acceleration for the first Rouse mode in the case of a bare wall, very similar to the case of short chains. The influence of grafted chains, however, is much more important than for short chains. In the systems with grafted chains of  $N = 50, 100$ , we measure a slowing down for the largest relaxation time in the parallel direction (of around 10% for  $N = 50$  and 40% for  $N = 100$  within a distance of  $R_G$  from the wall) with respect to the dynamics in the middle of the film (see fig. 5.3). The average relaxation times in the layer feeling the presence of the grafted chains are larger than

those for the system without grafted chains. On average, for  $N = 100$ , the mean relaxation times of the first five Rouse modes are increased by  $\sim 20\%$  in the presence of grafted chains, compared to what is observed for a bare wall (see fig. 5.4). In summary, the presence of grafted chains induces a slowing down for all modes (compared to the bare wall case), and in the case of the first mode a slowing down compared to the bulk is also observed.

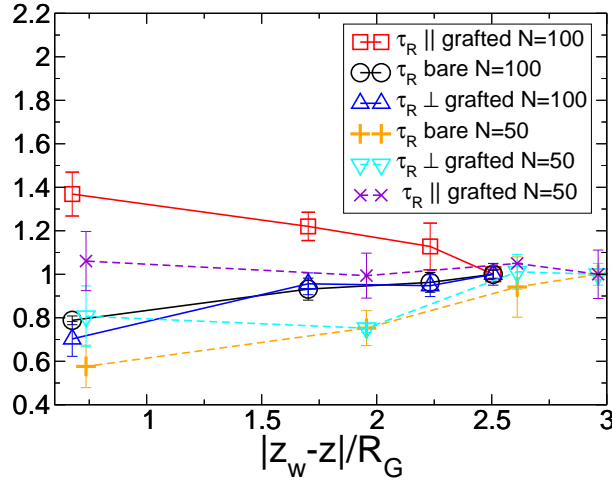


Figure 5.3: Local Rouse times (first mode), normalized by the bulk value, for chain lengths of 50 and 100 and systems with and without grafted chains.

In the  $z$  direction the conformation dynamics varies in a similar way as a function of the distance to the surface, regardless of the presence of grafted chains.

In the following, we argue that the substantial slowing down observed in the relaxation time of the first mode is due to entanglement effects near the surface. If the slowing down is due to entanglements, we should still have faster dynamics close to the surface for chain segments well below the entanglement threshold. In other words, the relaxation of a mode  $p$  such that  $N/p > N_e$  should be slowed down when approaching the wall, while the dynamics of a mode  $p$  satisfying  $N/p < N_e$  should be similar to the unentangled case, i.e. accelerated with respect to its value in the middle of the film. This assumption is confirmed by the measurement of the relaxation of higher Rouse modes of the chains (see fig. 5.6). In terms of effective monomeric friction the presence of the repulsive surface still leads to relative acceleration of the dynamics in the immediate vicinity of the wall on length scales smaller than the tube diameter (as in the case of unentangled chains). This leads to a relative acceleration of the small scale modes in the interface layer when approaching the wall. On the scale of entanglements the shorter the distance to the wall is, the slower the dynamics. This issue will be further

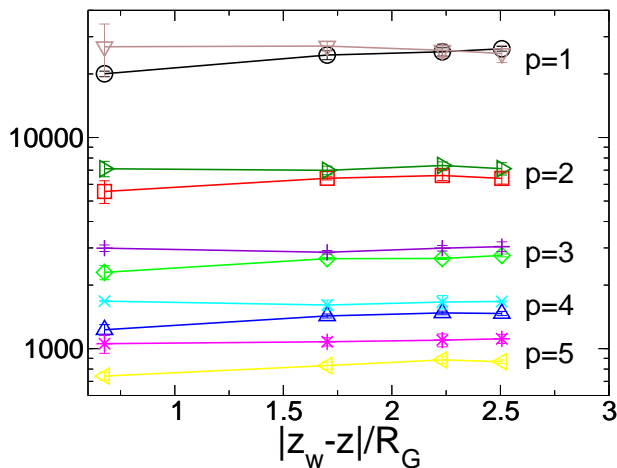


Figure 5.4: Local relaxation times of the first five Rouse modes for chain length of 100 for the systems with and without grafted chains. The system without grafted chains is systematically the faster one. Bare wall:  $p = 1$ : circles,  $p = 2$ : rectangles,  $p = 3$ : diamonds,  $p = 4$ : triangles,  $p = 5$ : left triangles; Grafted:  $p = 1$ : down triangles,  $p = 2$ : right triangles,  $p = 3$ : pluses,  $p = 4$ : crosses,  $p = 5$ : stars;

investigated in terms of entanglements in the next section.

In summary, the presence of the flat surface results in the formation of an interfacial layer where the dynamics and chain conformations are different from the bulk. The presence of the surface alters the dynamical properties of the melt in its vicinity within around two to three bulk  $R_G$ . The presence of grafted chains on the surface increases the thickness of the interfacial layer as far as static properties are concerned due to the tendency of the grafted chains to have an extension larger than the bulk  $R_G$ .

In the unentangled regime, the presence of a repulsive surface results in a relative acceleration of the melt dynamics when approaching the wall regardless of the presence of grafted chains on the surface. The presence of grafted chains (below the polymer brush density) slows down the free chains dynamics parallel to the surface compared to the system without grafted chains, but chains are accelerated with respect to the bulk.

The situation changes when the chain length increases and we enter the entangled regime. In the case of entangled melts, the relaxation of entangled modes  $p$  such that  $N/p > N_e$  is slowed down compared to the bulk near the surface in presence of grafted chains. In the next section we will relate this to the local entanglement density. The local dynamics at length scales shorter than the entanglement length is slower with grafted chains than without, but remains accelerated close to the surface with respect to the bulk.

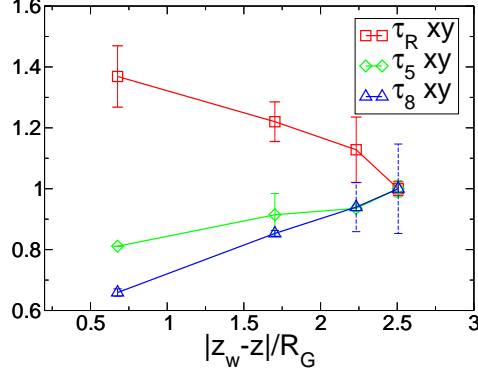


Figure 5.5: Local relaxation times ( $N=100$ ) normalized by the bulk value of the first (entangled) mode and of higher modes for the free chains in the system with grafted chains.

In the perpendicular direction adsorption-desorption dynamics are slightly accelerated compared to the system without grafted chains. This is due to the fact that the slowest chains in the vicinity of a flat wall tend to be those with most contacts with the wall [72]. In the grafting process, these chains are removed from the population of "free" chains that we consider here.

### 5.2.3 Local stress relaxation function

Next, we calculate the local stress relaxation in our systems using the method previously discussed for pure melts. We have seen that this quantity can be used to calculate the melt viscosity in the bulk and we will use it here to provide a local estimate for  $\eta$ . The stress correlation function can be calculated from equation 3.24, in this case each mode  $p$  of the chains has a contribution of:

$$G_p(t) = \frac{\rho k_B T \langle X_{p\alpha}(t) X_{p\beta}(t) X_{p\alpha}(0) X_{p\beta}(0) \rangle}{N \left( \frac{\langle X_{p\alpha}^2 \rangle + \langle X_{p\beta}^2 \rangle}{2} \right)^2} \quad (5.4)$$

where  $\alpha, \beta = x, y, z$ . Here we calculate these quantities locally in slices parallel to the wall, as for the Rouse modes in the previous section:

$$\langle X_{p\alpha}(t) X_{p\beta}(t) X_{p\alpha}(0) X_{p\beta}(0) \rangle(z) = \quad (5.5)$$

$$= \frac{1}{TN_{ch}^z} \int ds \sum_{i; z-dz < Z_{cm}^i(t) < z+dz} X_{p\alpha}^i(s+t) X_{p\beta}^i(s+t) X_{p\alpha}^i(s) X_{p\beta}^i(s)$$

$$\langle X_{p\alpha}^2 \rangle(z) = \frac{1}{TN_{ch}^z} \int ds \sum_{i; z-dz < Z_{cm}^i(t) < z+dz} (X_{p\alpha}^i(s))^2 \quad (5.6)$$

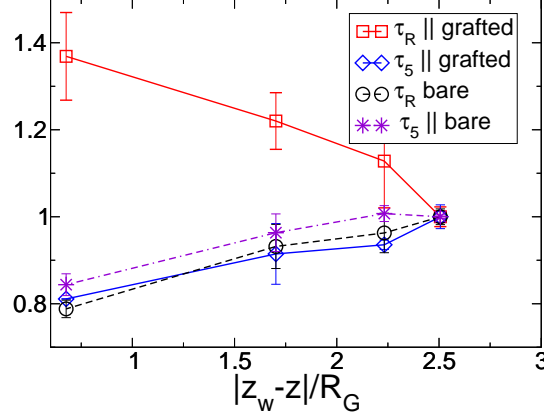


Figure 5.6: Relative variation of local relaxation times normalized ( $N=100$ ) by the bulk value. The first (entangled) mode and the fifth mode for the free chains in the system with grafted chains and the chains near a bare surface are shown. All modes except the first mode in the grafted system follow the same qualitative behavior and are accelerated close to the surface. The first mode of the free chains in presence of grafted chains is slowed down.

The contribution to the viscosity of the mode is  $\eta_p = \int_0^\infty G_p(t)dt$  and the total viscosity is given by  $\eta = \eta_{p=1} + \dots + \eta_{p=N-1}$ . For chain lengths of  $N = 10$  and  $N = 20$  the integral of the stress correlation function is estimated from all the Rouse modes and for chains of  $N = 50$  and  $N = 100$  only the first ten modes were considered. The contribution of the eleventh mode for  $N \geq 50$  was found to be less than 1% of the contribution of the first mode. The contribution of the non polymeric stress on very short time scales was neglected. This leads to an underestimate of the viscosity on the order of 20% in the unentangled regime, and this contribution is negligible ( $< 1\%$ ) for longer chains of  $N \sim 100$ . The average local integrated value of  $G_{local}$  is shown in fig. 5.7. For chains of length  $N = 100$ , the grafting induces an increase in the integrated stress relaxation function in a range of around  $2R_G$  from the wall, as could be expected from the increase in the relaxation times, due to the increased entanglement density. A smaller increase in a layer of  $R_G$  is observed for the chains around the entanglement threshold ( $N = 50$ ). For unentangled melts, there is essentially no difference between the results with and without grafted chains.

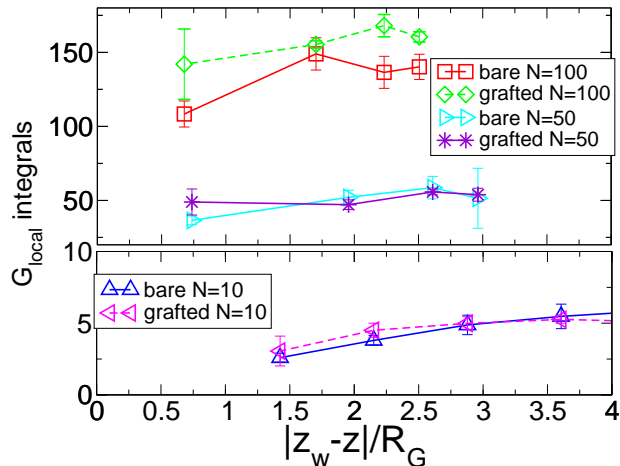


Figure 5.7: Local integral of  $G(t)$  for the different systems. The values are calculated as the mean of the three components  $xy$ ,  $xz$  and  $yz$  of the stress correlation function integral and error bars indicate the dispersion around the mean value.

### 5.3 Primitive Path Analysis of the Wall Melt Interface

In order to interpret the slowing down in the dynamics for entangled systems in the presence of grafted chains, we perform a local primitive path analysis following the algorithm discussed in ref. [70]. Starting from independent initial states separated by more than a chain relaxation time, the chain ends are kept fixed, while the intra chain pair interactions are switched off and the equilibrium bond length is reduced to zero while increasing the bond tension to  $k = 100\varepsilon/\sigma^2$ . Several parameters have to be carefully monitored for a correct primitive path quench. The main concern with this kind of simulation is to ensure the non crossability of the polymer chains during the relaxation. There are two ways in which a chain can cross another: due to a stretched bond or due to large monomer displacement for a large force and large time step. The setup for chain crossing is schematised in fig. 5.8.

For the LJ-FENE polymer model the critical value for the bond length is  $b_{trans} \approx 1.29\sigma$  [70]. To prevent this kind of situation, during the bond force calculation the code checks the bond length and the simulation is interrupted whenever a single bond stretches further than  $1.2\sigma$ . Even if the bonds are short enough, one can imagine that due to the high tension in the chain large accelerations can result and a chain could hop in a single time step on the other side of a neighboring chain, before “feeling” the repulsive potential. We prevent this from happening in the simulation in two ways. First, the

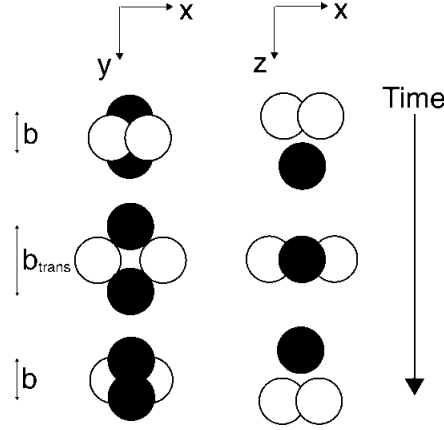


Figure 5.8: Schematic representation of PPA chain crossing. This can only take place for  $b_{trans} > 1.29\sigma$

time step is decreased and second we impose a very low temperature. In fact in the first stages of the primitive path quench the velocities are rescaled every single time step to give a temperature  $T = 0.001$ . This is limiting the maximum velocity of the monomers. In the same time, the time step is reduced to  $dt = 0.0025\tau$ : first to ensure the correct calculation of the bonds having now higher tension and second to limit the maximum displacement of a monomer within a time step. With these parameters a monomer has to have a velocity more than a thousand times higher than the thermal velocity in order to achieve a displacement of  $0.1\sigma$  in a time step.

In the systems with grafted chains the grafting bonds are maintained, the primitive path quench is applied to all the chains and the parameters of the primitive paths are measured for the free chains only as in the previous section.

We measure locally, as a function of the distance to the surface, the length of the primitive paths ( $L_{pp}$ ). If no entanglements exist between the chains the length of their primitive paths should be equal or very close to their end-to-end distance. The presence of entanglements leads to primitive paths longer than the end-to-end distance with a typical Kuhn length  $a_{pp} = \langle R^2 \rangle / L_{pp}$  and an average bond length  $b_{pp} = L_{pp} / N$ , which are related to the entanglement length [7]. We can define the number of monomers in straight primitive path segments by:

$$N_{pp}(N) = \frac{a_{pp}}{b_{pp}} = \frac{N \langle R^2 \rangle}{L_{pp}^2} \quad (5.7)$$

For short chains with no entanglements at all, as their primitive path length equals their end to end distance, equation 5.7 gives  $N_{pp} = N$ . When the

chain length becomes comparable to the entanglement length we are in a transition state (around one entanglement per chain) and the result of 5.7 is  $N_{pp} < N_e$ , smaller than the real value of the entanglement length. For longer chains ( $N > 2N_e$ ) with several entanglements per chain we have  $N_{pp}(N) = N_e$ . The statistical determination of  $N_e$  via equation 5.7 is already accurate and the result no longer depends on the chain length. The average number of entanglements per chain is  $\frac{L_{pp}}{a_{pp}} - 1$ . For chain lengths of 10 and 20 the primitive path analysis shows that we are in the unentangled regime as expected (with 0.1 entanglements per chain for  $N = 20$ ). For  $N = 50$  the melt is closer but still under the entanglement threshold with 0.5 entanglements per chain. For a chain length of 100 there are 1.1 entanglements per chain, the system is weakly entangled and for  $N = 200$  we measure on average 2.2 entanglements per chain. As expected in the unentangled case (fig. 5.9), the behavior in terms of primitive paths of the free chains in the system with and without grafted chains is identical. There is a slight decrease of the primitive path length close to the surface that is related to the decrease in the dimensions of chains lying flat on the surface. A noticeable difference is seen in the entangled case where the ratio  $L_{pp}/R_{ee}$  becomes larger for the free chains near the surface bearing tethered chains, while it decreases with respect to the bulk value for the bare wall system.

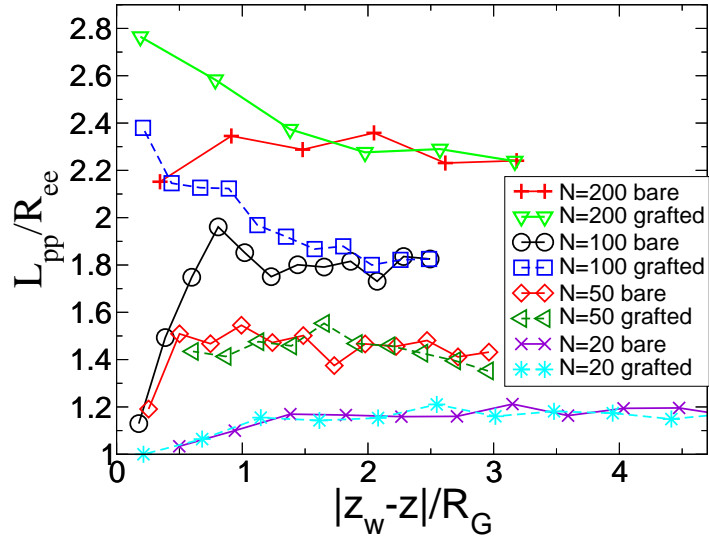


Figure 5.9: Local ratio of the primitive path length to the end-to-end chain distance in the different systems. This ratio for a given chain is proportional to its number of entanglements.

Measuring separately the primitive path length and the end-to-end distance in the systems of  $N = 100, 200$  (see fig. 5.10,5.11) we see that in the

presence of grafted chains on the surface the length of the primitive paths of the free chains remains essentially constant throughout the boundary layer, while it decreases in the presence of a bare wall. At the same time there is a slightly more pronounced decrease in the end-to-end distance for the system with grafted chains as discussed previously (fig. 4.5, 5.11). The grafted chains, being on average more extended than the free chains provide more entanglements in the plane parallel to the wall for the chains close to the interface, thus keeping their path length constant regardless of the fact that the perpendicular size of the chains diminishes leading to less inter-penetration in the  $z$  direction. In the case of a bare surface the decrease in the chains  $R_G$  results in less inter-penetration diminishing the primitive paths.

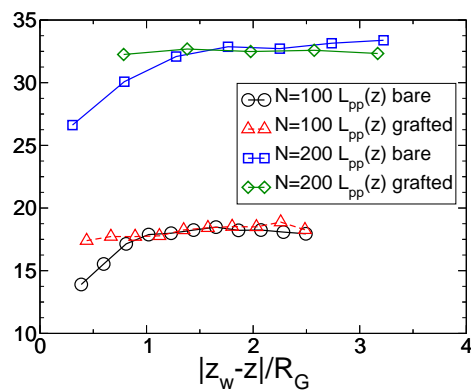


Figure 5.10: Local primitive path length for  $N = 100$  and  $200$ .

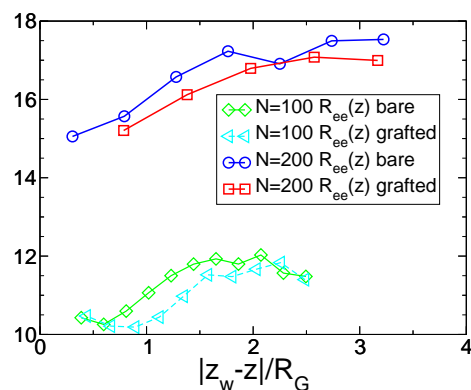


Figure 5.11: Local end-to-end distance for  $N = 100$  and  $200$ .

The additional entanglements due to the grafted chains can be interpreted in terms of local reduction of the entanglement length (or, equivalently increase in the entanglement density) as shown in fig. 5.12 and fig.

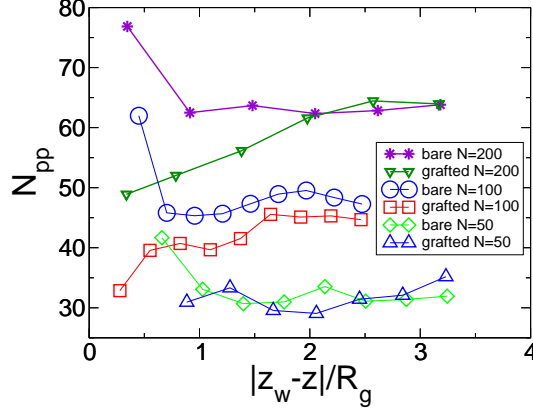


Figure 5.12: Local length of straight primitive path segments for the systems of  $N = 100$  and  $N = 200$ .  $N_{pp}(z)$  was calculated from the simulation data using equation 5.7. For  $N = 200$  the bulk value is equal to the entanglement length for the bead spring model at melt densities for flexible chains. [7]

5.13. The bulk entanglement length found for  $N = 200$  ( $N_e \approx 63$ ) is in agreement with the result of reference [7]. In the case of  $N < 200$  the numerical value of the bulk  $N_{pp}$  is lower than the  $N_e$  value for the melt as there are on average less than 2 entanglements per chain. The relative variation in  $N_{pp}$  is still meaningful and corresponds to a general trend in the entanglement density. To verify this assumption, we measure the local entanglement densities (entanglements per monomer) in the studied systems, defined as  $(L_{pp}(z)/a_{pp}(z) - 1)/N$ . The results are shown in fig. 5.13, confirming that the variation in  $N_{pp}$  leads to an increase in the entanglement density.

In a region that extends about one  $R_G$  from the surface, there is a depletion of entanglements for a bare repulsive wall, as qualitatively predicted in reference [68]. A similar behavior was also observed in ref. [74]. This effect was associated with smaller chain size in the  $z$  direction. It can be also understood knowing that chains in the immediate vicinity of the wall only have neighboring chains on one side and no chains to entangle with on the other side, so they have a smaller total number of entanglements. On the other hand, in presence of grafted chains the free chains near the surface do not feel its presence as far as entanglements are concerned as they still entangle with the chains grafted on the surface keeping a constant primitive path length. Moreover, as the parallel dimensions of the free chains are reduced, we end up with an interfacial region with higher density of entanglements. This difference in entanglement density explains the slowing down in the dynamics of the entangled modes. Moreover, a quantitative prediction can be established. Knowing from reptation theory that the relaxation

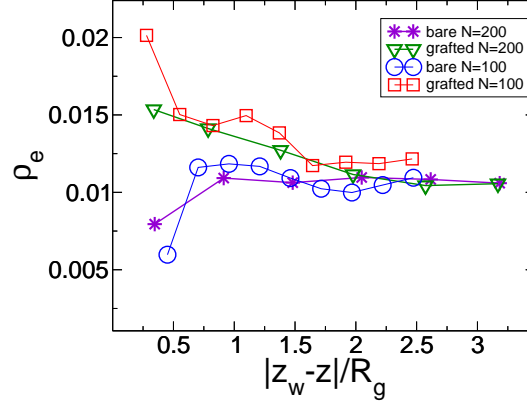


Figure 5.13: Local number of entanglements per monomer in the  $N = 100$  and  $N = 200$  systems. An increase in the entanglement density is seen for grafted wall, consistent with the measured variation in  $N_{pp}$  and  $N_e$ . A similar behavior is observed for  $N = 50$ .

of an entangled chain is proportional to  $N \times \left(\frac{N}{N_e}\right)^2$ , the ratio between the relaxation times of two systems of equal chain length should be equal to the inverse square ratio of the entanglement lengths in the two cases, i.e.

$$\frac{\tau_R^{grafted}}{\tau_R^{bare}} = \left(\frac{N_e^{bare}}{N_e^{grafted}}\right)^2 \quad (5.8)$$

This relation provides a way to predict dynamics from a static equilibrium quantity in the melt. It is reasonably well verified in the interfacial layer of our  $N = 100$  system, even if the melt is only weakly entangled at this chain length (see fig. 5.14). This argument can be pushed further to predict the local viscosity in the interfacial layer in the reptation regime:

$$\frac{\eta^{grafted}}{\eta^{bare}} = \left(\frac{N_e^{bare}}{N_e^{grafted}}\right)^3 \quad (5.9)$$

This prediction is no longer valid for chain lengths as short as  $N = 100$  as we have only one entangled mode (too few entanglements per chain), but should be verified for strongly entangled melts where the mechanical behavior is entirely dictated by the entanglements.

## 5.4 Entanglements in polymer nanocomposites

In this section we will discuss the variation of the entanglement density in an entangled polymer melt with spherical filler particles. The system under

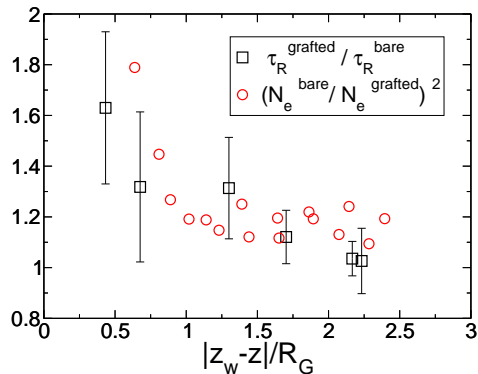


Figure 5.14: Comparison between the ratio of the local relaxation times (left term in eq. 5.8) and the inverse square ratio of the local entanglement lengths (right term in eq. 5.8) of the  $N = 100$  systems with and without grafted chains.

study was presented earlier (81 chains of  $N = 500$  and 10% (42 fillers) and 20% (84 fillers) of filler volume fraction). In these systems where  $N = 500$  we have on average in all cases at least 8 entanglements per chain.

In order to study the effect of the fillers on entanglements we follow several distinct setups for the primitive path quench. In the first setup the fillers are taken out of the melt before the quench. This study probes for an effect of the fillers presence on the equilibrium conformations in the polymer matrix without the the actual influence of the filler-melt interface. Next, we study the influence of the filler polymer interaction and the filler mobility on the primitive paths. In the second setup fillers are kept still in the melt and the chains are allowed to relax around the fixed fillers with attractive filler-polymer interactions identical to those during equilibration ( $\varepsilon = 3$ ,  $r_{cut} = 2.5\sigma$ ), with strongly attractive filler-polymer interactions ( $\varepsilon = 10$ ,  $r_{cut} = 2.5\sigma$ ) and also with purely repulsive interactions ( $\varepsilon = 3$ ,  $r_{cut} = 1.12\sigma$ ). Strong attraction increases the energy cost for a desorption during quench, transforming the fillers into more solid bridges, whereas repulsion allows the adsorbed chain segments to slip away from the filler surface. In the last set of simulations fillers are allowed to move freely during the analysis and again the cases of filler polymer repulsion and attraction are separately examined. Filler mobility during quench allows the fillers to take part in the constraint release of the primitive paths.

In the case of mobile fillers we studied the influence of excluded volume interactions between the fillers. We performed runs with fillers allowed to cross each other or having repulsive interactions. This parameter was found to have negligible effect on the primitive paths at the relatively low filler volume fractions we study. The primitive paths parameters measured in the

filled melt are compared to the results for a pure polymer melt (equilibrated at the same pressure).

In order to calculate the entanglement length the only quantity we need to extract from the PP quench is the bond length  $b_{pp}$ . The mean square end to end distance  $\langle R^2 \rangle$  is measured in an equilibrium simulation and the entanglement length is calculated by simplifying equation 5.7 using the expression:

$$N_e = \frac{\langle R^2 \rangle}{(N-1)b_{pp}} \quad (5.10)$$

The primitive path analysis in the pure polymer indicates an entanglement length  $N_e \approx 53$ . This value is again in agreement with the results in ref. [7], given that our system is at higher density and the equilibrium bond length is slightly larger.

We report a reduction of the entanglement length (or, equivalently increase in the entanglement density) in the systems with fillers (fig. 5.15).

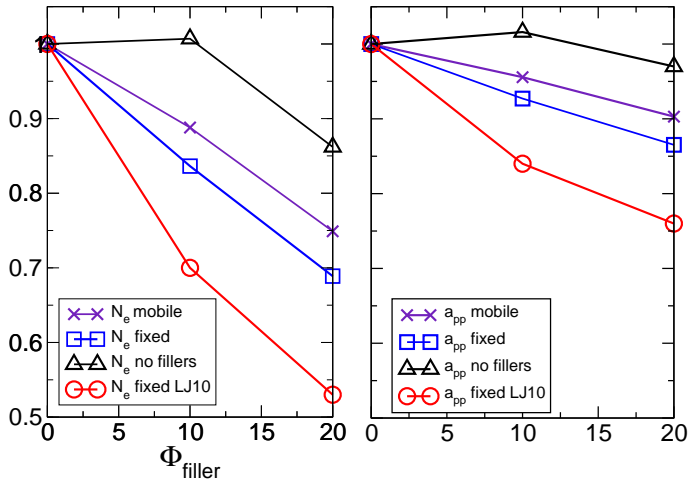


Figure 5.15: Entanglement length and tube diameter in the nanocomposites normalized by the value for the pure polymer. Results from the different quench set-ups are shown: PPA without fillers, mobile attractive fillers, fixed attractive fillers and fixed strongly attractive fillers.

In the case of repulsive interactions and mobile fillers the results superimpose with those from the PPA without fillers. A quench without fillers leads to no  $N_e$  variation for  $\Phi = 10\%$  and a small reduction ( $\sim 15\%$ ) for  $\Phi = 20\%$ . The reduction for  $\Phi = 20$  can be explained via the increase in the mean square end to end distance as discussed below. In view of this result we believe that the global chain conformations are not significantly affected

by the presence of the fillers, in the sense that when fillers are taken out the melt recovers an entanglement network close to the one of a pure polymer.

The observed  $N_e$  reduction is clearly related to the presence of the filler polymer interface and to the attractive filler-polymer interaction. This reduction is more pronounced in the case of fixed fillers. The increase in the entanglement density is in all cases higher in the samples with higher filler volume fraction.

In the following we discuss the results presented here in order to explain the origin of the  $N_e$  variation in the composite.

### 5.4.1 Effect of fillers on chain conformations

We observe that the overall chain dimensions remain only slightly perturbed compared to the reference pure system. The mean square end to end vector  $\langle R^2 \rangle$  is increased by 3% for a filler volume fraction of  $\Phi = 10\%$  and 8% for  $\Phi = 20\%$ . This result explains to a certain extent the PPA results without fillers - no difference for  $\Phi = 10$  and  $N_e$  reduction on the order of 15% in the case of  $\Phi = 20$ . An increase of the chain dimensions seems reasonable for sub-chain size fillers. Slight reduction of the chain size in MC simulations have been reported in the past for neutral interactions and fillers considerably larger than the chains  $R_G$  [75, 76]. In our system no global chain confinement is present due to the fillers.

On length scales smaller than the end to end distance we observe more noticeable differences in the chain conformations. The presence of the fillers surface leads to certain alignment and structuration in the surrounding chains thus effectively increasing the persistence length on the length scale of the inclusion. To study this effect it is useful to define the Kuhn length-like quantity [77]:

$$b_k(n) = \frac{\langle R^2(n) \rangle}{nb_0} \quad (5.11)$$

where  $n$  is the number of monomers over which the mean square distance is calculated. Results can be seen on figure 5.16. The change in the microscopic persistence length leads in principle to a modified packing length in a pure melt and can have an impact on the entanglement length as was discussed in section 2.4.

Better inter-penetration of neighboring chains promoted by higher persistence length causes a decrease in  $N_e$  for a pure polymer melt. This is equivalent to a decrease of the packing length  $p$  defined by equation 2.31. Still, calculating the packing length in a confined or an inhomogeneous system is not straightforward. To estimate this quantity we have to first define the volume per monomer and the effective bond length of the chains (or equivalently, the Kuhn segment length or the persistence length). Here we calculate the volume per monomer as the total volume occupied only by the

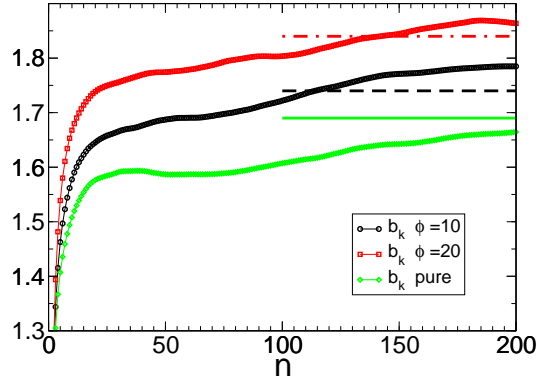


Figure 5.16: Kuhn length calculated over chain segments of length  $n$  as a function of  $n$ . The straight lines show the terminal values for  $n = 500$ .

polymer in the composite, divided by the total number of monomers:

$$v_0 = \frac{V - V_f}{N \times N_{ch}} \quad (5.12)$$

where  $V$  is the simulation box volume,  $V_f$  is the volume of the fillers,  $N$  the chain length and  $N_{ch}$  - the number of chains in the system. The effective bond length was calculated from the terminal value of the Kuhn length on fig. 5.16. The resulting prediction for the entanglement length and the tube diameter is shown on fig. 5.17. We note that an even larger effect can be obtained if we estimate the effective bond length at the scale of around 50 monomers, where the filler influence is bigger. We see that the estimation based on the packing argument is consistent with the decrease in  $N_e$  and  $a_{pp}$  measured by PPA. This result will be further discussed in the following sections.

#### 5.4.2 Influence of fillers on primitive paths

Given the presence of a large interfacial area in the composite system, next we analyze in finer detail the PPA results. Knowing that the quantity resulting from the quench is the bond length we measure its distribution in order to understand the structure of the primitive path network. Results for the PPA  $b_{pp}$  in absence of fillers are shown in fig. 5.18.

As stated earlier, we see that for  $\Phi = 10\%$  and quench without fillers the effect on the PPA is close to negligible and there is an increase in  $b_{pp}$  for  $\Phi = 20\%$ .

The nature of the bond length distributions in the filled melt changes qualitatively in presence of attractive fillers (fig. 5.19, 5.20, 5.21).

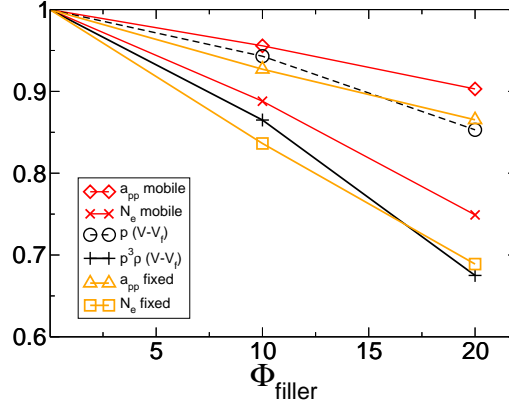


Figure 5.17: Comparison of the entanglement length and the tube diameter normalized by the bulk values with the prediction from the packing length, taking the volume per monomer from equation 5.12.

There are two distinct populations of bond lengths - highly extended and short. To understand this result we need a more precise view of the typical conformations of the primitive paths with respect to the polymer filler interface. Inspired by the analysis in section 4.3, we study the primitive paths in terms of filler adsorption. An adsorbed monomer of the primitive chain is defined as being closer to the filler than the first minimum of the measured  $g(r)$  function after quench. We can thus define several types of segments in a primitive chain: adsorbed (where monomers are within  $3.16\sigma$  from the center of the filler), bridge and loop segments (starting and ending with an adsorbed monomer) and tail segments (beginning or ending with a chain end). We measured separately the PP bond lengths of adsorbed segments and segments belonging to bridges and loops. Measurements show that bonds belonging to bridge segments are on average 2.5 times longer than the adsorbed bonds (table 5.1, fig. 5.22). More details about the PP conformations are given in table 5.1.

The PP quench increases in all cases the number of monomers on the surface of the fillers, there are around 8 times more adsorbed monomers after quench for the  $\Phi = 10$  systems and 4 to 5 times more for  $\Phi = 20$  (table 5.1). This result is expected: as during the quench excluded volume interactions between neighboring monomers are switched off, monomer adsorption on the filler surface is easier, not limited by intrachain excluded volume effects. Knowing that the surface is attractive, primitive paths have a tendency to maximize their number of adsorbed monomers as long as this does not involve an important elongation, penalized by the large bond tension during the

System $\Phi = 10$	<i>eq</i>	<i>PP fix</i>	<i>PP mob</i>	<i>PP fix10</i>
Loops per chain	10.8	1.7	1.7	2.1
Bridges per chain	4.8	4.5	4.7	5.2
Correlation after quench		0.39	0.21	0.64
Fillers per chain	5.1	4.9	5.5	5.5
Adsorbed monomers per chain	27	195	233	306
$a_{pp}$		8.79 $\sigma$	9.06 $\sigma$	7.96 $\sigma$
$N_e$		44.3	47.1	37.1
$b_{pp}$		0.199 $\sigma$	0.193 $\sigma$	0.217 $\sigma$
adsorbed segments $b_{pp}$		0.117 $\sigma$	0.093 $\sigma$	0.105 $\sigma$
bridge segments $b_{pp}$		0.243 $\sigma$	0.286 $\sigma$	0.392 $\sigma$
loop segments $b_{pp}$		0.153 $\sigma$	0.177 $\sigma$	0.300 $\sigma$
$L_{pp}$		99.3 $\sigma$	96.2 $\sigma$	108.4 $\sigma$
fraction adsorbed $L_{pp}$		23%	22%	29%
System $\Phi = 20$	<i>eq</i>	<i>PP fix</i>	<i>PP mob</i>	<i>PP fix10</i>
Loops per chain	20.3	2.3	2.0	3.2
Bridges per chain	11.5	8.5	9.6	10.6
Correlation after quench		0.27	0.13	0.49
Fillers per chain	10.4	8.7	10.2	10.1
Adsorbed monomers per chain	53	207	257	307
$a_{pp}$		8.20 $\sigma$	8.53 $\sigma$	7.20 $\sigma$
$N_e$		36.5	39.7	28.1
$b_{pp}$		0.225 $\sigma$	0.216 $\sigma$	0.256 $\sigma$
adsorbed segments $b_{pp}$		0.165 $\sigma$	0.126 $\sigma$	0.168 $\sigma$
bridge segments $b_{pp}$		0.273 $\sigma$	0.325 $\sigma$	0.406 $\sigma$
loop segments $b_{pp}$		0.244 $\sigma$	0.266 $\sigma$	0.388 $\sigma$
$L_{pp}$		112.2 $\sigma$	107.6 $\sigma$	127.7 $\sigma$
fraction adsorbed $L_{pp}$		30%	30%	40%

Table 5.1: Average values for primitive paths and equilibrium conformations. Different columns contain values for different quench methods: *eq* - equilibrium, unquenched melt; *PP fix* - quench with fixed particles and attractive interaction (same intensity as in equilibrium,  $\varepsilon = 3$ ); *PP mob* - quench with mobile particles and attractive interaction as in equilibrium; *PP fix10* - quench with fixed particles and strongly attractive interaction ( $\varepsilon = 10$ ).

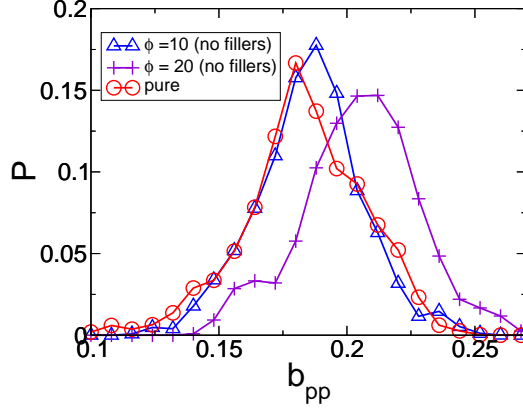


Figure 5.18: Distribution of the primitive path bond lengths for pure polymer and composites after quench in absence of fillers.

quench. The energy of a primitive chain is given by:

$$E = \sum_2^N E_{fene}(|\vec{r}_i - \vec{r}_{i-1}|) + \sum_{j \in \text{fillers}} \sum_i E_{LJ}(|\vec{r}_i - \vec{r}_j|) \quad (5.13)$$

We can simplify this expression by approximating the *FENE* potential by a harmonic spring and by simplifying the Lennard Jones potential considering that a particle has an energy gain of  $\varepsilon$  when it is adsorbed and does not feel the presence of the fillers otherwise. We can also assume that the primitive paths bond length has a constant value in the adsorbed layer and in the unadsorbed segments (bridge, loop and tail segments). The path energy becomes:

$$E(b_b, b_a, N_a) = (N - N_a) \frac{k}{2} b_b^2 + N_a \frac{k}{2} b_a^2 - N_a \varepsilon \quad (5.14)$$

where  $b_b$  is the primitive path bond length of the bridge, loop and tail segments,  $b_a$  is the bond length of the adsorbed segments and  $N_a$  is the number of adsorbed monomers. The primitive path conformations after quench are given by the minimum of this energy for every chain (with a certain number of topological constraints - the entanglements). Deriving this expression with respect to  $N_a$  and setting the derivative to zero gives the relation existing between the two distinct bond lengths:

$$\frac{k}{2} b_b^2 = \varepsilon + \frac{k}{2} b_a^2 \quad (5.15)$$

and from here the bridge/loop segments bond length is given by

$$b_b = \sqrt{\frac{2\varepsilon}{k} + b_a^2} \quad (5.16)$$

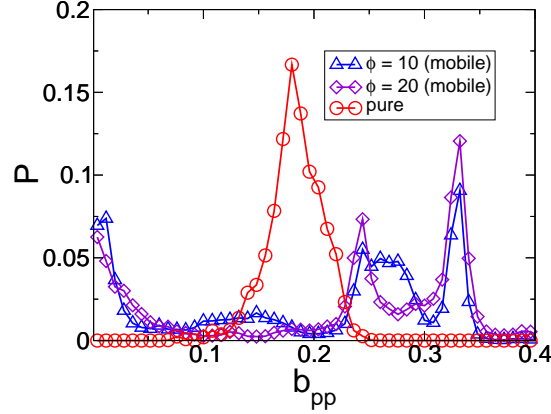


Figure 5.19: Distribution of the primitive path bond lengths for pure polymer and composites after quench with mobile attractive fillers.

Taking  $k = 100$  and  $\varepsilon$  as the Lennard Jones potential intensity, this relation is reasonably well verified by the results obtained from the PPA (see table 5.1). The last equation explains the fact that bridge segments are more extended than adsorbed ones. If  $b_b$  grows too large the extended spring in the unadsorbed segment will pull out monomers from the adsorbed layer. On the other hand if  $b_b$  is too small the segment will be adsorbed by the surface as it won't be able to resist the surface attraction added to the spring force from the adsorbed monomers. Thus equation 5.15 simply states that, in order for the chain to be stable, unadsorbed segments have to exactly balance the force from adsorbed segments.

### 5.4.3 Predicting the entanglement length

Next we will try to calculate the variation in  $N_e$  induced by the presence of the attractive fillers. The idea is that the presence of fillers creates polymer bridges that are seen by the chains as new entanglements to be added to the already existing ones in the pure polymer. For instance, we measured the average number of entanglements per chain given by:

$$n_{ent} = \frac{N}{N_e} - 1 \quad (5.17)$$

We can consider that the bridges between fillers a chain has ( $n_{br}$ ) contribute as entanglements as long as they are not destroyed during the PP quench. We assume that the chain acquires  $\alpha n_{br}$  new entanglements ( $0 \leq \alpha \leq 1$ , see below for a discussion of the appropriate choice of  $\alpha$ ) that are due to bridges.

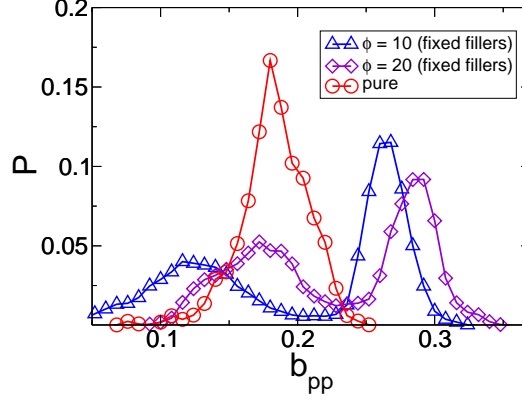


Figure 5.20: Distribution of the primitive path bond lengths for pure polymer and composites after quench with fixed attractive fillers.

So the number of entanglements per chain in the nanocomposite becomes:

$$n_{ent}^{nc} = n_{ent}^{pure} + \alpha n_{br} = \frac{N}{N_e^{nc}} - 1 \quad (5.18)$$

where  $n_{ent}^{pure}$  is the number of entanglements per chain in the unfilled melt and  $N_e^{nc}$  is the effective entanglement length measured from the PPA of the nanocomposite. In equation 5.18 we assume that the entanglements present in the pure polymer system persist in the nanocomposite and the bridges add independently their contribution. We calculate the number of bridges per chain by counting the number of fillers present in a typical volume spanned by the chain (a sphere of radius  $R_G$ ). The number of fillers in a sphere of radius  $R_G$  is given by  $\rho_f \times 4/3\pi R_G^3 = \Phi \times (R_G/r_f)^3$ . Taking  $r_f = 3.12\sigma$  and the measured bulk  $R_G$  of the chains, this estimate predicts 5.3 fillers per chain for the  $\Phi = 10$  system and 10.6 for  $\Phi = 20$ . These values are in good agreement with the simulation data as can be seen in table 5.1. Rewriting equation 5.18 using this expression gives an estimate for the effective entanglement length in the nanocomposite:

$$\frac{N}{N_e^{pure}} - 1 + \alpha(\Phi(R_G/r_f)^3 - 1) = \frac{N}{N_e^{nc}} - 1 \quad (5.19)$$

$$N_e^{nc} = N / [N_e^{pure} + \alpha(\Phi(R_G/r_f)^3 - 1)] \quad (5.20)$$

In order to compare this result to the simulation data, we need to determine the value of  $\alpha$ . It is reasonable to believe that during the quench with strong particle monomer attraction  $\varepsilon = 10$ , we have  $\alpha = 1$  (there is no significant bridge loss during the quench). To verify this assumption we calculated

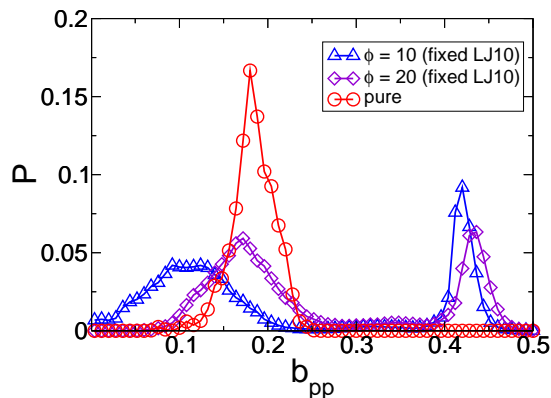


Figure 5.21: Distribution of the primitive path bond lengths for pure polymer and composites after quench with fixed strongly attractive (LJ10) fillers.

a per chain quantity that can be described as adsorption correlation after quench: it is defined as the number of adsorbed monomers in the primitive chain that remain adsorbed and adsorbed to the same filler as they were in the original chain, divided by the total number of adsorbed monomers of the original chain. If this quantity equals one, every adsorbed monomer of the original chain remained adsorbed to the same filler and zero means that every originally adsorbed monomer is either desorbed or adsorbed to a different filler in the primitive chain. The calculated correlation is shown in table 5.1, in both systems the primitive paths obtained with the quench with fixed particles and  $\varepsilon = 10$  show the largest degree of correlation to the original adsorption pattern of the chains (see fig. 5.23).

It is important to note that, even if the number of fillers and bridges per chain does not vary much for the other quenches, there is a more important change in the conformation, resulting in keeping only the moderately extended bridges and leading to shorter primitive paths: this situation is illustrated on figure 5.23.

The  $N_e^{nc}$  estimate from equation 5.20 with  $\alpha = 1$  is in agreement with the PPA results for  $\varepsilon = 10$  (table 5.1), predicting  $N_e^{nc} \approx 36.5$  for  $\Phi = 10$  and  $N_e^{nc} \approx 26.4$  for  $\Phi = 20$ . We can conclude that the simple expression given in 5.20 can be used to estimate the  $N_e$  reduction in the filled polymer melt.

#### 5.4.4 Conclusion

We used two different ways to predict the entanglement length in the nanocomposite from equilibrium properties. The observed decrease can be explained by packing arguments: the packing length in the composite decreases as there is less space per monomer while the effective bond length increases

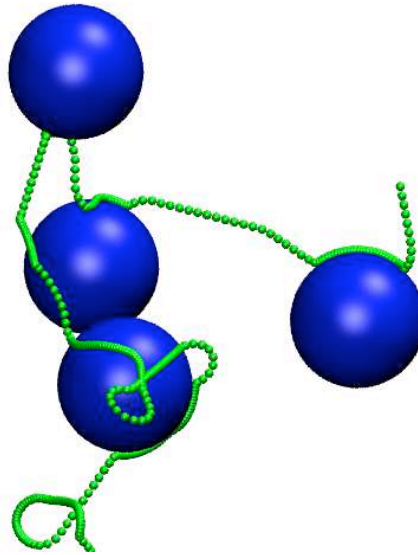


Figure 5.22: Snapshot of the primitive path of a chain in presence of filler particles (fixed fillers, LJ10). Adsorbed segments are shorter than bridge segments.

(as chain dimensions are larger or as large as in the pure polymer). On the other hand we can explain the  $N_e$  variation by taking into account the inter-filler bridges in the composite. When considering every bridge as new entanglement a large decrease in  $N_e$  can be obtained, fitting the PPA results with strongly attractive fixed filler particles. The two predictions are essentially based on the same idea. The packing length reduction means that the nanoparticles bring chains closer together allowing the formation of entanglements “through” the fillers. In the bridge-based prediction fillers are considered to form links between chains, making them interact with each other in the same way an entanglement would. The idea of the entanglement forming fillers requires in both cases the presence of filler polymer attraction.

In the case of repulsion the PPA results are similar to the quench results in absence of fillers. In this setup, there is no  $N_e$  variation for  $\Phi = 10\%$  and a reduction of around 10-15% for  $\Phi = 20\%$  that we relate to the increase in chain dimensions at equilibrium in this system.

Recent experimental work has suggested that the entanglement network remains unmodified by sub-chain sized filler particles (ideal organic nanoparticles) having neutral interaction with the polymer [13, 78]. On the other hand, experiments with particles strongly interacting with the polymer matrix showed a large increase in the viscosity for entangled melts [14]. This effect was attributed to the possible formation of polymer-filler network.

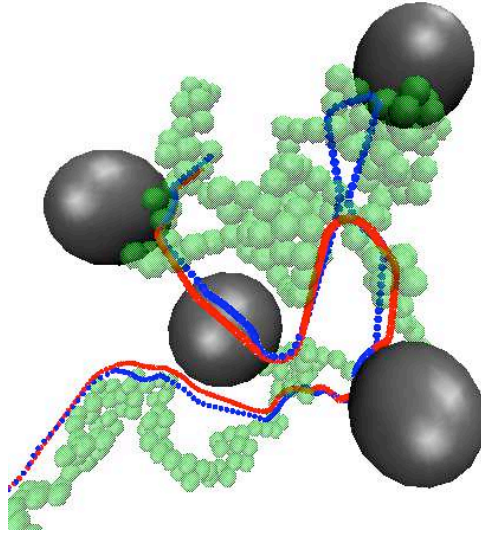


Figure 5.23: Snapshot of a chain along with its primitive paths after a quench with  $\varepsilon = 3$  (red) and  $\varepsilon = 10$  (blue). The  $\varepsilon = 10$  quench preserves most of the original adsorptions of the chain.

These experimental findings are in qualitative agreement with our predictions.

The choice of the parameter  $\alpha$  in our model, as well as the type of PP quench to be applied when a particular physical system is investigated, need to be further discussed. Filler mobility in the entanglement network of the polymer plays undoubtedly a major role in the reinforcement. Light, mobile fillers diffusing faster than the reptation time of the chains will undoubtedly have smaller reinforcing effect or even accelerate disentanglement and participate in constraint release [78]. Heavier, more compact fillers (such as silica, or grafted fillers), can on the contrary anchor entanglements. After the PP quench, as the achieved configuration is an energy minimum, the entanglement length does not depend on filler mass. Thus experimental results for heavy particles composites should be better modeled with fixed fillers quench whereas particles with typical diffusion time faster than  $\tau_d$  would correspond to a mobile filler quench. The parameter  $\alpha$  should depend on the surface chemistry of the inclusions for heavy particles and for light particles its value has to be adapted to take into account an eventual constraint release occurring due to the high filler mobility.

## 5.5 Stress relaxation and dynamics in polymer nanocomposites

Next we study the dynamical behavior of the filled melt compared to the bulk system. A variation in the entanglement density between the pure and filled systems is in principle reflected in the plateau modulus and therefore in the stress autocorrelation function of the systems. We explore here two distinct ways to obtain the  $G(t)$  function: step shear and equilibrium determination.

The first setup consists in applying a step shear to the system and monitoring the following stress decay over time. Starting from a fully relaxed equilibrium configuration we impose a deformation  $\varepsilon_{sh}$  to all the atoms:

$$x_{new} = u(x, y) = x(1 + \varepsilon_{sh}y) \quad (5.21)$$

the corresponding shear rate is given by

$$\frac{\partial u}{\partial y} = \varepsilon_{sh}\delta(t) \quad (5.22)$$

the resulting stress is then [31]

$$\begin{aligned} \sigma_{xy}(t) &= \int_{-\infty}^t G(t-t')\dot{u}(t')dt' \\ &= \varepsilon_{sh}G(t) \end{aligned} \quad (5.23)$$

Where  $G(t)$  is the stress correlation function. For entangled melts we know that in theory this function has an initial decay and for times  $\tau_e < t < \tau_d$  (where  $\tau_e$  is the entanglement time and  $\tau_d$  is the reptation time) shows a plateau (fig. 2.6). Its value is given by the plateau modulus [31] (equation 2.36).

Thus the measurement of the stress relaxation after a step shear provides a way to estimate some characteristics of the primitive paths. In practice due to stress fluctuations the stress correlation function is difficult to accurately obtain using the global stress as was discussed in chapter 3. Here we measure the stress using the Rouse modes of the chains following equation 2.26.

$$\frac{\sigma_{xy}^p(t)V_p}{\sigma_{xy}^{nc}(t)V_{nc}} = \frac{\sum \frac{\langle X_{px}^p(t)X_{py}^p(t) \rangle}{\langle X_{px,p}^2 \rangle_{eq}}}{\sum \frac{\langle X_{px}^{nc}(t)X_{py}^{nc}(t) \rangle}{\langle X_{px,nc}^2 \rangle_{eq}}} \quad (5.24)$$

$$= \frac{G_p^0 V_p}{G_{nc}^0 V_{nc}} = \frac{N_e^{nc}}{N_e^p} \quad (5.25)$$

The measurement of this quantity in practice suffers from several drawbacks. First, the computational cost for this setup is very high. As we are

using Lees-Edwards boundary conditions due to the tilted box, the simulation has low parallel efficiency. Second, in order to obtain a measurable stress signal, the deformation applied to the simulation box has to be rather large because of the stress fluctuations. We performed 5 distinct simulations starting from independent equilibrated initial configurations for every system (pure,  $\Phi = 10\%$ ,  $\Phi = 20\%$ ), and for three distinct values of the deformation  $\varepsilon_{sh} = 5\%$ ,  $10\%$ ,  $20\%$ . Error bars were calculated from the dispersion of the signal from the simulations with identical parameters and different initial states. The resulting stress curves for  $\varepsilon_{sh} = 5\%$  have error bars considerably larger than the difference of the stress between the systems. For higher deformations non linear effects (Payne effect) are expected at the particle volume fractions we study. The Payne effect we observed between  $5\%$  and  $20\%$  of deformation was around  $30\%$  for  $\Phi = 20\%$ , but the initial drop for  $\varepsilon_{sh} < 5\%$  could not be estimated. Results for  $\varepsilon_{sh} = 10\%$  are shown on fig. 5.24.

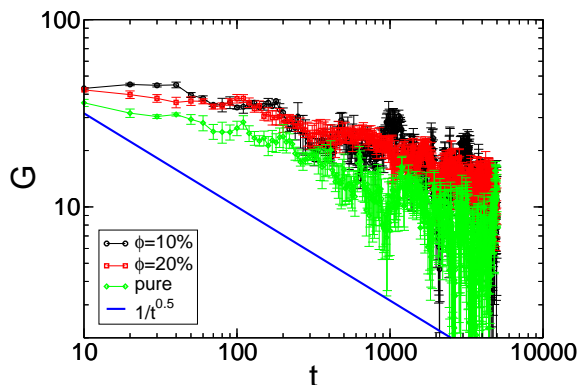


Figure 5.24: Stress correlation function calculated from equation 5.23 after step shear deformation of  $\varepsilon_{sh} = 10\%$ .

The stress was calculated from the first 50 modes of the chains. The curves follow approximately the  $1/\sqrt{t}$  power law predicted by theory. The noise in  $G(t)$  remains rather large and a plateau cannot be clearly distinguished. The values for  $\Phi = 10\%$  and  $\Phi = 20\%$  are on average  $38\%$  and  $43\%$  higher than the response of the pure system. A difference around  $10\%$  smaller was observed for a deformation of  $\varepsilon_{sh} = 20\%$ . The uncertainty in these values are very large, so we do not discuss them further.

The second method for obtaining the stress correlation function is the equilibrium based Rouse modes method discussed in section 3.3.2. We monitored the values of the first 60 Rouse modes of the chains in equilibrium. To obtain  $G(t)$  we performed averaging over chains, time origins and the three

off diagonal components of the stress tensor (see section 3.3.2 for details). The resulting functions are shown in fig. 5.25.

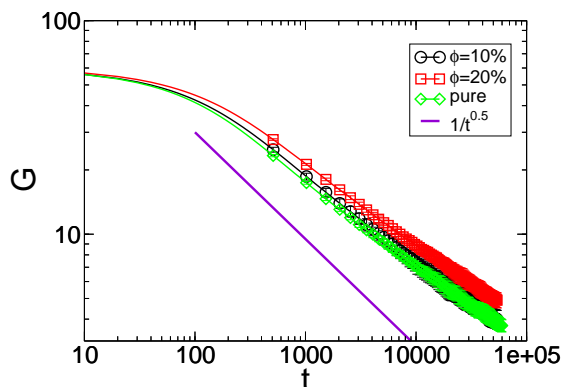


Figure 5.25: Stress correlation function calculated in the nanocomposite systems from the first 60 equilibrium Rouse modes. Only every 50th symbol of the curves is shown for clarity.

The simulation time in the three systems for this measurement was  $2 \times 10^5 \tau$ . The stress correlation does not show a plateau and follows a  $1/\sqrt{t}$  behavior. By measuring the relaxation of the individual Rouse modes we established that, within the simulated time span, the first mode stays more than 95% correlated to its initial value. Full relaxation allowing to extract a relaxation time only occurs for modes  $p > 20$  (see fig. 5.26).

From the measured Rouse times for modes  $p > 20$  we find a slowing down in dynamics of around 20% for  $\Phi = 10\%$  and around 50% for  $\Phi = 20\%$ . Knowing that these modes are associated with relaxation on sub- $N_e$  length scales, this increase in relaxation times has undoubtedly its origin in the increased monomeric friction in the filler/polymer interface. Even if it could be partly due to bridges, a relation to the entanglement length cannot be easily established. Due to the slowing down at the interface, the measured  $G(t)$  is roughly increased by about 8% and 18% for  $\Phi = 10\%$  and  $\Phi = 20\%$ .

From the results above we can conclude that, in order to extract an information relevant to the entanglement network from dynamics, the system has to be simulated for at least several disentanglement times, which, for the chain length considered in our study, is presently out of reach for molecular dynamics.

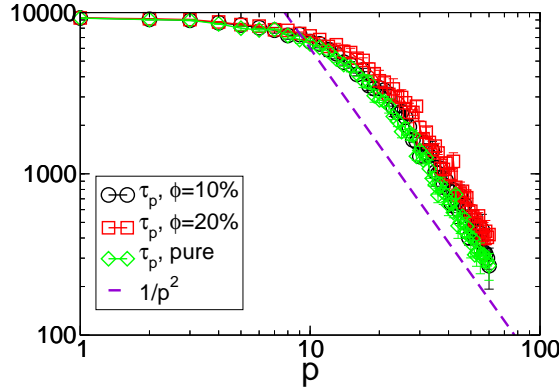


Figure 5.26: Calculated values of the Rouse times in equilibrium for the  $N = 500$  systems. The  $1/p^2$  behavior is followed by modes of roughly  $p > 20$ . The simulated time does not permit the determination of an accurate relaxation time for slower modes.

## 5.6 Discussion and conclusions

In this chapter we further extended our study to cover the melt properties in a wider zone covering the whole interface with different microscopic chemical nature of the wall, as well as for a filled melt. We examined the dynamic behavior for a polymer melt at the interface with a flat wall and a flat wall subject to surface treatment creating about 20% of chemisorbing sites on the surface. We find that the modifications in the dynamics due to the surface treatment depends on the level of entanglement of the melt. In the case of unentangled melts, the dynamics is accelerated compared to the bulk due to the repulsive surface. The grafted chains locally slow down the dynamics in the surface plane compared to systems without grafted chains, but the relaxation times are smaller than in the bulk and there is a local decrease in the integrated stress relaxation function as in the case of a bare wall. In the case of weakly entangled melts, the presence of the surface induces a decrease ( $\sim 20 - 40\%$ ) in the entanglement density in a range of about  $R_G$  from the surface. The presence of the grafted chains prevents this depletion of the entanglements and further reduces the entanglement length in the interfacial layer, in part due to the smaller chain dimensions. This leads to slower dynamics in the interfacial layer and a local increase of the relaxation times of the entangled modes near the surface. A summary of the dynamical behavior of the chains is given in fig. 5.27. The behavior of the relaxation times can be predicted by measuring the local entanglement length, following the expression given by reptation theory.

Our results on dynamics are obtained for chains that are only slightly

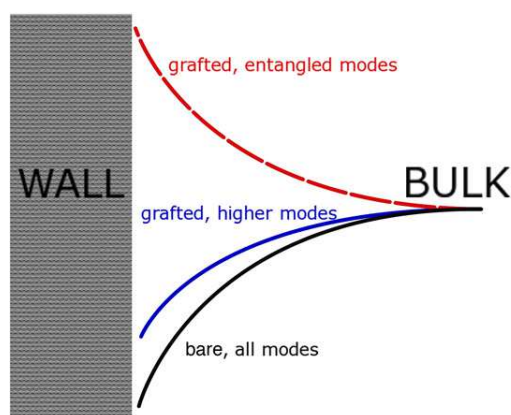


Figure 5.27: Schematic representation of the relative variation of the relaxation times of the modes of the polymer chains at the interface.

above the entanglement threshold but the primitive path analysis extends to chains further in the entangled regime. The results of the two methods are consistent and if a contribution from the grafted chains is added we can explain the observed moderate reinforcement in systems of  $T \geq 2T_g$  where there can be no formation of glassy bridges.

We expect that these conclusions would hold for highly entangled melts. For longer chains the extension of the region where entanglement effects are enhanced by the grafting will be larger. It is likely that the motion of the chains perpendicular to the interface will be slowed down as well within this region, as entanglements will also hinder this type of motion.

We note that the explanation of reinforcement by local variation of the entanglement length we proposed here is also relevant in a wider range of systems. We considered a surface with a certain number of infinitely attractive sites, but similar effects can be expected for a surface with a fraction of finitely attractive sites or a globally attractive surface. Thus the slowing down mediated by the adsorbed, slowest chains plays a role in the high temperature mechanical properties of nanocomposite polymer based materials.

Finally, we studied a model polymer nanocomposite with spherical fillers. We report that the presence of attractive nanofillers with subchain dimensions and volume fraction allowing bridging leads to an effective increase of the total entanglement density in the system. Fillers tend to act as reticulations, creating new effective entanglements between chains. The measured reduction of the entanglement length can be partly predicted by packing arguments and with a model taking into account the polymer bridges between fillers in the melt. This effect, different from the confinement effect near a grafted surface discussed above, should play a role in the mechanical properties of nanocomposites filled with small size attractive fillers.

## Chapter 6

# Heat transfer and thermal conductivity in nanofluids

### Contents

---

<b>6.1</b>	<b>Introduction</b>	<b>119</b>
<b>6.2</b>	<b>Simulation method</b>	<b>120</b>
<b>6.3</b>	<b>Modeling pump-probe experiments and determination of the interfacial resistance</b>	<b>124</b>
<b>6.4</b>	<b>Conductivity of nanofluids</b>	<b>129</b>
6.4.1	The Maxwell Garnett calculation	129
6.4.2	Single particle in a heat flow	132
6.4.3	Study of Collective Effects	134
<b>6.5</b>	<b>Conclusion</b>	<b>138</b>

---

### 6.1 Introduction

Numerous experimental studies have suggested that the thermal conductivity of nanofluids is unusually high [15, 17]. On the theoretical side predictions of effective medium theories are accurate in some cases [79] but generally fail to account for the large enhancement in conductivity. Despite of the large number of - sometimes conflicting or controversial - suggestions and experimental findings [80] (fig. 1.2), the microscopic mechanisms for such an increase remain unclear.

Knowing the importance of interfaces in nanocomposite materials, an essential feature of nanofluids is the large influence of interfacial thermal resistance, called Kapitza resistance. Its meaning can be understood by defining a characteristic Kapitza length as the product of the Kapitza resistance with the thermal conductivity. This length is simply the thickness of

material equivalent to the interface from a thermal point of view as shown in figure 6.1.

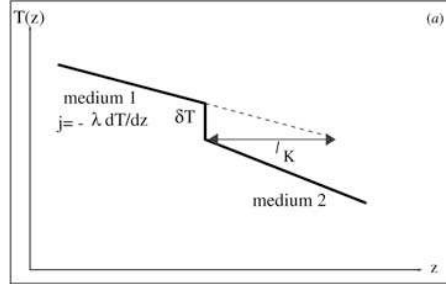


Figure 6.1: Schematic illustration of the Kapitza length of the interface

The Kapitza resistance has been mostly studied in the case of superfluid helium in contact with a solid, or in the case of grain boundaries between pure crystals [81]. In both cases the conductivity is large, so the Kapitza length is large and measurable effects can be expected. Size effects on the thermal conductivity of composites are also an indirect way of assessing the thermal properties of interfaces. These interfacial properties, as we will see later, are crucial for the conductivity of the material.

In this work we use non equilibrium molecular dynamics “experiments” to explore the transfer of heat in a model fluid containing nanoparticles. First we discuss a method for measuring the interfacial resistance. Our approach is closely related to experimental techniques, but we also make use of the flexibility allowed by molecular simulations to explore extreme cases in terms e.g. particle/fluid mass density mismatch and to control the behavior of the particles to assess the influence of collective effects. We concentrate on model systems that are expected to be representative of generic properties. We explore a large range of parameters and make a quantitative comparison with effective medium calculations. We examine in detail the influence of Brownian motion on the thermal transport. By studying the thermal conductivity in a system with two particles and by precisely controlling their positions we are able to observe the influence of collective effects consisting in different particle-particle interactions and displacement with respect to the temperature gradient.

## 6.2 Simulation method

The model fluid used in this study is a simple Lennard-Jones liquid. The nanoparticles (solid phase) suspended in the fluid are represented by roughly spherical inclusions of a bulk fcc solid. All atoms in our system interact

through Lennard-Jones interactions

$$U_{lj}(r) = \begin{cases} 4\varepsilon((\sigma/r)^{12} - c(\sigma/r)^6), & r \leq r_c \\ 0, & r > r_c \end{cases} \quad (6.1)$$

where  $r_c = 2.5\sigma$ . The coefficient  $c$  is equal to 1 for atoms belonging to the same phase, but can be adjusted to modify the wetting properties of the liquid on the solid particle. It has been shown that the variation of this parameter is related to the contact angle between the phases thus providing an efficient way to study systems with different interfacial microscopic wetting behavior [82, 83]. A coefficient of  $c = 1$  defines a wetting interaction while the non wetting case is modeled by  $c = 0.5$ . Within the solid particles, atoms are linked with their neighbors through a FENE (Finite extension non-linear elastic) bonding potential:

$$U_{FENE}(r) = -\frac{k}{2}R_0 \ln(1 - (\frac{r}{R_0})^2) + 4\varepsilon((\sigma/r)^{12} - (\sigma/r)^6) + \varepsilon, \quad r < R_0 \quad (6.2)$$

where  $R_0 = 1.5\sigma$  and  $k = 30.0\varepsilon/\sigma^2$ . This potential, combined with the Lennard-Jones interaction results in a narrow distribution of the distance between linked atoms around  $0.965\sigma$  as discussed in section 3.2. A solid particle in the fluid was prepared as follows: starting from a fcc bulk arrangement of atoms at zero temperature, the atoms within a sphere were linked to their first neighbors by the FENE bond. Then the system was equilibrated in a constant NVE ensemble with energy value corresponding to a temperature  $k_B T = 1\varepsilon$ . A particle contains 555 atoms, surrounded by the atoms of the liquid. The number density in the system is  $\rho = 0.85\sigma^{-3}$ . As the simulated particles are not exactly spherical, but present some FCC facets, special care should be taken when evaluating their radius. Here we estimate this radius ( $R_p$ ) from the radius of gyration of the solid atoms:

$$\langle R_g^2 \rangle = \frac{1}{N} \sum_1^N (r_i - r_{CM})^2 = \frac{3}{5} R_p^2 \quad (6.3)$$

where  $R_g^2$  is the measured radius of gyration of the particle atoms, and the second equality applies to an ideal sphere. Taking  $\sigma = 0.3nm$  this corresponds to a particle radius of order  $R_p \sim 1.5nm$ . The so obtained solid particles behave much like ideal harmonic solids. Non linear effects associated with the non linearity of the bond potential are absent in a wide temperature range. This assumption was verified through equilibrium simulations at different temperatures monitoring the energy per particle. We equilibrate the particle and the surrounding fluid for several values of the temperature and then measure the mean value of the total energy of the nanoparticle for a period of around  $1000\tau$ . The observed relation is linear and indicates a particle heat capacity very close to  $3k_B T N$  as shown on fig. 6.2.

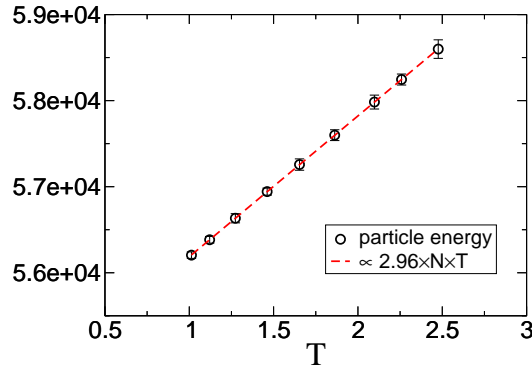


Figure 6.2: Plot of the total energy of the particle for different temperatures. The error bars indicate the standard error from the energy fluctuations. The particle contains 555 atoms.

This value is what one should expect for an harmonic ideal solid, i. e. a capacity of  $3k_B$  per atom in the solid phase. There are no deviations from this behavior in the temperature range (from  $T = 1$  to  $T \approx 3$ ) of interest in our study. In order to cover a large range of physical situations we study systems of both wetting ( $c = 1$ ) and non wetting ( $c = 0.5$ ) particles. For each new value of the constant  $c$  the system is re-equilibrated coupled to a Nose-Hoover thermostat and pressostat to the same pressure. Changing interaction parameters results in a change in pressure due to different behavior of the solid-liquid interface and the equilibration of the different systems is a crucial point. We also explore different density mismatch between the solid and liquid phase ( $m_p/m_l = 1, 50, 100$  where  $m_l$  is the mass of a fluid atom and  $m_p$  is the mass of a particle atom) and different volume fractions of the particle.

### Simulating Heat Flow and Measuring Conductivity

The most simple and direct method of measuring thermal conductivities in a simulation is undoubtedly non equilibrium molecular dynamics. With this set up a temperature gradient is established through the sample and thermal properties are calculated from the measurement of energy fluxes. This method involves locally injecting and evacuating heat in the system. In our study this is achieved by applying two thermostats with different temperatures in the two ends of a fluid slab. The periodicity of the box is maintained in the directions perpendicular to the temperature gradient and the system is non periodic in the direction of the heat flux. If one allows the gradient to change sign in the simulation box a stationary heat flow

can be achieved in a fully periodic box [23]. However with this setup special attention should be paid in the regions of abrupt change in the temperature gradient, and the simulated system is less physically realistic. The systems we study are periodic in the  $x$  and  $y$  directions. Following  $z$  the liquid is confined by the repulsive part of an integrated 9-3 Lennard Jones potential (ideal flat wall). The thermostats are applied to a fluid slice in the vicinity of the walls of width of around 3 atom diameters. The thermostat consists in a rescaling of the velocities of the particles currently present in the slice at a given time interval. The temperature measured locally in slices parallel to the heat flow direction shows that a linear profile is established in the fluid slab. The value of the temperature gradient depends on the temperature of the thermostats and their rescaling time constant (see fig. 6.3).

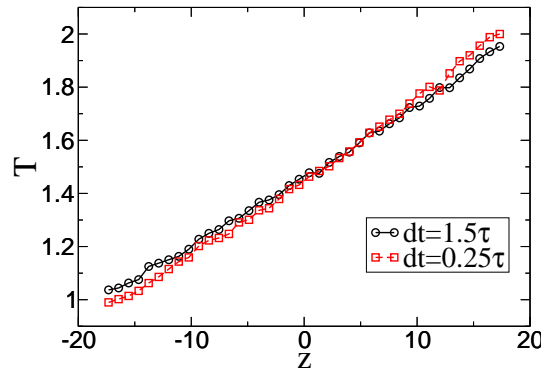


Figure 6.3: Dependence of the temperature profile on the thermostat time constant for a pure liquid. A smaller rescaling interval increases the efficiency of the energy transfer between the thermostat and the liquid inducing a smaller temperature jump.

A smaller rescaling interval increases slightly the energy transfer between the thermostat and the fluid thus maintaining the thermostated layer at an average temperature closer to the temperature of the thermostat. It is thus important to have the same time constant for the thermostat in all the systems in order to compare the values of the energy flow and detect its variations in the different setups. We set this value to  $dt = 1.5\tau$  in the simulations. Using this heat transfer setup, the local thermal conductivity is given by:

$$\lambda(z) = \frac{J(z)}{\nabla T(z)} \quad (6.4)$$

where  $J(z)$  is the heat flow and  $T(z)$  the temperature. This formula is easily generalized to the whole slab by taking the heat flow at the thermostats

and a mean slope of the temperature profile. The problem is that such an estimation of the mean gradient is prone to error. The mean temperature profile for a pure liquid has a well defined slope, even if the fluctuations and the fitting procedure cause error. The situation is worse in the presence of nanoparticles. The temperature profile averaged over liquid and solid atoms has noticeable fluctuations around the particles as the gradient is different in the two phases. That is why measuring an effective value of the conductivity that does not involve fitting and assuming linear temperature profile is preferable. If the thermostat relaxation time is constant for all systems, a well defined values are the two thermostats temperatures. Thus we define the slab conductivity as:

$$\lambda_{eff} = \frac{J}{(T_1 - T_2)/L} \quad (6.5)$$

where  $J$  is the mean stationary heat flux measured by the thermostats,  $T_i$  is the temperature of the thermostat  $i$  and  $L$  is the length of the simulation box in the  $z$  dimension. The conductivity chosen this way is only sensible to variations in the energy flux and is a more precise method for capturing free of artifacts variations in conductivities between systems. Another point that needs attention is the diffusion of the nanoparticle in the liquid undergoing a heat flow. Usually there is a thermal drift of the particle position (thermoporesis). To avoid any effect of thermophoresis or coupling of the thermostat to the particle, the particles are constrained to stay away from the thermostated regions. This is achieved by either tethering weakly their center of mass to a fixed point by harmonic springs of stiffness  $k = 30$  or by applying a flat repulsive potential only to the particle atoms, thus constraining the particles to move in a plane in the middle of the simulation box away from the thermostats. Controlling the particles position also allows to study different configurations and explore the influence of the spatial distribution of the particles on the thermal properties. The temperatures of the two thermostats were  $T_1 = 2$  and  $T_2 = 1$ . In order to compare the conductivity results for the different systems they were first equilibrated to the same pressure at a temperature  $T = 1.5$ , then a non equilibrium run was performed for about 1500-2000  $\tau_{LJ}$  to make sure the pressure stays the same for the systems of different nature and finally a production run of about 15000  $\tau_{LJ}$  during which thermostats energy, particle positions and temperature profiles are monitored.

### 6.3 Modeling pump-probe experiments and determination of the interfacial resistance

As mentioned above, in nanoscale systems it has been observed that interfacial effects are very important [84]. In order to compare quantitatively the

conductivity variations to the predictions of effective medium calculations it is necessary to know the value of the interfacial (Kapitza) thermal resistance. Its value in simulations can be determined both by equilibrium and non equilibrium methods. If we have two infinite media - a solid slab in contact with a fluid,  $R_K$  can be determined via a Green-Kubo relation:

$$\frac{1}{R_K} = \frac{1}{Sk_B T^2} \int_0^\infty \langle q(t)q(0) \rangle dt \quad (6.6)$$

This equation cannot be applied in the case of a spherical particle and it is preferable to use a non equilibrium method for the determination of  $R_K$ . In our study this is achieved by performing a simulation inspired by the experimental setup of pump-probe experiments (known also as transient absorption). The "pump-probe" experiments are used in nanofluids to estimate interfacial resistance. They are an essential ingredient in modeling the thermal properties of highly dispersed systems [85]. The idea is to emit a short laser pulse (pump) that converts some ground state atoms of the metallic particles into their excited states thus increasing selectively the particle temperature. Typically, the temperature of the metal nanoparticles is inferred through changes in optical absorption of the particle-fluid mixture measured by a second, time-delayed beam (probe).

To reproduce this procedure in simulation we prepare a system with a single nanoparticle containing 555 atoms, surrounded by 30000 atoms of liquid. The number density in the system is  $\rho = 0.85\sigma^{-3}$ . For a  $\sigma = 0.3nm$  this corresponds to a system size  $L \sim 10nm$  (the particle radius being about  $R_p \sim 1.5nm$ ). The particle volume fraction in the system is about 1.4%. The transient absorption simulation starts with an equilibrium configuration at temperature  $T = 1$ , by "heating" uniformly the nanoparticle. This heating is achieved by rescaling the velocities of all atoms within the solid particles, so that the kinetic energy per atom is equal to  $3\epsilon$ . We then monitor the kinetic energy per atom of the particle as a function of time, which we take as a measure of the particle temperature. The system evolves at constant energy, but the average temperature of the liquid, which acts essentially as a reservoir, is only very weakly affected by the cooling process. Within a few time steps the kinetic temperature of the particle drops to a value of  $T_p \approx 2$ . This evolution corresponds to the standard one for an isolated, harmonic system. As the particle was equilibrated at  $T_p = 1$ , we have due to kinetic and potential energy equipartition  $\langle E_{pot}(t = 0) \rangle = 1/2$ . As we start our simulation with  $\langle E_k(t = 0) \rangle = 3$ , within a very short time the kinetic energy drops to a value of 1.5, then the potential energy stored in the particle atoms positions yields its contribution of 1/2 to the temperature, equilibrating it to a value of 2. This first step does not involve any heat exchange with the liquid surroundings.

The subsequent decrease of the particle temperature, on the other hand, directly probes such exchanges. A quantitative understanding of this decay

is particularly important, as it remains an essential experimental tool to quantify heat transfer across the particle-liquid interface. In figure 6.4, we compare the molecular dynamics simulation result for the temperature as a function of time, to the result of a continuum calculation involving the interfacial (Kapitza) thermal resistance as an adjustable parameter. The continuum calculation makes use of the standard heat transfer equations

$$C \frac{dT_p}{dt} = -4\pi R_p^2 j(R_p, t) \quad (6.7)$$

$$\frac{\partial T_l}{\partial t} = D_{th} \frac{1}{r^2} \frac{\partial}{\partial r} \left( r^2 \frac{\partial T_l(r, t)}{\partial r} \right) \quad (6.8)$$

where  $T_l(r, t)$  and  $T_p$  are the liquid and particle temperatures, respectively.  $C$  is the thermal capacity of the particle,  $R_p$  its radius,  $D_{th}$  is the thermal diffusion coefficient of the liquid. The above equations are solved with the following boundary conditions:

$$j(R_p, t) = \frac{1}{R_k} (T_l(R_p^+, t) - T_p(t)) \quad (6.9)$$

$$j(R_\infty, t) = 0 \quad (6.10)$$

where  $R_\infty$  is chosen so that  $\frac{4}{3}\pi R_\infty^3$  is equal to the volume of the simulation box from the previous section. The initial condition is

$$T_p(0) = 2 \quad (6.11)$$

$$T_l(r, 0) = 1 \quad (6.12)$$

The temperature was assumed to be uniform inside the nanoparticle. This assumption is based on the simulation results, where the observed temperature profile inside the particle was found independent of position within statistical accuracy. We used data found in the literature [83, 86] for the values of the fluid thermal diffusivity and conductivity. The particle radius is estimated via equation 6.3. The heat capacity of the particle is taken to be  $3k_B T N$ , as obtained from equilibrium simulations (fig. 6.2).

The value of the interface thermal resistance (Kapitza resistance) appearing in equation 6.10 was adjusted to fit the simulation data. The value that fits the simulation results for the wetting system  $m = 1$  and  $c = 1$  was found to be  $R_K \approx 0.8$ . This number is in agreement with the thermal resistance for a wetting flat wall calculated in [83] for a similar system with a different potential in the solid phase, and a completely different simulation method.

The same cooling simulation was performed using a non wetting particle ( $c = 0.5$ ). A substantial slowing down of the cooling rate was also observed, which can be attributed to an increased Kapitza resistance. The resulting value of  $R_K$  is 3.2 (Lennard-Jones units), again in agreement with previous determinations for flat surfaces [83]. In real units, a value  $R_K = 1$  corresponds typically to an interfacial *conductance*  $G = 1/R_K$ , on the order of

$100\text{MW}/\text{Km}^2$ . The conversion to physical units is made by taking a Lennard-Jones time unit  $\tau_{LJ} = 10^{-12}\text{s}$ , and a length unit  $\sigma = 0.3\text{nm}$ . The unit for  $G$  is *energy/temperature/(length)<sup>2</sup>/time*. As the energy/temperature ratio is given by the Boltzmann constant  $k_B$ , we end up with a unit for  $G$  equal to  $k_B/\sigma^2/\tau_{LJ} \simeq 10^8\text{W}/\text{m}^2/\text{s}$ . In view of the results above, we can conclude that the method is a sensitive probe of interfacial resistance, as usually assumed in experiments.

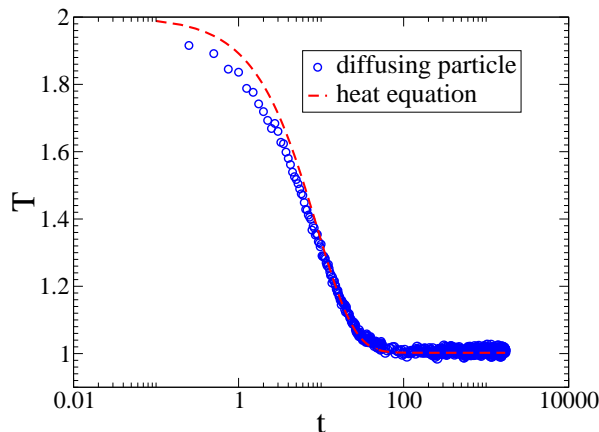


Figure 6.4: Comparison between the temperature evolution from simulations and the solution of the continuum heat equation. The value of the Kapitza resistance taken for the calculation is  $R_K = 0.8$ .

In the second part of this section, we explore the influence of thermal Brownian motion of the particle on the cooling process. First, let us recall that the naive idea, that diffusion could speed up cooling by displacing the particles towards cooler fluid regions is easily excluded. Quantitatively, diffusion of the particle and heat diffusion take place on very different time scales. The diffusion coefficient of the particle was measured, in our case, to be three orders of magnitude smaller than the heat diffusion coefficient in the fluid. We also suppressed diffusion by tethering the particle to its initial position with a harmonic spring of stiffness  $k = 30\epsilon/\sigma^2$ . As expected, no effect is observable on the cooling rate. This measurement cannot probe for another possible effect - the influence of fluid flow on the cooling. As discussed in [87] the heat transfer from a sphere in a low Reynolds number velocity field is enhanced by the latter. Because of the diffusion velocity of the Brownian particle  $v = \left(\frac{3k_B T}{m}\right)^{1/2}$ , it can be viewed, at any given moment, as a particle in a velocity field [19]. To probe the influence of this phenomenon, we tether every single atom in the particle to its initial position with a harmonic spring ( $k = 30$ ) and compare the measured temperature evolution with the previous results. The cooling rate is still not influenced by this manipulation even if

the center of mass is now “frozen” (fig. 6.5).

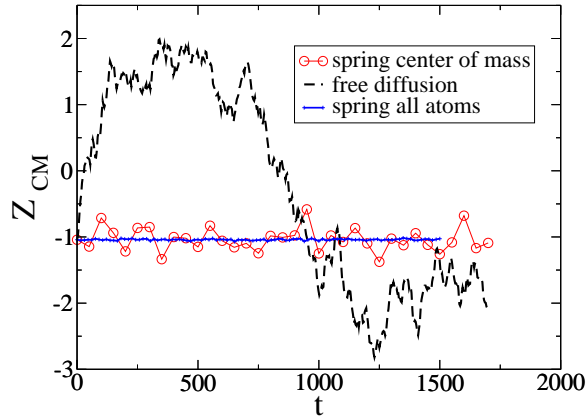


Figure 6.5: Evolution of the  $Z$  coordinate of the particle center of mass for the different systems: free particle, particle confined by a spring attached to its center of mass and particle where all atoms are tethered to their initial position. The spring constant for all springs is  $k = 30$ .

A final check on the influence of such velocity effects was attempted by modifying the mass of the atoms that constitute the nanoparticle. This artificial procedure reduces the thermal Brownian velocity, and when it is carried out we indeed observe a strong slowing down of the cooling process. However, this slowing down is again completely independent of the center of mass motion of the particle, which is controlled by the presence of the tethering springs. On the other hand, the effect of this mass density increase is easily understood in terms of an increase of the interfacial resistance. A higher mass of the particle atoms decreases the speed of sound in the solid and thus leads to a larger acoustic mismatch between the two media, which slows down the cooling. Numerically, we find that for a mass of 100 times the mass of a liquid atom, the Kapitza resistance increases to  $R_K = 7.4$  (fig. 6.7).

In summary, we have shown that the Brownian motion of the particle does not affect the cooling process. As a byproduct, we have shown that the mass density parameter provides a flexible numerical way of tuning the interfacial resistance, which will be used in the following section of this chapter.

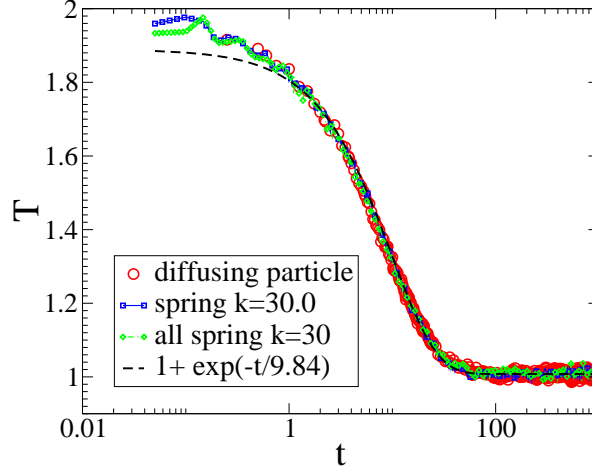


Figure 6.6: The evolution of the particle temperature for the different systems: free particle, particle confined by a spring attached to its center of mass and particle where all atoms are tethered to their initial position. Every curve is the mean value from 20 simulation runs. No effect is observed.

## 6.4 Conductivity of nanofluids

### 6.4.1 The Maxwell Garnett calculation

The standard way of predicting the thermal conductivity of composite materials are the effective medium calculations. If one takes into account the interfacial thermal resistance between the different materials in the composite, the resulting equation for the thermal conductivity is called a Maxwell Garnett equation. This approach has been successful in predicting the thermal properties of solid composites, as well as for some particle suspensions. We present briefly here the derivation of the Maxwell Garnett equation for the effective thermal conductivity in a two phase media (matrix with spherical inclusions) taking into account the interfacial thermal resistance. We consider a macroscopically homogeneous material with thermal conductivity  $\lambda_{eff}$  in a temperature gradient following some axis:  $T_{eff}(r) = -\vec{g} \cdot \vec{r}$ . We concentrate on a spherical inclusion of radius  $r_0$  and conductivity  $\lambda_1$  surrounded by a spherical shell of host material of thickness  $r_1$ , matrix conductivity  $\lambda_2$  and we assume that the inclusion does not change the temperature field for  $r > r_1$ . The two radii define the volume fraction of the inclusion,  $\Phi = r_0^3/r_1^3$  (fig. 6.8). The effective conductivity can be determined by solving the steady state diffusion equation for the temperature:

$$\Delta T(r, \theta) = 0 \quad (6.13)$$

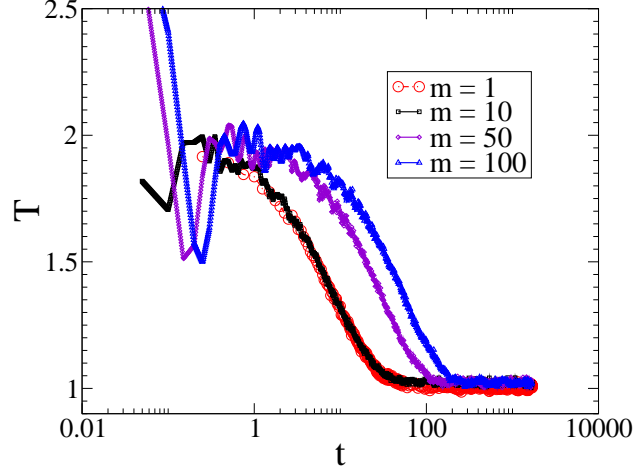


Figure 6.7: The evolution of the particle temperature as a function of the mass of the particle atoms. Every curve is the mean value from 20 simulation runs. The increased mass slows down heat exchange.

where  $\theta$  is the angle between  $\vec{r}$  and the external gradient  $\vec{g}$ . The solutions of equation 6.13 in the three different regions are given by:

$$T_1(r, \theta) = Ar \cos \theta, \quad 0 < r \leq r_0 \quad (6.14)$$

$$T_2(r, \theta) = (Br + E/r^2) \cos \theta, \quad r_0 < r \leq r_1 \quad (6.15)$$

$$T_{eff}(r, \theta) = -gr \cos \theta, \quad r_1 < r \quad (6.16)$$

The unknown constants in the equations above are to be determined from the appropriate boundary conditions. These are obtained by expressing the continuity of the heat flow at the domain boundaries and the value of the temperature field:

$$T_1(r_0, \theta) - T_2(r_0, \theta) = -\lambda_1 \frac{\partial T_1}{\partial r}(r_0) R_K \quad (6.17)$$

$$\lambda_1 \frac{\partial T_1}{\partial r}(r_0) = \lambda_2 \frac{\partial T_2}{\partial r}(r_0) \quad (6.18)$$

$$T_2(r_1, \theta) = T_{eff}(r_1, \theta) \quad (6.19)$$

$$\lambda_2 \frac{\partial T_2}{\partial r}(r_1) = \lambda_{eff} \frac{\partial T_{eff}}{\partial r}(r_1) \quad (6.20)$$

where  $R_K$  is the interfacial thermal resistance responsible for a temperature jump at the matrix-inclusion interface. Substituting the solutions for the temperature fields in equations 6.18-6.20, we end up with the following

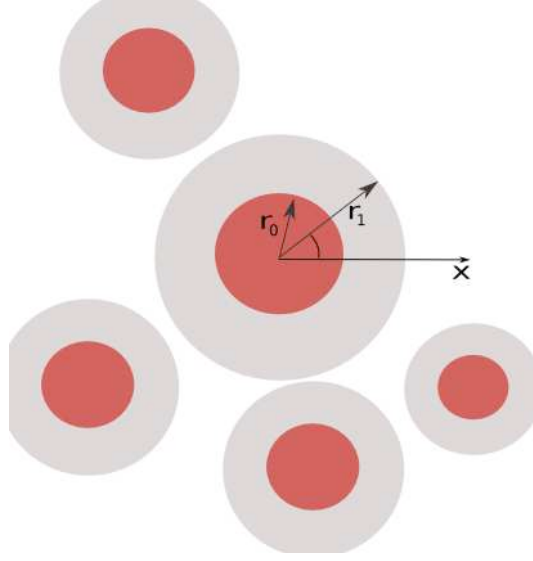


Figure 6.8: Schematic presentation of the matrix with dispersed inclusions

relations:

$$Ar_0^3 - Br_0^3 - E + \lambda_1 R_K Ar_0^2 = 0 \quad (6.21)$$

$$\lambda_1 Ar_0^3 - \lambda_2 Br_0^3 + 2\lambda_2 E = 0 \quad (6.22)$$

$$Br_1^3 + E + gr_1^3 = 0 \quad (6.23)$$

$$\lambda_2 Br_1^3 - 2\lambda_2 E + \lambda_{eff} gr_1^3 = 0 \quad (6.24)$$

Using this set of equations, one can obtain the Maxwell Garnett equation for the effective conductivity with interfacial thermal resistance:

$$\frac{\lambda_{eff}}{\lambda_2} = \frac{\left(\frac{\lambda_1}{\lambda_2}(1 + 2\alpha) + 2\right) + 2\Phi\left(\frac{\lambda_1}{\lambda_2}(1 - \alpha) - 1\right)}{\left(\frac{\lambda_1}{\lambda_2}(1 + 2\alpha) + 2\right) - \Phi\left(\frac{\lambda_1}{\lambda_2}(1 - \alpha) - 1\right)} \quad (6.25)$$

where  $\alpha = R_K \lambda_2 / r_0$ . The parameter  $\alpha$  is crucial for the effective conductivity. It represents the ratio of the thermal interface width to the inclusion radius. The product  $R_K \lambda_2$  called Kapitza length is simply the thickness of material 1 equivalent to the interface from a thermal point of view (see figure 6.1).

Equation 6.25 predicts an increase in the effective conductivity for  $\alpha > 1$  and a decrease for  $\alpha < 1$ , regardless of the value of the conductivity of the inclusions or of their volume fraction. If a composite is made of inclusions whose size is smaller than the thermal interface they create, the resulting effective conductivity will be smaller than the one of the matrix, even if the inclusions are much more conductive than the matrix. The prediction depends very weakly on the ratio  $\lambda_1/\lambda_2$ , less than 1% for  $10 < \lambda_1/\lambda_2 < 100$ .

The minimum value of  $\lambda_{eff}/\lambda_2$ , obtained when  $\alpha \rightarrow \infty$ , is  $\frac{1-\Phi}{1+\Phi/2}$  while the maximum possible enhancement (for  $\lambda_1 \rightarrow \infty$  and  $R_K \rightarrow 0$ ) is  $\frac{1+2\Phi}{1-\Phi}$ .

### 6.4.2 Single particle in a heat flow

In this section we turn to the direct measurement of the thermal conductivity of a nanofluid slab in a thermal gradient. Periodic boundary conditions are maintained in the  $x$  and  $y$  direction and the system is confined by a flat repulsive potential in the  $z$  direction. We study systems with particle volume fraction of 2%, 13% or 12%. The volume fraction is defined as the volume of the particle divided by the volume of the fluid outside the thermostats.

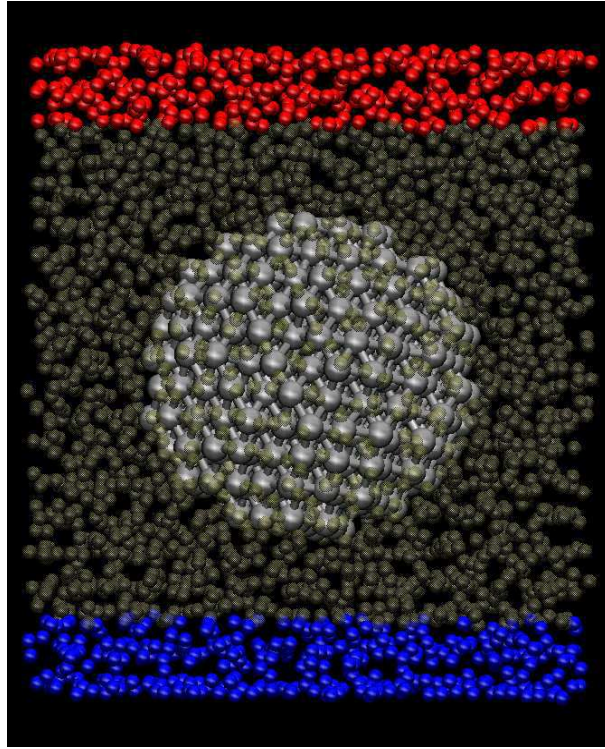


Figure 6.9: Snapshot of the system used to evaluate the thermal conductivity with a particle of 13% volume fraction.

First we checked the influence of Brownian motion on the measured conductivities. The conductivity was measured in several different set-ups, the particle movement was controlled by attaching its center of mass with a spring, by attaching all its atoms to their initial positions and by letting the particle diffuse freely in the  $x - y$  plane in the middle of the simulation box. As expected from the study in the previous section, no effect of the particle diffusion on the fluid conductivity was observed. The effective conductivity measured for the particle diffusing in 2D, the particle attached with a

single spring or the particle where all atoms were attached to their initial positions has the same value within 1% which is below the error bar of the measurement (around 2-3%).

Now we investigate the effect of the presence of a single nanoparticle on the thermal conductivity of the fluid. In this system the particle center of mass is at equal distance from the two thermostats (fig. 6.9). We performed simulations for a small volume fraction ( $\Phi \sim 2\%$ ), where we were not able to detect any change in thermal conductivity compared to the bulk fluid. At a higher volume fraction ( $\Phi \sim 13\%$ ), on the other hand, we observe a clear *decrease* in the heat conductivity associated with the presence of the nanoparticle (fig. 6.10). The Kapitza resistance  $R_K$  for the considered particles ranges from 1 to 7 so that the associated characteristic Kapitza length is in all cases on the order of and larger than the particles diameter. This means that the decrease must be interpreted in terms of interfacial effects as discussed in section 6.4.1. To quantify these effects, we use the Maxwell-Garnett equation 6.25 [88].

The Kapitza resistance can be modified by tuning either the liquid solid interaction coefficient  $c$ , or the mass density of the solid, or a combination thereof. Figure 6.10 illustrates the variation of the measured effective conductivity for several values of the Kapitza resistance, determined independently for various values of these parameters. It is seen that the observed variation (decrease in our case) in the effective conductivity is very well described by the Maxwell-Garnett expression. This expression also allows us to understand why the heat conductivity does not vary in a perceptible manner for small volume fractions ( $\sim 2\%$ ), for which the predicted change would be less than 2%, within our statistical accuracy.

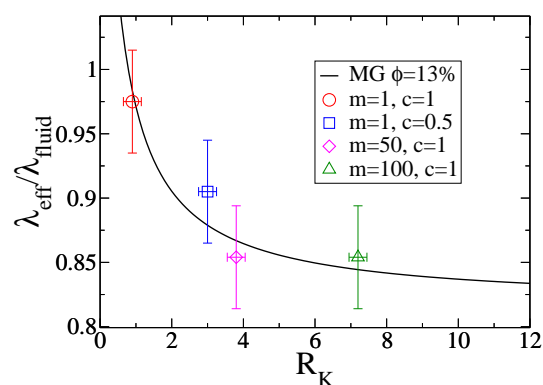


Figure 6.10: Comparison between the ratio of the effective conductivity to the conductivity of the pure liquid of the simulated systems and the values obtained from the Maxwell Garnett equation.

### 6.4.3 Study of Collective Effects

Given the previous discussion it is rather clear that Brownian motion cannot cause an increase in the conductivity and in the case of small nanoscopic particles the interfacial resistance can cause a decrease in the effective conductivity. This means that the large increase reported in some experiments has to come from some kind of collective effects and cannot be explained considering a single particle. In this section we study a system of volume fraction 12% containing two nanoparticles in different configurations probing for the influence of collective effects. In order to model the influence of microscopic particle clustering we tether the particles by soft springs to stay in “contact”, directly interacting with each other (fig. 6.11). We modify the particles center of mass position with respect to the temperature gradient - the particles are either aligned parallel or perpendicular to the gradient. In these two situations the solid phase has an aspect ratio of either  $a = 2$  (parallel) or  $a = 1/2$  (perpendicular). We also varied the Lennard-Jones interaction intensity between the two particles ( $\varepsilon_{pp}$ ) in order to increase the rate of particle-particle energy transfer. The particles-liquid thermal resistance is also modified by choosing different wetting properties or different ratios of the masses of the atoms belonging to the two phases. Finally to reflect a broader range of configurations we also modified the distance between the centers of mass of the particles. In most configurations the particles are directly interacting with each other and in two setups they are separated following the  $z$  direction by a layer of liquid on the order of a particle diameter. An overview of the studied systems can be seen in table 6.1.

System name	Aspect ratio $a$	$\varepsilon_{pp}$	$m_p/m_l$	$c$	$R_K$	Particle-particle $\Delta r$
$a2\varepsilon1m1c1$	2.0	1.0	1	1	0.8	$2R_p$
$a2\varepsilon10m1c1$	2.0	10.0	1	1	0.8	$2R_p$
$a2\varepsilon1m50c1$	2.0	1.0	50	1	4.0	$2R_p$
$a2\varepsilon10m50c1$	2.0	10.0	50	1	4.0	$2R_p$
$a2\varepsilon10m1c0.5$	2.0	1.0	1	0.5	3.2	$2R_p$
$a0.5\varepsilon1m1c1$	0.5	1.0	1	1	0.8	$2R_p$
$a0.5\varepsilon10m1c1$	0.5	10.0	1	1	0.8	$2R_p$
$a0.5\varepsilon1m50c1$	0.5	1.0	50	1	4.0	$2R_p$
$a0.5\varepsilon10m50c1$	0.5	10.0	50	1	4.0	$2R_p$
$\varepsilon1m1c1$	×	1.0	1	1	0.8	$4R_p$
$\varepsilon1m50c1$	×	1.0	50	1	4.0	$4R_p$

Table 6.1: List of the studied systems containing two particles. The last column indicates the distance between the centers of mass of the two particles.

First we study the systems of aspect ratio 2 and strong particle-particle interaction as a function of the interfacial resistance (fig. 6.11). Given that the intense pair potential between the particles makes them move as a single

rigid body and the heat transfer between them is considerably enhanced, it makes sense to compare the obtained conductivities to what effective medium calculation would predict for an ellipsoid of the same aspect ratio. A calcula-

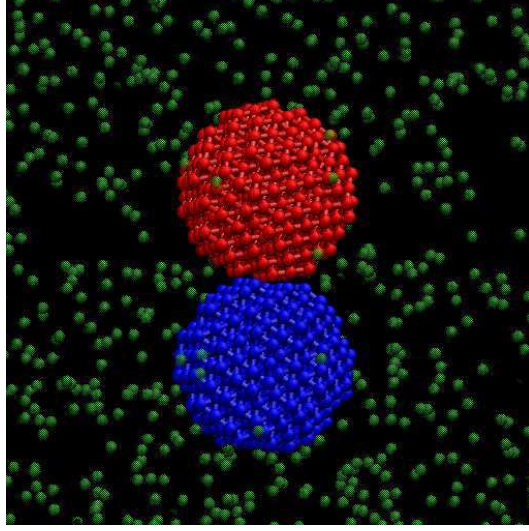


Figure 6.11: Snapshot of the system containing two particles aligned with the temperature gradient having strong particle-particle interaction.

tion including interfacial thermal resistance for equisized ellipsoidal particles aligned with the thermal gradient relevant for this case can be derived from a general expression in ref. [88]. The ratio of the effective conductivity to the conductivity of the pure liquid is given by:

$$\frac{\lambda_{eff}}{\lambda_l} = \frac{1 + \Phi\beta(1 - L_{zz})}{1 - \Phi\beta L_{zz}} \quad (6.26)$$

where  $\Phi$  is the volume fraction,  $L_{zz}$  is given by

$$L_{zz} = 1 - 2 \left( \frac{a^2}{2(a^2 - 1)} - \frac{a^2}{2(a^2 - 1)^{3/2}} \cosh^{-1} a \right) \quad (6.27)$$

with aspect ratio  $a > 1$ . The parameter  $\beta$  is given by

$$\beta = \frac{\lambda^c - \lambda_l}{\lambda_l + L_{zz}(\lambda^c - \lambda_l)} \quad (6.28)$$

where

$$\lambda^c = \frac{\lambda_p}{1 + \frac{\lambda_p}{\lambda_l} (2 + 1/a) \frac{R_K \lambda_l}{R_p} L_{zz}} \quad (6.29)$$

In the above  $\lambda_p$  and  $\lambda_l$  are the conductivities of the particles and the liquid,  $R_p$  is the particles radius and  $R_K$  - the Kapitza resistance of the particle-liquid interface. The relations hold for an aspect ratio  $a > 1$ .

As can be seen on fig. 6.12 the measured conductivities are in reasonable agreement with the calculation. For the smallest interfacial resistance there is an enhancement of the composite system conductivity not larger than 10% and for larger  $R_K$  the small radius of the particles makes that there is a decrease in the conductivity due to interfacial effects.

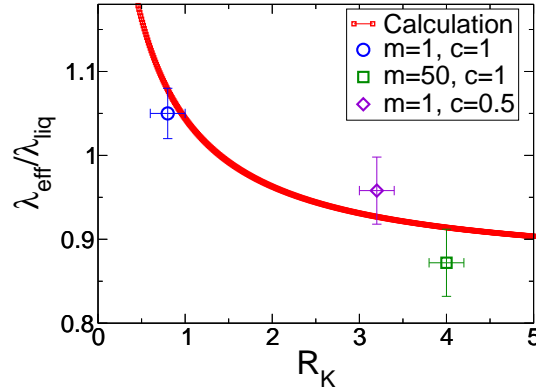


Figure 6.12: Comparison of the measured variation in conductivity in the  $\varepsilon = 10$ ,  $a = 2$  systems to the prediction of the effective medium calculation with aspect ratio 2 and volume fraction 0.12 (equation 6.26).

Next we study the thermal behavior of the systems with particles aligned with the thermal gradient and neutral particle-particle interaction  $\varepsilon_{pp} = 1$  ( $a2\varepsilon1m50c1$ ,  $a2\varepsilon1m1c1$  in table 6.1). The tenfold stronger interaction increases the measured conductivity by about 4% (3% for  $m = 50$  and 5% for  $m = 1$ ). Even if the contact area between the two particles is small, the increased interaction intensity influences the temperature of the particles as can be seen on fig. 6.13. As the strongly attractive interaction decreases the particle-particle thermal resistance the particles temperatures are closer for  $\varepsilon_{pp} = 10$ . As the particles are much more conductive than the liquid phase their temperature varies very little within their dimension, it is essentially constant. We observed that the temperature difference between the particles decreases by a factor of two when the interaction intensity is increased by a factor of ten:  $\Delta T = 0.22$  for  $\varepsilon_{pp} = 1$  and  $\Delta T = 0.12$  for  $\varepsilon_{pp} = 10$  in the systems of  $m = 1$ . In the  $m = 50$  case  $\Delta T(\varepsilon_{pp} = 1) = 0.44$  and  $\Delta T(\varepsilon_{pp} = 10) = 0.2$ . Because of the layers of fluid (of thickness around  $5\sigma$ ) remaining in both cases between the particles and the thermostats the global conductivity of the slab is still dominated by interfacial effects and its increase is small.

When the particle-particle distance increases so that the particles do not interact directly with each other the conductivity of the sample stays nearly

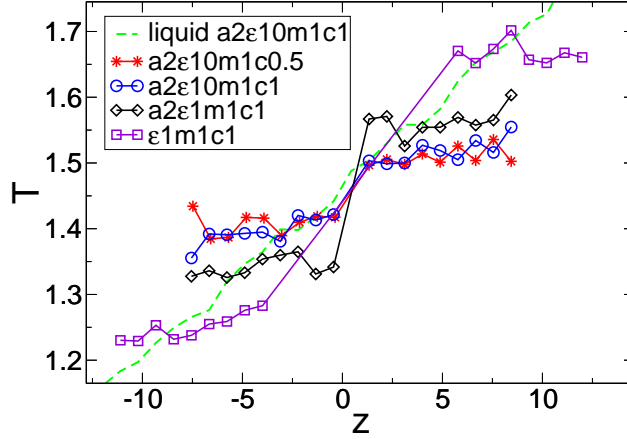


Figure 6.13: Temperature profiles in the particles in the  $m = 1$  systems in stationary heat flow. The temperature profile of the liquid for one of the systems is also shown, for the other systems the liquid temperature profile is very similar. Stronger interaction decreases the temperature difference between the particles approximately twice compared to particles separated by the same distance with neutral interaction.

identical (difference  $\sim 1\%$  in favor for the system where the particles are closer) to the case where they are in contact and with neutral interaction. Knowing that the contact area is very small when the particles are close and also given that the interaction is not strong, being equal to the interaction with the liquid atoms  $\varepsilon_{pp} = \varepsilon = 1$ , the inter particle distance in this case does not play an important role in the value of the conductivity. As can be seen on fig. 6.13 whenever  $\varepsilon_{pp} = \varepsilon = 1$  the average temperature of the particle is close to the average temperature of the liquid at the  $z$  coordinate of its center of mass, the particle thermalizes with the surrounding fluid. In contrast, when  $\varepsilon_{pp} = 10$  the inter particle heat flux becomes important and the two particles behave more like a single body.

We now turn to the conductivity of the systems where the particles are in the plane situated in the middle of the box and orthogonal to the temperature gradient. The heat fluxes measured for the systems of aspect ratio 1/2 with strong and neutral particle-particle interaction were identical within our statistical accuracy (difference less than one percent). The conductivities in this case are slightly lower, with about 4.5% (2% for  $m = 1$  and 7% for  $m = 50$ ) than the case where the particles are aligned with the temperature gradient and has neutral interactions ( $\varepsilon_{pp} = 1$ ). The difference is further increased to  $\sim 8\%$  (7% for  $m = 1$  and 10% for  $m = 50$ ) when the  $a = 0.5$  systems are compared with the  $a = 2$  and  $\varepsilon_{pp} = 10$  systems.

In summary, we showed that the mutual positions of the particles in suspension in the fluid has an influence on the thermal conductivity of the system. If the particles interact so that clustering occurs in the suspension, the global conductivity of the nanofluid can increase to values higher than those for a pure fluid, even if a well dispersed suspension at the same volume fraction has a conductivity lower than the pure system. The alignment with the temperature gradient enhances the conductivity and its effect on a microscopic level can be predicted by effective medium calculation taking into account the aspect ratio of the particle cluster. According to the effective medium prediction the ratio of the slab conductivity to the conductivity of the pure liquid grows linearly with the number of aligned particles (or the aspect ratio) (see fig. 6.14) when this number is smaller than the ratio of the conductivities of the two phases ( $\lambda_p/\lambda_l$ ).

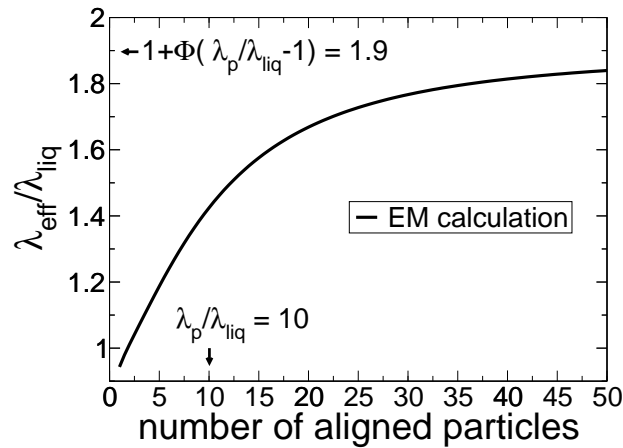


Figure 6.14: Prediction of the effective medium calculation (equation 6.26) for the ratio of the system conductivity to the conductivity of the liquid for an interfacial resistance  $R_K = 1$ .

The enhancement tends to  $(1 - \Phi) + \Phi\lambda_p/\lambda_l$  when the aspect ratio tends to infinity. Thus, following this calculation that seems to give reasonable results at least on the scale of two particles and given that the ratio  $\lambda_p/\lambda_l$  is usually high in real nanofluids, a big enhancement can be expected through particle alignment.

## 6.5 Conclusion

We have explored some important aspects of the thermal properties of nanofluids, at the level of model system, individual solid particles and collective

effects involving two particles on a microscopic scale.

The molecular modelling of transient heating experiments confirms that they are a sensitive tool for the determination of thermal boundary resistances. The effect of Brownian motion on the cooling process, on the other hand, was found to be negligible.

By varying interaction parameters or mass density, we are able to vary the interfacial resistance between the particle and the fluid in a large range. This allowed us to estimate, over a large range of parameters, the effective heat conductivity of a model nanofluid in which the particles would be perfectly dispersed. The results for this setup can be simply explained in terms of the classical Maxwell-Garnett model, provided the interfacial resistance is taken into account. The essential parameter that influences the effective conductivity turns out to be the ratio between the Kapitza length and the particle radius, and for very small particles a decrease in conductivity compared to bulk fluids is found.

We also examined the effect of particle clustering and alignment with respect to the temperature gradient. We found that alignment improves the conductivity of the nanofluid in accordance with calculation with effective medium approach. Increased inter particle interaction further enhances conductivity. The increase in the case of alignment and neutral interaction persists even when the particles do not interact directly with each other but through a fluid layer.

Given our results it is possible, even if difficult, to provide some clues explaining the diversity of experimental findings about nanofluids conductivity. As collective effects have been shown to be the only possibility of providing tremendous increase in conductivity, special care should be taken in experiment for the determination of the exact level of dispersity of the nanofluid. It is clear that in real nanofluids there are very few isolated particles that contribute to the conductivity as described in section 6.4.2. Nanoparticle clusters and aggregates are generally persistent and difficult to brake for nearly any way of preparation. It seems plausible that small differences in the way of preparation of the samples thus result in noticeable differences in the value of the conductivity.

In order to draw more precise conclusions concerning the conductivity dependence on the complex physics of collective effects undoubtedly larger systems should be examined. The present study provides guidelines and outlines general tendencies that are to be expected in a larger and more complex system.



## Chapter 7

# Conclusion and Perspectives

### Contents

---

<b>7.1 Summary of the main results</b> . . . . .	<b>141</b>
<b>7.2 Perspectives</b> . . . . .	<b>143</b>

---

### 7.1 Summary of the main results

We began our study with an investigation of the viscoelastic behavior of a pure model polymer melt. The Green Kubo method for measuring viscosity revealed that a precise determination needs a large computational effort, so we proposed an alternative method inspired by the Rouse model. Based on a measurement of the Rouse modes of the chains at equilibrium, this method provides a satisfactory description of the viscosity and of the elastic moduli of the melt and, being based on a single chain quantity, is inherently local and therefore can be applied to the study of local dynamics in heterogeneous systems.

We showed that inter chain interactions in the melt add a non negligible background part to the storage modulus and dictate the loss modulus behavior at high frequencies. These interactions should be taken into account for a precise description of the mechanical properties of a polymer melt made of relatively short chains and are important for longer chains in several far from equilibrium situations.

We demonstrated by non equilibrium MD simulations of bulk polymer melts that the elastic energy storage takes place in chain conformations relaxing on times longer than the period of the external solicitation. Energy dissipation is, on the contrary, dictated by short time scales “non polymer” stress relaxation and subchain relaxation on times shorter than the solicitation period. Chain vibration modes are “frozen” one by one as the frequency grows higher than the inverse mode relaxation time.

The non linear regime is dictated by the shear rate of the solicitation and takes place at  $\gamma_0\omega > 1/\tau_R$  for  $\omega < 1/\tau_R$ . At higher frequencies, the onset of nonlinear effects is related to the strain amplitude rather than rate, as full chain relaxation does not take place on the time scale of one oscillation. Our study allows a comprehensive description of the melt mechanical behavior in the form of a schematic frequency - shear rate diagram (fig. 3.16).

Next, we examined the static and dynamic properties of polymers in a melt in the presence of a flat surface. Static conformations near the surface were compared to predictions from a random walk model and found to be in good agreement for the number of trains per chain. The length of the trains is larger than in the random walk model, reflecting a tendency of chains to lie flat on the surface.

The population of chains is shown to contain a portion of weakly adsorbed chains with rapid desorption dynamics and strongly adsorbed chains with slower desorption dynamics. The desorption time is seen to scale slightly slower than  $N^2$ , for chains up to  $N = 100$  showing dynamics more complex than the predictions of a simple diffusion based model.

We further extended our study to cover the melt properties in a wider zone covering the whole interface with different microscopic chemical nature of the wall. We find that the modifications in the dynamics due to the surface treatment depends on the level of entanglement of the melt. In the case of unentangled melts, the dynamics are, both for bare and grafted wall, accelerated compared to the bulk. In the case of weakly entangled melts, the presence of the flat surface induces a decrease ( $\sim 20 - 40\%$ ) in the entanglement density in a range of about  $R_G$  from the surface. In contrast, the presence of grafted chains prevents this depletion of the entanglements and further increases the entanglement density in the interfacial layer. This leads to slower dynamics in the interfacial layer and a local increase of the relaxation times of the entangled Rouse modes near the surface. The behavior of the relaxation times can be predicted by measuring the local entanglement length, following the expression given by reptation theory.

Our study showed that reinforcement via the entanglement network can be obtained in presence of grafted chains and chain confinement at the interface, i.e. for fillers larger than the chain typical size.

In order to cover a broader range of physical situations, we studied a model polymer nanocomposite with spherical fillers, smaller than the spatial extension of the polymer chains. The chains are not confined in this case and their dimensions tend to increase compared to those in a pure melt. We report that the presence of attractive nanofillers with subchain dimensions and volume fraction allowing bridging leads to an effective increase of the total entanglement density in the system. Fillers tend to act as reticulations, creating new effective entanglements between chains. The measured reduction of the entanglement length can be partly predicted by packing arguments and with a model taking into account the polymer bridges be-

tween fillers in the melt. This effect plays a role in the mechanical properties of nanocomposites either filled with small size attractive fillers or for high molecular weight melts where the chains become larger than the fillers.

In the last part of this study, we have explored some important aspects of the thermal properties of “nanofluids”, at the level of model system, individual solid particles and collective effects involving two particles on a microscopic scale.

The molecular modeling of transient heating experiments confirms that they are a sensitive tool for the determination of thermal boundary resistances. The effect of Brownian motion on the cooling process, on the other hand, was found to be negligible. By varying interaction parameters or mass density, we are able to vary the interfacial resistance between the particle and the fluid in a large range. This allowed us to estimate, over a large range of parameters, the effective heat conductivity of a model nanofluid in which the particles would be perfectly dispersed. The results for this setup can be simply explained in terms of the classical Maxwell-Garnett model, provided the interfacial resistance is taken into account. The essential parameter that influences the effective conductivity turns out to be the ratio between the Kapitza length and the particle radius, and for very small particles a decrease in conductivity compared to bulk fluids is found, even if particles are many times more conducting than the fluid.

We also examined the effect of particle clustering and alignment with respect to the temperature gradient. We found that alignment improves the conductivity of the nanofluid in accordance with a calculation with effective medium approach. Increased inter particle interaction further enhances conductivity. The increase in the case of alignment and neutral interaction persists even when the particles do not interact directly with each other but through a fluid layer.

Given our results it is possible, even if difficult, to provide some clues explaining the diversity of experimental findings about nanofluids conductivity. As collective effects have been shown to be the only possibility of providing tremendous increase in conductivity, special care should be taken in experiment for the determination of the exact level of dispersity of the nanofluid. It seems plausible that small differences in the way of preparation of the samples thus result in noticeable differences in the value of the conductivity.

## 7.2 Perspectives

The results presented in this work provide a background for a number of future studies. We have provided the tools and understanding needed to undertake more precise investigations of the linear and non linear mechanical properties in composite polymer based materials. An interesting question

arising from our results is what would be the mechanical response of the polymer interface to external solicitation. The equilibrium entanglement density at a polymer-wall interface was found to vary as a function of the wall surface chemistry and the presence of grafted chains was shown to provide additional entanglements. This finding could be more precisely related to practical applications. In order to establish such relation, the dependence of the entanglement density on shear, including the exact dependence on the amplitude and the frequency of the solicitation and the mechanical history of the sample, need to be examined. For instance, the onset of non linear effects can be governed either by the global chain relaxation time as we showed for pure melts, or by the entanglement time. The relevant length scale in this phenomenon is expected to be related to the tube diameter, itself dependent in equilibrium on the surface structure as discussed (interaction, grafting, chain length). This analysis can be achieved by applying the primitive paths quench systematically after a precise number of shear cycles with given shear rate. Another question concerns the dynamics of entanglements - do they have a longer lifetime near the interface compared to the bulk? This problem is harder to study by conventional molecular dynamics using the bead spring model, due to the long computational time needed to study disentanglement.

Non equilibrium simulations could also provide interesting results for the nanocomposite systems. The response of the filled melt to solicitation, compared to the behavior observed in the pure melts is of great practical interest. Again the case of sub chain size fillers can be compared to the case of a grafted wall, relevant for larger filler particles. The response to high amplitude and frequency shear can in principle be examined in the scope of the coarse grained models we considered. Understanding of the molecular mechanisms involved can be achieved through non equilibrium molecular dynamics via a Lees-Edwards setup as we used in chapter 3.

The modification of the effective entanglement density in filled melts reported here should also have an impact on the stress-strain curves one measures in these systems [89]. Applying uniaxial deformation and studying the resulting stress-strain relation as well as an eventual cracking in the material is another problem that can be addressed via molecular dynamics on the samples we studied.

Last but certainly not least, the obtained results and modeling at the scale we considered can also be integrated into models of higher level of coarse graining (such as described in [90, 91, 92]) for a study of the viscoelastic behavior on larger time and length scales.

As a part of this work we also studied the thermal conductivity of nanoparticle suspensions. At this stage the subject is somewhat disconnected from the larger part of the thesis concerning polymer melts. A straightforward application of interest using the accumulated results and knowledge in the two fields would be the study of thermal transport in filled polymer melts. Experimental work on the subject suggests phenomena differing from

---

the case of a liquid, involving possibly different mechanisms in this case [79]. The study of such a system involves the introduction of all atom thermal nanofiller in the polymer melt (this being a rather standard procedure [93]) and simulating a thermal flow in the sample.

Our study of nanofluids can itself be extended to draw more precise conclusions concerning the conductivity dependence on the complex physics of collective effects. This can be achieved by studying larger systems involving more nanoparticles and precisely controlling their level of dispersion, again varying the interfacial properties.



# Bibliography

- [1] A. M. Bueche. *J. Poly. Sci.*, 25:139, 1957.
- [2] B. Kuriakose, S. K. De, S. S. Bhagawan, R. Sivaramkrishnan, and S. K. Athithan. *J. Appl. Pol. Sci.*, 32:5509, 1986.
- [3] P. C. LeBaron, A. Wang, and T. J. Pinnavaia. *Appl. Clay Sci.*, 15:11, 1999.
- [4] P. B. Messersmith and E. P. Giannelis. *Chem. Mater.*, 6:1719, 1994.
- [5] S. Iijima. *Nature*, 354:56, 1991.
- [6] L. J. Fetters, D. J. Lohse, and W. W. Graessley. Chain dimensions and entanglement spacings in dense macromolecular systems. *J. Polymer Science B-Polymer Physics*, 37(10):1023–1033, May 1999.
- [7] R. Everaers, S. K. Sukumaran, G. S. Grest, C. Savneborg, A. Sivasubramanian, and K. Kremer. Rheology and microscopic topology of entangled polymeric liquids. *Science*, 303:823–826, 2004.
- [8] H.R. Brown and T.P. Russell. Entanglements at polymer surfaces and interfaces. *Macromolecules*, 29(2):798–800, 1996.
- [9] Lun Si, Michael V. Massa, Kari Dalnoki-Veress, Hugh R. Brown, and Richard A. L. Jones. Chain entanglement in thin freestanding polymer films. *Physical Review Letters*, 94:127801, 2005.
- [10] P. A. O’connell and G. B. Mckenna. Dramatic stiffening of ultrathin polymer films in the rubbery regime. *European Physical Journal E*, 20:143–150, 2006.
- [11] H. Bodiguel and C. Fretigny. Reduced viscosity in thin polymer films. *Phys. Rev. Lett.*, 97:266105, Dec 2006.
- [12] H. Itagaki, Y. Nishimura, E. Sagisaka, and et al. Entanglement of polymer chains in ultrathin films. *Langmuir*, 22:742–748, 2006.

- [13] M. E. Mackay, T. T. Dao, A. Tuteja, D. L. Ho, B. Van Horn, H. C. Kim, and C. J. Hawker. Nanoscale effects leading to non-einstein-like decrease in viscosity. *Nature Materials*, 2(11):762–766, Nov 2003.
- [14] Q. Zhang and L. A. Archer. Poly(ethylene oxide)/silica nanocomposites: Structure and rheology. *Langmuir*, 18:10435–10442, Sept 2002.
- [15] J. A. Eastman, S. U. S. Choi, S. Li, W. Yu, and L. J. Thompson. *Appl. Phys. Lett.*, 78:718, 2001.
- [16] D. Hemanth Kumar, Hrishikesh E. Patel, V. R. Rajeev Kumar, T. Sundararajan, T. Pradeep, and Sarit K. Das. Model for heat conduction in nanofluids. *Physical Review Letters*, 93(14):144301, 2004.
- [17] H. E. Patel, S. K. Das, Sundararajan T., A. S. Nair, B. George, and T. Pradeep. *Appl. Phys. Lett.*, 83:2931, 2003.
- [18] S. A. Putnam, D. G. Cahill, P. V. P. V. Braun, Z. Ge, and Shimmin R. G. *J. Appl. Phys.*, 99:0843308.
- [19] R. Prasher, P. Bhattacharya, and P. E. Phelan. *Phys. Rev. Lett.*, 94:025901, 2005.
- [20] B.J. Alder and T.E. Wainwright. *Phys. Rev. A*, 1:18, 1970.
- [21] P. Keblinski and J. Thommin. *Phys. Rev. E*, 73:010502, 2006.
- [22] P. Keblinski, S. R. Phillot, S. U.-S. Choi, and J. A. Eastman. *Int. J. of Heat and Mass Transf.*, 45:855, 2002.
- [23] W. Evans, J. Fish, and P. Keblinski. *Appl. Phys. Lett.*, 88:093116, 2006.
- [24] S. J. Plimpton. *J. Comp. Phys.*, 117:1, 1995.
- [25] P. Rouse. *J. Chem. Phys.*, 21:1272, 1953.
- [26] C. Bennemann, J. Baschnagel, W. Paul, and K. Binder. *Comp. and Theor. Polym. Sc.*, 9:217, 1999.
- [27] J. T. Padding and W. J. Briels. Time and length scales of polymer melts studied by coarse-grained molecular dynamics simulations. *J. Chem. Phys.*, 117(2):925–943, 2002.
- [28] P. G. de Gennes. *Scaling Concepts in Polymer Physics*. Cornell University Press, 1979.
- [29] L. J. Fetters, D. J. Lohse, D. Richter, T. A. Witten, and A. Zirkel. Connection between polymer molecular weight, density, chain dimensions, and melt viscoelastic properties. *Macromolecules*, 27(17):4639, 1994.

- [30] Y. H. LIN. Number of entanglement strands per cubed tube diameter, a fundamental aspect of topological universality in polymer viscoelasticity. *Macromolecules*, 20(12):3080–3083, Dec 1987.
- [31] M. Doi and S. F. Edwards. *The Theory of Polymer Dynamics*. Oxford University Press, 1986.
- [32] A. R. Payne. *J. Appl. Pol. Sci.*, 6:57, 1962.
- [33] A. J. Zhu and S. S. Sternstein. Nonlinear viscoelasticity of nanofilled polymers: interfaces, chain statistics and properties recovery kinetics. *Composites Science and Technology*, 63(8):1113–1126, Jun 2003.
- [34] G. Heinrich and M. Kluppel. *Adv. in Polymer Sci.*, 160:1, 2002.
- [35] J. Berriot, H. Montes, F. Lequeux, D. Long, and P. Sotta. *Europhys. Lett.*, 64:50, 2003.
- [36] S. S. Sternstein and A.-J. Zhu. *Macromolecules*, 35:7262, 2002.
- [37] S. S. Sternstein, G. Ramorino, B. Jiang, and A. J. Zhu. Reinforcement and nonlinear viscoelasticity of polymer melts containing mixtures of nanofillers. *Rubber Chemistry and Technology*, 78(2):258–270, May-Jun 2005.
- [38] J. D. Ferry. *Viscoelastic Properties of Polymers*. Wiley, New York, 3rd edition edition, 1980.
- [39] R. G. Larson. *Constitutive Equations for Polymer Melts and Solutions*. Butterworth Publ., AT&T Bell Labs, 1988.
- [40] M. Kröger. *Phys. Rep.*, 390:453, 2004.
- [41] M. Kröger and S. Hess. *Phys. Rev. Lett*, 85:1128, 2000.
- [42] J. G. H. Cifre, S. Hess, and M. Kroger. *Macromol. Th. Simu.*, 13:748, 2004.
- [43] K. Kremer and G. S. Grest. *J. Chem. Phys.*, 92:5057, 1990.
- [44] D. J. Evans and G. P. Morris. *Statistical Mechanics of Nonequilibrium Liquids*. Academic, New York, 1990.
- [45] F. Varnik and K. Binder. Shear viscosity of a supercooled polymer melt via nonequilibrium molecular dynamics simulations. *J. Chem. Phys.*, 117(13):6336 – 6349, 2002.
- [46] M. P. Allen and D. J. Tildesley. *Computer Simulation of Liquids*. Oxford University Press, 1987.

- [47] H. Flyvbjerg and H. G. Petersen. Error estimates on averages of correlated data. *J. Chem. Phys.*, 91(1):461, July 1989.
- [48] D. Frenkel and B. Smith. *Understanding Molecular Simulation*. Academic Press, 1996.
- [49] R. Zwanzig and N. K. Ailawadi. Statistical error due to finite time averaging. *Phys. Rev.*, 182(1):280, 1969.
- [50] S. Sen, S. K. Kumar, and P. Keblinski. *Macromolecules*, 38:650, 2005.
- [51] Z. Xu, R. Khare, J. J. de Pablo, and S. Kim. *J. Chem. Phys.*, 106:8285, 1997.
- [52] Suchira Sen, Sanat K. Kumar, and Pawel Keblinski. Analysis of uncertainties in polymer viscoelastic properties obtained from equilibrium computer simulations. *The Journal of Chemical Physics*, 124(14):144909, 2006.
- [53] M. Mondello and G. S. Grest. *J. Chem. Phys.*, 106:9327, 1997.
- [54] V. A. Harmandaris, V. G. Mavrantzas, and D. N. Theodorou. *Macromolecules*, 31:7934, 1998.
- [55] M. Kroger, C. Luap, and R. Muller. *Macromolecules*, 30:526, 1997.
- [56] P. J. Flory. *Statistical Mechanics of Chain Molecules*. 1969.
- [57] S. K. Nath, A. L. Frischknecht, J. G. Curro, and J. D. McCoy. *Macromolecules*, 38:8562, 2005.
- [58] J. Baschnagel and F. Varnik. Computer simulations of supercooled polymer melts in the bulk and in-confined geometry. *J. Phys.: Condens. Matter*, 17(32):851, Aug 2005.
- [59] N. C. Karayiannis, V. G. Mavrantzas, and D. N. Theodorou. A novel monte carlo scheme for the rapid equilibration of atomistic model polymer systems of precisely defined molecular architecture. *Phys. Rev. Lett.*, 88(10):105503, Mar 2002.
- [60] R. Auhl, R. Everaers, G. S. Grest, K. Kremer, and S. J. Plimpton. Equilibration of long chain polymer melts in computer simulations. *J. Chem. Phys.*, 119(24):12718–12728, Dec 2003.
- [61] J.-S. Wang and Kurt Binder. *J. Phys. France*, 1:1583, 1991.
- [62] S. K. Kumar, M. Vacatello, and D. Y. Yoon. *Macromolecules*, 23:2189, 1990.

- [63] W. Feller. *An Introduction to Probability Theory and Its Applications*, volume 1. Wiley Text Books, 2nd edition, 1971.
- [64] I. A. Bitsanis and G. Brinke. *J. Chem. Phys.*, 99:3100, 1993.
- [65] A. Silberberg. *J. Colloid and Interface Sci*, 90:86, 1981.
- [66] J. Oberdisse. *Soft Matter*, 2:29, 2006.
- [67] F. Dalmas, L. Chazeau, C. Gauthier, J. Y. Cavaille, and R. Dendievel. *Polymer*, 47:2802–2812, 2006.
- [68] H. R. Brown and T. P. Russell. *Macromolecules*, 29:798, 1996.
- [69] R. Oslanec and H. R. Brown. *Macromolecules*, 36:5839, 2003.
- [70] S. K. Sukumaran, G. S. Grest, Kurt Kremer, and Ralf Everaers. *J. Poly. Sci*, 43:917, 2005.
- [71] M. Vladkov and J.-L. Barrat. Linear and nonlinear viscoelasticity of a model unentangled polymer melt: Molecular dynamics and rouse modes analysis. *Macromol. Th. Simu.*, 15:252–262, 2006.
- [72] K. A. Smith, M. Vladkov, and J. L. Barrat. Polymer melt near a solid surface: A molecular dynamics study of chain conformations and desorption dynamics. *Macromolecules*, 38(2):571–580, Jan 2005.
- [73] G. Huber and T. A. Vilgis. *Eur. Phys. J. B*, 3:217, 1998.
- [74] H. Meyer, T. Kreer, A. Cavallo, J. P. Wittmer, and J. Baschnagel. *to be published in J. Phys. IV France*, 2006.
- [75] M. Vacatello. Molecular arrangements in polymer-based nanocomposites. *Macromol. Th. Simu.*, 11(7):757–765, Oct 2002.
- [76] M. Vacatello. Predicting the molecular arrangements in polymer-based nanocomposites. *Macromol. Th. Simu.*, 12(1):86–91, Feb 2003.
- [77] R. S. Hoy and M. O. Robbins. Effect of equilibration on primitive path analyses of entangled polymers. *Phys. Rev. E*, 72:061802, 2005.
- [78] A. Tuteja, M. E. Mackay, C. J. Hawker, and B. V. Horn. Effect of ideal, organic nanoparticles on the flow properties of linear polymers: Non-einstein-like behavior. *Macromolecules*, 38:8000–8011, July 2005.
- [79] S. A. Putnam, D. A. Cahill, B. J. Ash, and L. S. Schadler. *J. Appl. Phys.*, 94:6785, 2003.
- [80] P. Keblinski, J. A. Eastman, and D. A. Cahill. *Materials Today*, 8:36, 2005.

- 
- [81] L. Puech, G. Bonfait, and B. Castaing. *J. Low Temp. Phys.*, 62:312, 1986.
- [82] J.-L. Barrat and L. Bocquet. *Faraday Discussions*, 112:121, 1999.
- [83] J.-L. Barrat and F. Chiaruttini. *Molecular Physics*, 101:1605, 2003.
- [84] M. Vladkov and J.-L. Barrat. *Nanoletters*, 6(6):1224–1228, 2006.
- [85] O. M. Wilson, X. Hu, D. G. Cahill, and P. V. Braun. *Phys. Rev. B*, 66:224301, 2002.
- [86] B. J. Palmer. *Phys. Rev. E*, 49:2049, 1994.
- [87] A. Acrivos and T. D. Taylor. *Physics of Fluids*, 5:387, 1962.
- [88] C. W. Nan, R. Birringer, D. R. Clarke, and H. Gleiter. *J. Appl. Phys.*, 81:6692, 1997.
- [89] G. Heinrich and T. A. Vilgis. Contribution of entanglements to the mechanical properties of carbon black-filled polymer networks. *Macromolecules*, 26(5):1109–1119, 1993.
- [90] M. Doi and J. Takimoto. Molecular modelling of entanglement. *Phil. Trans. R. Soc. Lond.*, 361:641–652, 2003.
- [91] D. Long and P. Sotta. *Macromolecules*, 39:6282–6297, 2006.
- [92] G. Raos, M. Moreno, and S. Elli. Computational experiments on filled rubber viscoelasticity: What is the role of particle-particle interactions? *Macromolecules*, 39:6744–6751, 2006.
- [93] F. W. Starr, T. B. Schroder, and S. C. Glotzer. Molecular dynamics simulations of a polymer melt with a nanoscopic particle. *Macromolecules*, 35:4481–4492, 2002.